AN ABSTRACT OF THE THESIS OF

Paul D. Thompson for the degree of Doctor of Philosophy in Chemistry presented on June 6, 1991.
Title: Synthesis and Characteristics of New Solid-State Borates.

Redacted for Privacy

Abstract approved: _____
Douglas A. Keszler

In this work I describe new materials in the SrO-Sc_2O_3-B_2O_3 phase system. The orthoborate $Sr_3Sc(BO_3)_3$ has a distinctive structure and is relevant as a possible solid-state laser host. The mixed orthoborate-pyroborate $Sr_2Sc_2B_4O_{11}$ contains a unique planar pyroborate group with the bridging O atom occupying a special position. This compound is the first example of a material in which both orthoborate and pyroborate groups crystallize together in a solid-state structure. I grew single crystals of a new rhombohedral orthoborate, $Sr_3Sc_2(BO_3)_4$, that is another member of the phase system. This compound exhibits an unusually large unit cell caused by B atom ordering and

symmetry requirements.

I acquired DTA data and examined three two-component phase lines within the system triangle. By analyzing the $Sr_3B_2O_6$-$ScBO_3$ liquidus line I determined that $Sr_3Sc(BO_3)_3$ melts congruently.

My work led to the discovery of a new structural class of orthoborate, $A_6MM'(BO_3)_6$, that is now the largest synthetic structural family of solid-state oxides prepared to date. The family contains many of the +2, +3, and +4 rare earth and transition metal cations. I prepared 43 members of the family, studied solid-solution behavior for two series of compounds in the family, and examined luminescence properties of several of the materials. Many members of the family may have potential use as phosphors or laser materials.

I present a new material containing Li atoms that was discovered during an attempt to grow crystals of another material with a $LiBO_2$ flux. The pyroborate $Sr_2ScLi(B_2O_5)_2$ crystallizes in a new structure type characterized by planes of pyroborate groups; the material has five-coordinate Li atoms. I synthesized a pair of unique trigonal borates, $LiSrM_2(BO_3)_3$ (M = Y and Er).

Synthesis and Characteristics of New Solid-State Borates

by

Paul Douglas Thompson

A THESIS

submitted to

Oregon State University

in partial fulfillment of

the requirements for the

degree of

Doctor of Philosophy

Completed June 6, 1991

Commencement June 1992

APPROVED:

Redacted for Privacy

Professor of Chemistry in charge of major

Redacted for Privacy

Head of Department of Chemistry

Redacted for Privacy

Dean of Graduate School

Date thesis is presented June 6, 1991

Prepared and presented by Paul D. Thompson

ACKNOWLEDGMENTS

I thank Professors Ray Woodriff and Patrik Callis for their patient guidance during my undergraduate work at Montana State University. I thank especially Oliver and Donna Ellison, and Dana Hegna for their encouragement and support. I am grateful to my Mom and Dad, and to my brothers James and Charles.

I thank my major professor, Dr. Douglas Keszler, for his pragmatic suggestions, persistence, and depth of insight in guiding my work. For a long time I have "wanted to be a scientist." One morning this past year, because of Doug's influence in my life, I woke up and knew that I am a scientist.

I thank Dr. Carroll DeKock and Dr. James Krueger for having faith in me and supporting me through the tough times.

I am especially grateful to my fellow students and co-workers, all of whom have contributed to my success: Rob Smith, Hongxing Sun, Yaobo Yin, Kathy Schaffers, Jim Cox, Ted Alekel, Tom Reynolds, Jinfan Huang, John Ebner, and Lan Peng. It has been a fascinating and valuable journey.

I am grateful to Vince Grant and Chuck Meitle. I thank the Spirit who has been with me always and is showing me how to walk in the light.

TABLE OF CONTENTS

LIST OF FIGURES

LIST OF TABLES

LIST OF APPENDIX FIGURES

LIST OF APPENDIX TABLES

Synthesis and Characteristics of New Solid-State Borates

CHAPTER 1

INTRODUCTION

An interaction of matter and energy occurs where solid-state materials absorb and emit light. I am interested in the atomic structure of solids and the way structure determines the characteristics of absorption and emission. My research has been directed toward the search for and study of new solid materials that interact with and produce light.

Everyone is familiar with the fluorescent tubes that produce the every-day lights we live in. If you have ever encountered a broken tube you may have touched the white dust that coats the inside of the lamp. This ordinary-looking powder is called a phosphor and performs the most important role in the lamp. Voltage is applied to the mercury vapor in the tube exciting the metal's electrons into energetic states. This energy is emitted as ultraviolet (UV) radiation that strikes the powder. The UV radiation is absorbed by electrons in rare earth and transition metal cations in the powder and causes them to undergo transitions to excited states. The energized electrons in the metals fall back down to their lowest

energy ground states by emitting visible light which we see.

Phosphors are named after phosphorus because some compounds containing this element glow in the dark when the lights are turned off. A mix of phosphors is coated on the inside of lighting tubes to provide light tailored to specific uses: soft white reading light for the living room, a variety of colors for CRT screens, or green-tinged light over the grocer's produce. Common phosphors in use today include Sb- and Mn-doped calcium halophosphate [$Ca_5(PO_4)_3(F,Cl)$:Sb(III),Mn(II)] that emits in the blue and green regions of the spectrum and Eu-doped yttrium oxide [Y_2O_3:Eu(III)] that emits red light. The blue-emitter strontium borate [SrB_4O_7:Eu(II)] functions as a light lure in insect traps, and is used in reprographic systems and "black lights" [1].

Inorganic single crystals provide another medium for the interaction of light and matter. We are familiar with the red beams of light installed under check-out counters that are used to read the bar codes on items of purchase. Less familiar yet important applications of solid-state light emission include hand-held surgical beams, knives made of light, for retinal repair, and intense beams that can cut steel plate. The acronym "laser" is in common use for this "**l**ight **a**mplification by **s**timulated **e**mission of **r**adiation" and designates a use for solid-state materials

that is as important as phosphors. The original discovery of laser light was a coherent beam of red light from a ruby crystal mounted within a coiled flashlamp [2].

My desire to discover and prepare new compounds that will find use as phosphors and laser crystals has motivated my work. The effort to discover new materials has been focused primarily by two factors. These are the need to tailor the solid/light interaction so that desirable optical compounds result, and the need to produce congruent materials that can be grown as large single crystals directly from the melt. Single crystals are needed for evaluation as laser crystals and for spectroscopic studies such as ground-state and excited-state absorption that cannot be done on microcrystalline powders. Within this focus I have emphasized exploratory synthetic work, thermal and phase analysis, and luminescence characterization.

In the remaining portion of this introduction I present the background information that is necessary to understand the emission characteristics of solid-state materials. I explain the reasons that I chose the system $SrO-Sc_2O_3-B_2O_3$ for exploratory synthesis followed by description of the results achieved. Finally the newly discovered borates will be structurally compared to existing borates, and the general synthetic technique discussed.

Absorption and emission spectra from electronic processes in transition and rare earth metal cations may be observed when these cations are present in solid-state hosts in large amounts or at doping-level concentrations. My work has involved primarily the transition-metal ion Cr^{3+} as a dopant. The characteristics of its spectra are strongly influenced by the symmetry of the coordination site occupied by the metal and the crystal-field strength imposed by the host matrix on the electrons of the metal. The host dependence of Cr^{3+} lasing characteristics in vibronic laser materials is especially important in planning an exploratory synthetic effort. Spectra and data are presented that show smaller substitutional sites in host crystals tend to produce a stronger field strength for the Cr^{3+} site which shifts λ_{max} [3] of the emission band to shorter wavelengths. Emission spectra of new materials presented in succeeding chapters of the thesis will be compared to known cases. Other factors such as electron-phonon coupling characteristics and excited state absorption must also be considered.

Interpreting Cr^{3+} optical characteristics begins with consideration of the Tanabe-Sugano diagram [4] shown in Figure 1.1. In this diagram the normalized energy of excited electronic states in Cr^{3+} (E/B) is plotted relative to the normalized crystal-field strength (Dq/B) possessed by the host crystal. In this method of

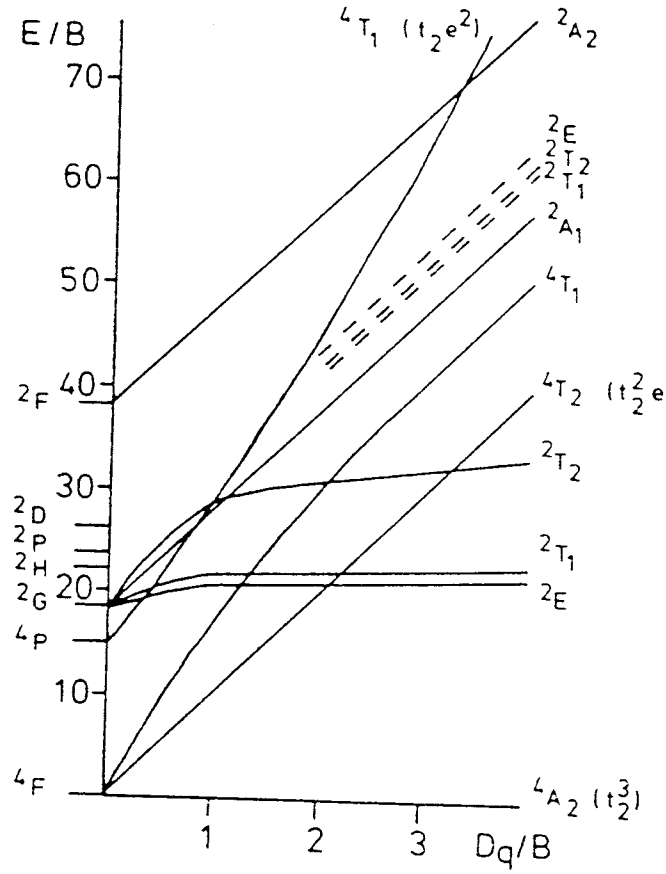

Figure 1.1. Tanabe-Sugano energy level diagram for Cr^{3+} ion (d^3) in an octahedral environment

presenting data B is the interelectronic repulsion term which allows different ions with the same number of d electrons to be represented by the same diagram. The terms on the ordinate of the diagram indicate the excited energy levels for a free ion. Crystal-field strength applied by the host material containing the cation affects the separate terms uniquely as seen by the differing slopes of the excited states. The more a particular state interacts with the atoms of the host environment and is affected by the crystal field applied by those atoms, the larger the slope is. A state largely unaffected by the strength of the crystal field has a slope parallel to the abscissa.

Electronic states that are strongly coupled to lattice vibrations such as $^4T_2$ and $^4T_1$ have large positive slopes relative to the $^4A_2$ ground state and states that are coupled poorly or not at all to lattice vibrations such as ^2E have small slopes relative to the ground state. To make this more apparent the $^4A_2$ level has been made commensurate with the abscissa of the plot. Cr^{3+} absorption occurs primarily by way of the spin-allowed $^4A_2 \rightarrow {}^4T_2$ and $^4A_2 \rightarrow {}^4T_1$ transitions. Once the ion has been excited to higher electronic states energy is lost via nonradiative processes and emission finally occurs from the lowest excited state in the form of a broad band, sharp peaks, or a combination of both depending on the

crystal-field strength of the host.

To understand the origin of these features it is necessary to examine the physical nature of the ground and excited states of the ion. A diagram of the d-orbital energy levels in Cr^{3+} under different conditions is given in Figure 1.2. At the left is shown three electrons populating five degenerate energy levels for the free ion. Next is shown the splitting of the five d-orbitals into a lower energy t_{2g} set (d_{xy},d_{xz},d_{yz}) and the higher energy e_g set (d_{z^2},$d_{x^2-y^2}$) when the central Cr atom is bonded to six O atoms in an octahedral configuration. This splitting is the direct result of the orientation of the d-orbitals relative to the O ligands.

If the CrO_6 complex is placed in a Cartesian frame of reference with the central Cr^{3+} ion at the origin and the six O atoms along the x, y, and z axes, the d-orbitals are split into the t_{2g} set with lobes oriented off the Cr-O bond vectors and the e_g set with lobes on the Cartesian axes in the Cr-O bond regions. The three electrons in the ground state occupy the three lowest t_{2g} orbitals in obedience to Hund's rule of maximum multiplicity.

To the right in Figure 1.2 are shown the two different lowest excited state configurations that can result when an electron gains the energy from an absorbed photon. In the ^4T excited state pairing energy is greater than promotion energy so the excited electron is promoted

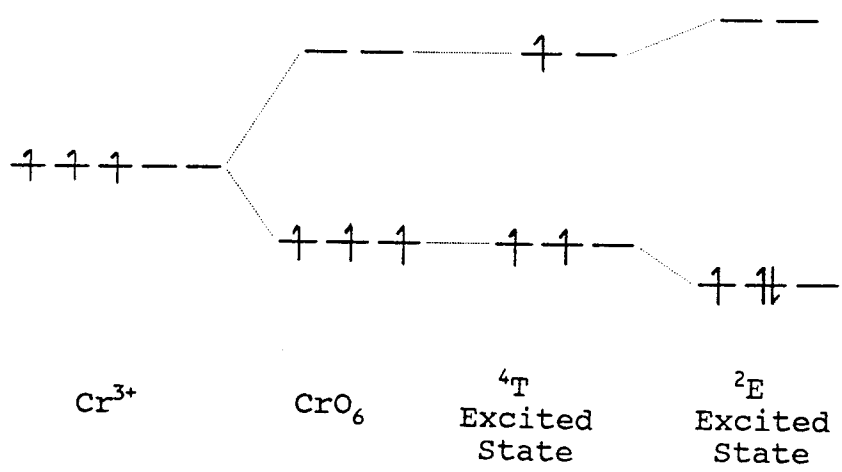

Figure 1.2. Schematic representation of d-orbital energy levels for four differerent cases (left to right): free ion state, ion in octahedral environment, ^4T excited state, and ^2E excited state

into the upper on-axis e_g set. In the ^2E excited state promotion energy is greater than pairing energy so the excited electron remains in the t_{2g} set. The latter excitation consists of a spin-flip that results in pairing.

The extent that electronic transitions couple to lattice vibrations results from the physical interaction of electrons in an optically active ion with the bonding electrons of the host lattice. An electron excited into one of the e_g orbitals will feel repelled by the Cr-O bond pairs more than an electron going into one of the t_{2g} orbitals. Since the ^2E excited state involves only spin pairing of one of the three d electrons in the t_{2g} set, the higher energy on-axis d_{z^2} and $d_{x^2-y^2}$ orbitals of the e_g set are not involved in the transition. As a result the transition is not strongly coupled to lattice vibrations and a sharp peak results. If an electron is promoted into the e_g set as in the $^4T_2$ excited state it is now in the region of Cr-O bonding density and is strongly affected by lattice vibrations. A whole manifold of vibrational phonons is imposed on the energy of the excited electron directly though the lattice O atom and broad band emission results from termination on various vibrational levels of the ground state.

To show these two features a schematic representing the emission spectra of $Cr^{3+}:YAl_3(BO_3)_4$ taken at three

different temperatures [5] is presented in Figure 1.3. This borate has a crystal field strength that places it higher than the crossover point between the ^2E and $^4T_2$ energy levels on the Tanabe-Sugano diagram. At room temperature the emission spectrum exhibits both a sharp line from the $^2E \rightarrow {}^4A_2$ transition and a broad band from the $^4T_2 \rightarrow {}^4A_2$ transition.

At 535 K there is much more thermal energy available to promote excited electrons from the lowest excited ^2E state into the $^4T_2$ state at higher energy so the intensity of the broad band is even greater relative to the sharp line. Boltzmann statistics are used to describe the distribution of electrons into the ^2E and $^4T_2$ states, explaining the changes in intensity of the broad band with temperature. The higher the temperature the more intense the broad band is relative to the ^2E sharp line. As thermal population of the $^4T_2$ state from the ^2E lowest excited state is eliminated by cooling to 4.2 K the broad band disappears. Persistence of the sharp peak at 4.2 K is evidence that the ^2E state is the lowest excited state in this material. If the $^4T_2$ level were the lowest excited state the sharp line would be absent and the broad band emission arising from $^4T_2$ would persist at 4.2 K though with a reduced intensity.

A configurational coordinate diagram that shows both kinds of transitions that occur in the Cr^{3+} ion is

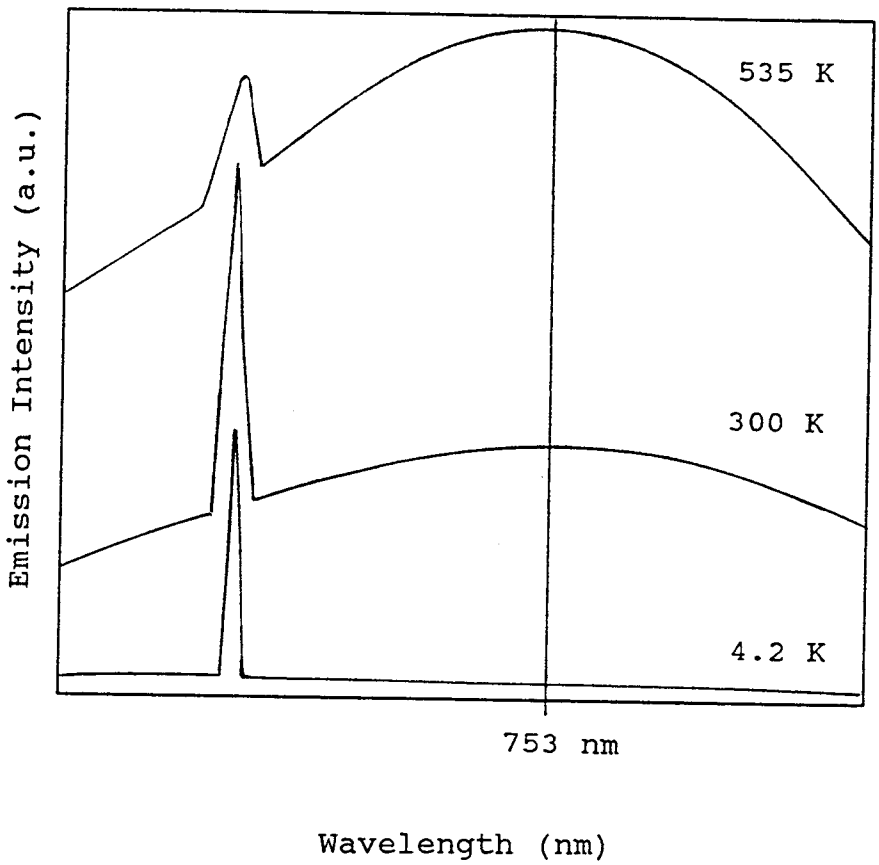

Figure 1.3. Schematic representation of $Cr^{3+}:YAl_3(BO_3)_4$ emission spectra at three different temperatures given in reference 4. Spectra exhibit persistence of sharp line at 4.2 K and variation of broad band intensity with temperature.

given in Figure 1.4. In this diagram potential energy curves representing excited and ground states in a crystalline host are shown relative to the Cr-O bond distance. Displacements of these curves along the abscissa represent the extent of motion of the O atoms away from their equilibrium positions because of electron excitation. On the left side of the diagram the ^2E well is shown undisplaced relative to the ground-state well resulting in a sharp line transition. On the right the upper state $^4T_2$ well is shown shifted to the right because the Cr-O bond lengthens in response to the increased on-axis electron density during excitation of an electron into one of the e_g orbitals. Since excitation of an electron into the ^2E state does not involve leaving the t_{2g} set no relative atomic displacement occurs and the minima of the potential wells remain aligned. Excitation of an electron into the e_g set causes displacement of the excited-state well relative to the ground-state well and involves both excited-state and ground-state vibronic manifolds in the transition. Even though the ^4T state is at a higher energy than the ^2E state, the $^4T \rightarrow {}^4A$ broad band occurs at a lower energy than the $^2E \rightarrow {}^4A$ sharp line because of termination on excited vibrational levels of the ground state in the former transition.

Because of the differing natures of the $^4T_2$ and ^2E states, the characteristics of emission are primarily

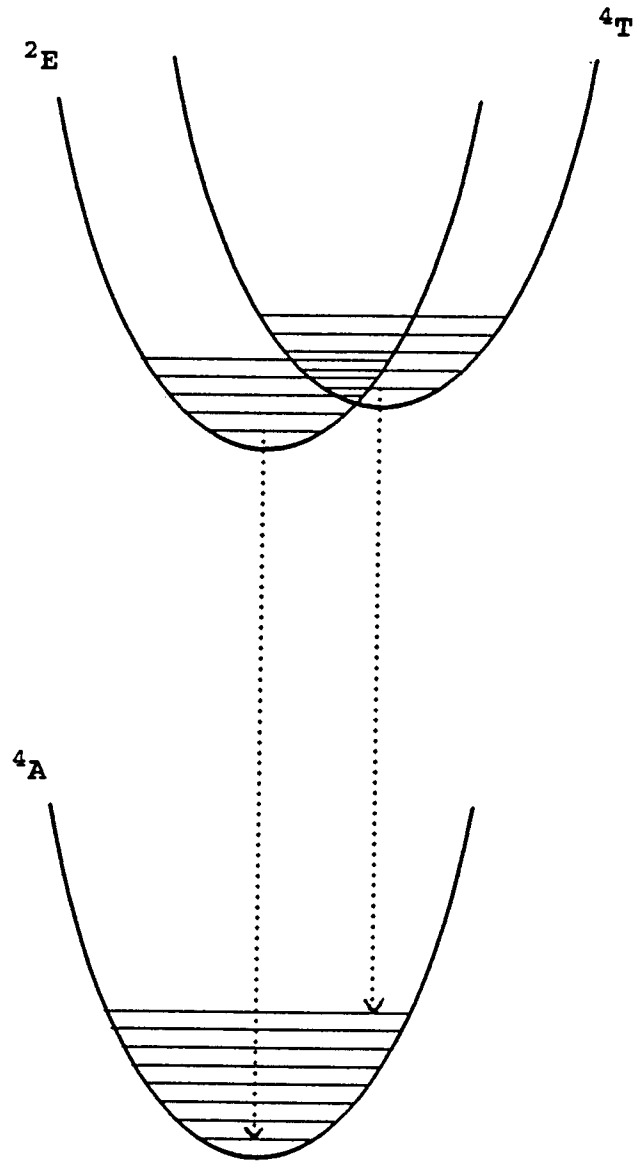

Figure 1.4. Configurational coordinate diagram showing position of ^2E and ^4T excited state energy wells relative to the ^4A ground state well.

determined by whether the host possesses a strong, intermediate, or weak crystal-field strength. Strength of the crystal field imposed by the host material on an emitting ion determines not only the lowest excited state but also the size of the energy difference (ΔE) between the $^4T_2$ and ^2E states. Values for ΔE, λ_{max} for maximum emission intensity, and the parentage of the lowest excited state are listed in Table 1.1. If ΔE is positive as it is for the high field material ruby ($Cr^{3+}:Al_2O_3$) the ^4T state is higher in energy than the ^2E state. If ΔE is negative as it is in the low field material $Cr^{3+}:La_3Lu_2(GaO_4)_3$ (LLGG) the ^4T state is lower than the ^2E state. λ_{max} shifts to the red as the crystal field strength decreases.

For strong crystal-field materials such as ruby ΔE is too large to allow thermal population of the $^4T_2$ state. Instead electrons undergo nonradiative transitions from higher quartet states into the ^2E state and are not subsequently thermally excited into higher levels. Emission from the ^2E state is split into two sharp R-lines because the ^2E state is split by a low-symmetry component of the crystal field [6]. These sharp lines are called "R-lines" because they were first observed in ruby and occur in the red region of the visible spectrum; hence "R" means "red" and is used to designate this particular transition of Cr^{3+} in all host materials. The

Table 1.1. ΔE and λ_{max} of lasing for seven different laser materials.

	ΔE (cm^{-1})	λ_{max} (nm)	L.E.S.[a]
Al_2O_3	2300	694	^2E
$BeAl_2(SiO_3)_6$	400	730	^2E
$YAl_3(BO_3)_4$		730	^2E
$BeAl_2O_4$	800	750	^2E
$Gd_3Sc_2(GaO_4)_3$		768	^4T
$La_3Lu_2(GaO_4)_3$	-900	820	^4T
$ScBO_3$		840	^4T

[a]Lowest excited state

intermediate case as already discussed for $YAl_3(BO_3)_4$ is found in many materials of which alexandrite ($BeAl_2O_4$) and ß-Ga_2O_3 are examples. In weak field materials such as LLGG and $ScBO_3$ the $^4T_2$ state is so much lower than the ^2E state that thermal population of the ^2E state does not occur. As a result sharp zero-phonon peaks are not seen and only the broad band transition is observed.

Since lasing occurs from the same energy states that fluorescence does, broad band laser emission spectra occur in or near the fluorescence regions displayed by photon emitting species in host materials. Hence, fluorescence spectra are one indicator of how a particular material might lase. Comparative spectra for a sequence of Ga garnets have been reported [7]. A schematic representation of this set of comparative spectra is given in Figure 1.5, showing how a gradual increase in crystal field strength shifts λ_{max} for the broad band to higher energies. The graph also demonstrates emergence of the R-lines in this sequence of Cr^{3+} hosts as field strength increases. To reveal the overall trend occurring in this series I have estimated the position of λ_{max} of the broad band from the figure in the reference. The position of λ_{max}, cation radii of the substitutional sites in the different garnets, and the average electronegativity of the host compound are listed in Table 1.2. As substitutional site cations become more electronegative

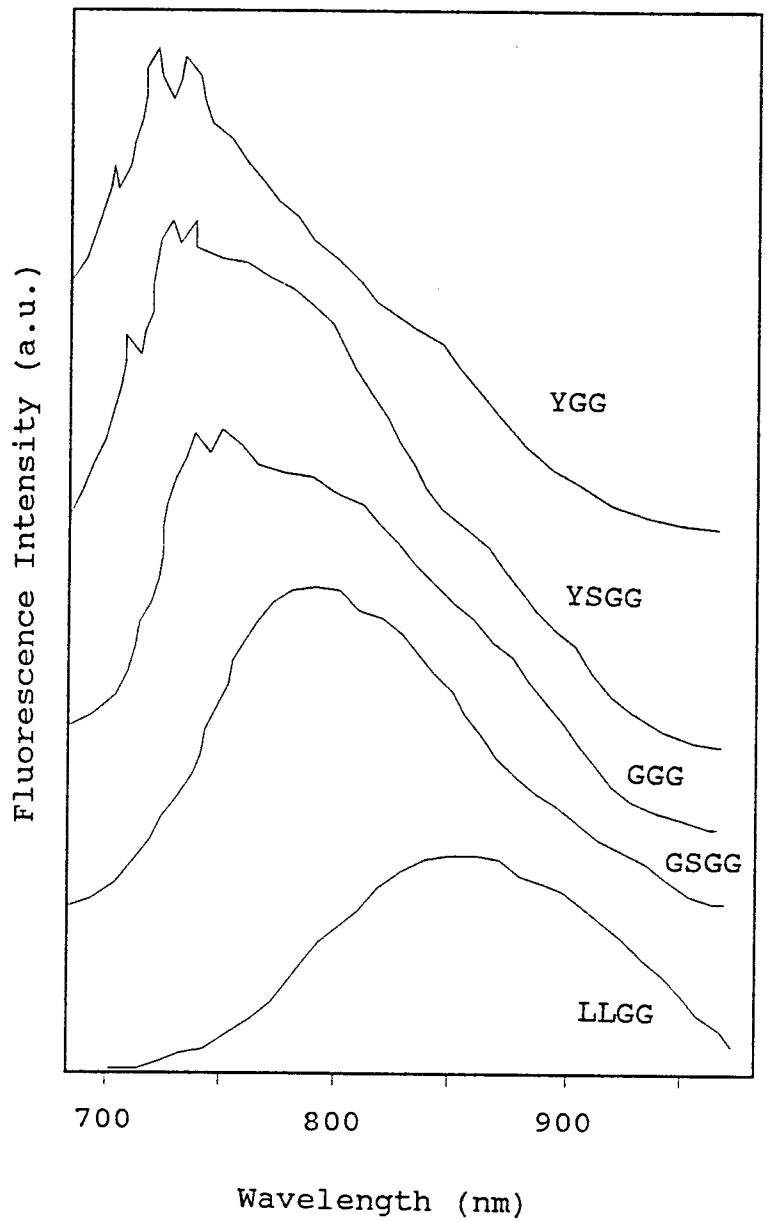

Figure 1.5. Schematic representation of emission spectra for five different gallium garnets plotted together on the same graph given in reference [7]. Acronyms for the five garnets are included with the empirical formulas they stand for in Table 1.2.

Table 1.2. Position of λ_{max} for broad emission band related to substitutional site radius (r) and mean electronegativity (en) for five garnets.

		λ_{max} (nm)[a]	en[b]	r (Å)[c]
$La_3Lu_2(GaO_4)_3$	LLGG	842	2.625	1.001
$Gd_3Sc_2(GaO_4)_3$	GSGG	768	2.635	.885
$Gd_3Ga_2(GaO_4)_3$	GGG	730	2.660	.76
$Y_3Sc_2(GaO_4)_3$	YSGG	724	2.665	.885
$Y_3Ga_2(GaO_4)_3$	YGG	717	2.695	.76

[a]Estimated from spectra in ref. [7]

[b]Computed from Pauling electronegativities

[c]From empirical Shannon radii (Ref. 9)

and smaller the Cr^{3+} ion occupies a smaller site. The Cr-O bond distances are shorter and electron density in the bond regions increases. As a result, the crystal field imposed on the Cr^{3+} d-electrons at the emitting site strengthens and λ_{max} shifts to the blue. A comparison of ΔE (cm^{-1}), the energy difference between the ^2E and $^4T_2$ states, and λ_{max} (Å) has been made for two of the garnets and six other materials which span the range of crystal field strength already in Table 1.1.

Another method of increasing the field strength at the emitting site involves changing the atoms linked through O atoms or BO_3 groups to the substitutional site. Since these atoms do not occupy the site where dopant ions substitute they are called next nearest neighbor atoms. In some materials a larger, more electropositive atom that is a next nearest neighbor will shift electron density toward the substitutional site. The Sr-Sc-B-O compounds discovered in this work are an example. In this case increasing the proportion of the larger more electropositive Sr^{2+} cation in a scandium borate host matrix increases the charge and crystal field strength at the emitting site causing a blue shift of the broad band.

A similar variation in trends is found in sequences of silicate minerals [8]. In the amphiboles of formula $M_2M'_5(SiO_{11})_2(OH)_2$ the $Si\text{-}O_{term}$ bond length gradually increases as electronegativity of the M and M' atoms

increases. Conversely, for the olivines M_2SiO_4 and garnets $M_3M'_2(SiO_4)_3$, the Si-O_{term} bond length gradually decreases as electronegativity increases. The Ga-garnets listed in Table 1.2 behave like the Si-garnets, and the new Sr-Sc-B-O materials are similar to the amphiboles.

Reference to the $YAl_3(BO_3)_4$ spectrum in Figure 1.3 shows that it is an intermediate field strength host for Cr^{3+} based on the presence of the R-lines in its spectrum and λ_{max} being similar to that for emerald. $YAl_3(BO_3)_4$ exhibits an increase in broad band intensity with rising temperature because energy becomes available to thermally populate the $^4T_2$ state which (by inference from emerald) is on the order of 2kT above the ^2E level. Similarly $ScBO_3$ is seen to be a weak-field material because of complete disappearance of the R-line and occurrence of λ_{max} at 800 nm. If $ScBO_3$ is compared to $YAl_3(BO_3)_4$, the average cation radii are 0.518 Å and 0.458 Å respectively [9]. Again, a decrease in overall cation size giving a stronger crystal field at the Cr^{3+} site is consistent with the observations made for the garnet sequence.

Another mechanism that affects stimulated emission displayed by metals in oxide host lattices during lasing is excited state absorption (ESA). This phenomenon occurs when photons interact with excited-state electrons and promote them to higher energy levels rather than stimulate emission. An example of this is found in ruby in which

two different sets of sharp ESA peaks have been identified as the spin-allowed $^2E \rightarrow {}^2A_1$ and $^2E \rightarrow {}^2A_2$ transitions [10]. Location of these transitions can be found at high field strength (≈3.0 Dq/B) in the Tanabe-Sugano diagram given in Figure 1.1. The lower frequency pair of ESA peaks corresponding to the $^2E \rightarrow {}^2A_1$ transition are the R_1 and R_2 lines occurring in the red at 667.4 nm and 666.2 nm. The higher frequency pair corresponding to the $^2E \rightarrow {}^2A_2$ transition are the R_1 and R_2 peaks that occur in the UV at 364.4 nm and 364.0 nm. The authors report these peaks are separated by an amount of energy (≈29 cm^{-1}) comparable to the separation between the R_1 and R_2 emission peaks. This is the energy separation reported for the two R-lines of the ^2E state which has been split into two levels by a low-symmetry component of the crystal field [11]. Ruby also displays broad band ESA at elevated temperatures (663 K) because of vibronic coupling of e_g electrons to lattice modes of vibration [12]. These ESA mechanisms are the primary reason slope efficiency for the ruby laser is less than 1%.

Another example of laser output reduction from ESA has been studied in alexandrite which has an ESA band that partially overlaps its emission band [13]. Even with this reduction the alexandrite laser is the third most efficient solid-state laser with 51% slope efficiency [14]. The overlap of ESA with emission is also

responsible for the position of λ_{max} for the laser emission band. Alexandrite displays λ_{max} for fluorescence at ≈715 nm and peak lasing wavelength at ≈760 nm at 28 °C [13]. The shift in λ_{max} of approximately 45 nm when going from unstimulated to stimulated emission arises from the ESA induced by pumping of the laser crystal. A schematic representation of the ESA and emission cross sections for alexandrite laser crystal from reference [13] is given in Figure 1.6. This representation exhibits an ESA minimum at 13000 cm^{-1} in the lasing band region with absorption increasing more rapidly to the shorter wavelength end of the spectrum. Removal of excited state electrons from the blue end of the fluorescence spectrum shifts λ_{max} for the stimulated emission band to the red. A similar comparison for emerald shows a small amount of overlap between the emission and ESA bands [12]. This allows the emerald laser to be an efficient solid-state laser with slope efficiency measured at 39 % and 51 % depending on output coupling [14].

Both of these laser materials show that placing Cr^{3+} into an intermediate crystal field host improves lasing efficiency over the high field host such as ruby. The intermediate field strength brings the electronic energy levels in the Cr^{3+} ion nearer to the crossover point for the $^4T_2$ and ^2E states so that the next lowest excited state ($^4T_2$) is thermally accessible from the ^2E state.

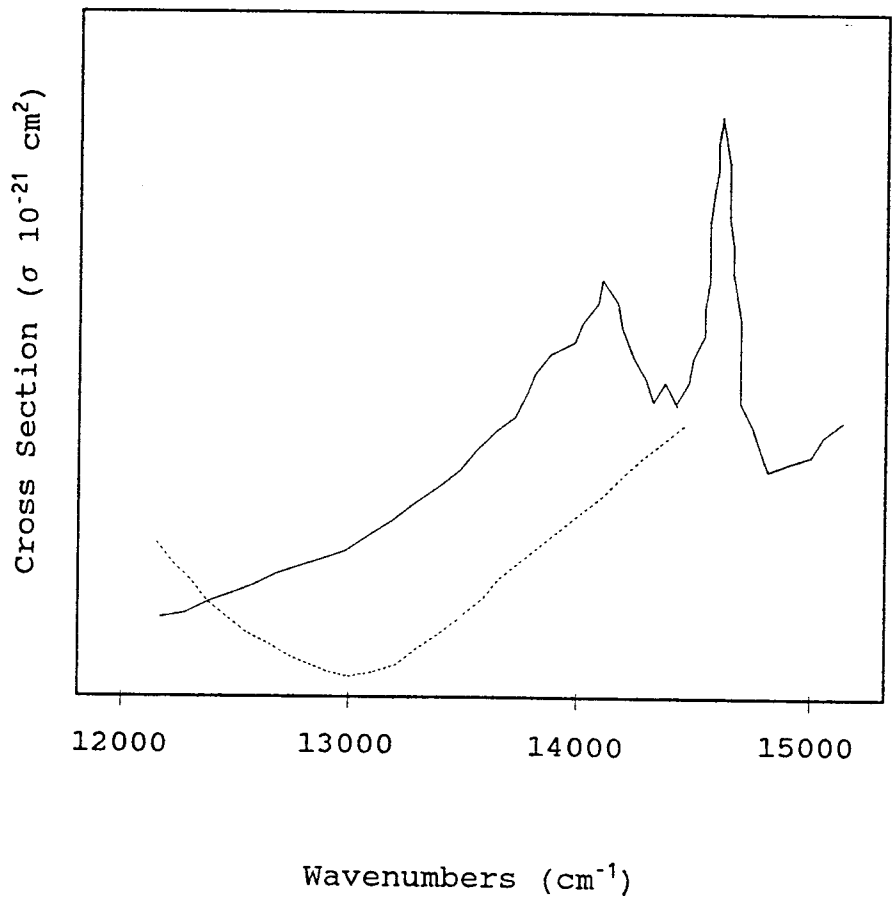

Figure 1.6. Schematic representation of alexandrite ESA (dotted line) and emission (solid line) cross sections plotted together in reference [13]. ESA cross section exhibits intensity minimum at 13000 cm^{-1}.

There is also less overlap of ESA and emission bands for an intermediate field strength material. Overlap of stimulated emission bands with ESA bands results in the small slope efficiencies of low field materials such as YSGG and LLGG (both < 5%) as well [15]. Evidence for the highest efficiency materials occurring at intermediate field strengths is also seen in the garnet sequence listed in Table 1.2 and schematically represented in Figure 1.5. Although slope efficiency is $\leq$ 10% for the other four garnets, the maximum slope efficiency of 28% is displayed by GSGG which has $\Delta E \approx 0$, placing it near the overlap of the two levels.

The background material presented above is necessary to explain why the SrO-Sc_2O_3-B_2O_3 phase system was chosen for study. The primary reason for searching this phase system is because the weak-field borate Cr^{3+}:$ScBO_3$ is the sixth-most efficient solid-state laser known to date [16]. If $ScBO_3$ has some ESA/stimulated emission overlap it could be possible to increase its efficiency even more by shifting the position of the emission band. Specifically, presence of the electropositive Sr atom in a scandium borate host could shift the emission band away from the ESA band. A hypothesis was formed that Sr would increase the crystal field strength at the Sc^{3+} (Cr^{3+}) site. Increasing the field strength surrounding the Cr^{3+} ion would squeeze the three Cr d-electrons more than they are

in the solid-state laser host $Cr^{3+}:ScBO_3$ and this would increase the energy of the transitions they undergo. As a result the fluorescence band would be shifted toward the higher energy blue end of the spectrum and away from the ESA band which would not be shifted as much. Research detailed in this thesis confirms the hypothesis to be true for several of the new materials.

$Cr^{3+}:ScBO_3$ plus other borates such as $Nd^{3+}:YAl_3(BO_3)_4$ that have been made to lase point to borate materials as being a likely source of new efficient laser crystals in the future. Many borates have good crystal growth properties necessary to the production of single crystals used as lasers. These properties include congruent melting which allows single crystals to be pulled or grown directly from the melt, and moderate to high melting points (960 °C to 1560 °C). Many borates are resistant to thermal shock and have high optical damage thresholds; they are also transparent which allows bulk emission necessary for the lasing process.

Sc_2O_3 was chosen to be part of the phase system because Sc has no d-electrons and has a suitable size and charge for Cr^{3+} doping. Correct interpretation of spectra requires that host cations have no d electrons so it is known that all observed spectroscopic properties are the result of the dopant ion.

SrO was chosen to be a member of the phase system to

supply the electropositive Sr and because SrO would enhance reactivity in a mixture. SrO is a basic oxide and would aid crystal growth and stability because a stoichiometric melt for growth of a single crystal would include the two basic oxides SrO and Sc_2O_3 and the acidic oxide B_2O_3.

Initial efforts to discover new materials in the SrO-Sc_2O_3-B_2O_3 phase system involved mixing the three components in various molar ratios occurring in the central part of the phase triangle and employing standard solid-state synthetic methods to see if any new compounds formed. The positions of the discovered compounds are shown in the phase triangle given in Figure 1.7. Powders of each of the materials discovered during this research can be synthesized by standard solid-state methods. Stoichiometric ratios of the starting materials (oxides, nitrates, oxalates, and carbonates) are ground together and heated at 923 K for 1-2 hr to decompose all reagents to the oxides. The starting mixture includes 5 mol % excess B_2O_3 which is kept in a drying oven at 410 K. This is necessary to ensure formation of the desired product if some of the B_2O_3 is lost to volatilization. Then the oxide mixture is reground and flash-heated at a higher temperature ranging from 1123 to 1323 K and annealed 4-6 hr, depending on the sample. Once the sample has sintered powder X-ray diffraction patterns are taken to

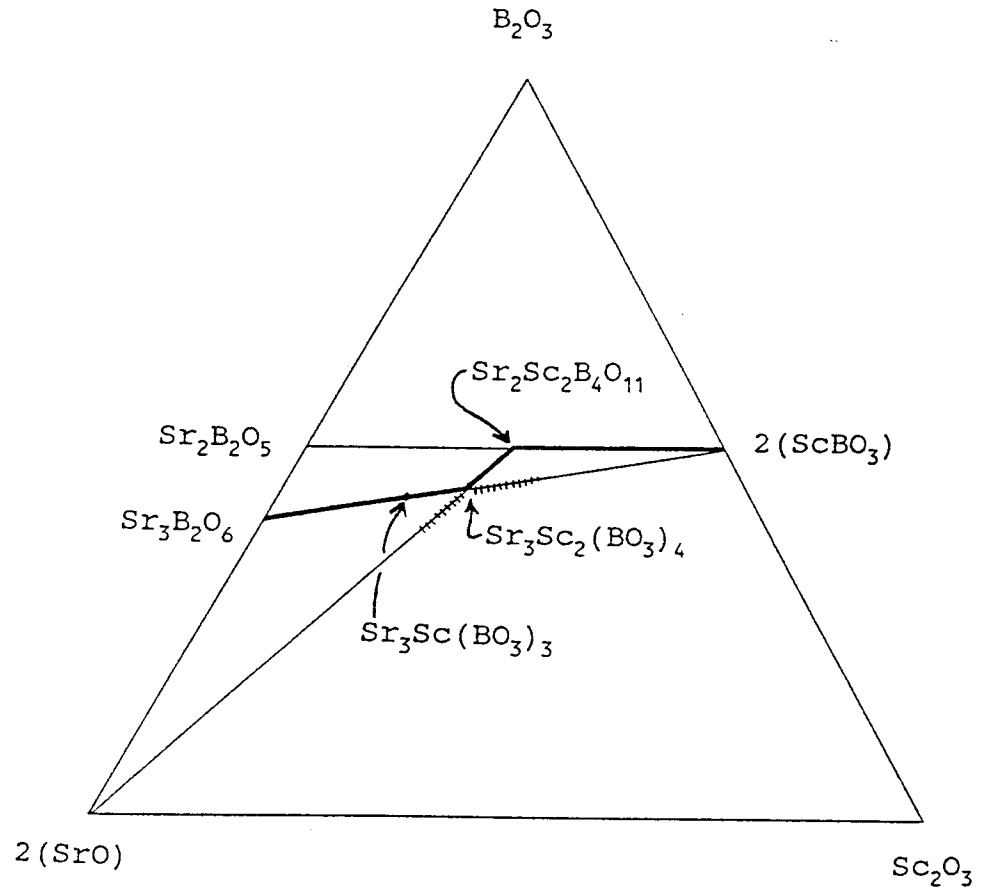

Figure 1.7. $SrO-Sc_2O_3-B_2O_3$ Phase Triangle showing location of the three new materials discovered in this phase system. Equilibrium mixtures of stable components were achieved on the three heavy phase lines.

evaluate product purity. If unwanted phases are found in the sample after flash-synthesis or if the sample melts, a step-wise heating method has to be used. In this alternate method, after the initial decomposition step the sample is reground and reheated starting at a lower temperature such as 1023 K. Each time the temperature is increased by 50 K until sintering occurs.

Three new materials were discovered and grown in microcrystalline form. Structure determinations were achieved for the orthoborate $Sr_3Sc(BO_3)_3$ and the mixed orthoborate-pyroborate $Sr_2Sc_2(BO_3)_2(B_2O_5)$. Unit cell parameters were obtained for the orthoborate $Sr_3Sc_2(BO_3)_4$. All new materials discovered during this research are built up of either or both of the borate structural units shown in Figure 1.8. The orthoborate group BO_3^{3-} adopts a triangular planar arrangement with O-B-O angles near 120° as the O atoms maximize their interatomic distances. Three σ-type bonding M.O.'s and a delocalized π-type bonding M.O. make the bond order = 1.33 for each B-O bond. Solid-state materials built up of this structural unit are often layered structures because of the planarity of the group itself and because extra electron density to complete the octet for the central B atom comes from the O atoms. An additional bond pair coming from above or below the triangular plane of the group would actually transform it into a tetrahedral BO_4^{5-} group. Many

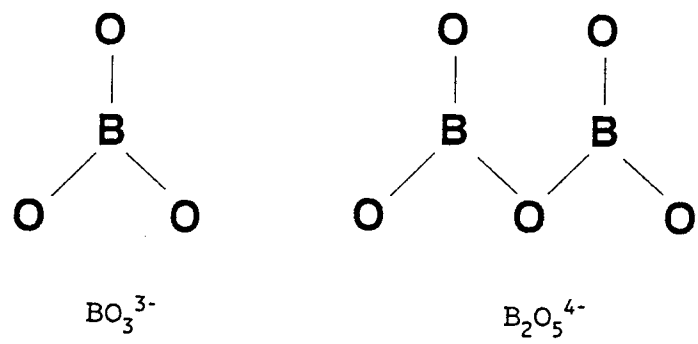

BO_3^{3-} $B_2O_5^{4-}$

Figure 1.8. Diagrams representing the orthoborate (BO_3^{3-}) group and the pyroborate ($B_2O_5^{4-}$) group.

materials containing BO_3^{3-} groups as their basic borate unit are detailed in the literature, including $ScBO_3$ [17] and the huntite $NdAl_3(BO_3)_4$ [18].

The pyroborate group, $B_2O_5^{4-}$, occurring in the compound $Sr_2ScLi(B_2O_5)_2$ is the simplest condensation of two BO_3 groups with each other. In this group the σ- and π-bonding M.O.'s around each B atom are nearly the same as they are in the BO_3 group. Results presented later in this thesis show that the two BO_2-ends of the pyroborate group are bonded independently of each other giving rise to free rotation of the two borate planes relative to each other. The pyroborate group is seen to adopt a wide range of pivot and interplanar angles in different materials. Structural details of pyroborates including $Tl(NbO)B_2O_5$ [19], $Na_4B_2O_5$ [20], $Sr_2B_2O_5$ [21], and $Co_2B_2O_5$ [22] can be found in the literature. Geometries of both of these groups will be discussed in more detail in succeeding chapters. The new material $Sr_2Sc_2B_4O_{11}$ presented in this work has its B-O framework composed of both BO_3 and B_2O_5 groups, the first known example of intermixing of orthoborate and pyroborate groups in a single structure.

DTA experiments were performed to determine the liquidus lines and single phase melting points along three of the two-phase lines that are drawn between end-members in the triangle. Equilibrium mixtures of stable components were found to persist in DTA samples on the

heavy phase lines marked in the diagram in Figure 1.7. Efforts to establish liquidus lines for the $Sr_3B_2O_6$-$Sr_3Sc_2(BO_3)_4$, $Sr_3Sc_2(BO_3)_4$-$Sr_2Sc_2B_4O_{11}$, and $Sr_2Sc_2B_4O_{11}$-$ScBO_3$ phase lines were successful because of this. Mixtures on the cross-hatched lines between $Sr_3Sc_2(BO_3)_4$ and $ScBO_3$, and between SrO and $Sr_3Sc_2(BO_3)_4$ did not form ratios of the stable end-members but in each case moved over to form end-members on the heavy lines. As a result it was not possible to establish the phase line on both sides of $Sr_3Sc_2(BO_3)_4$ that would determine it to be either congruent or incongruent in its melting characteristics. The melting point for $Sr_3Sc(BO_3)_3$ is at a local maximum on the $Sr_3B_2O_6$-$ScBO_3$ phase line, indicating the material melts congruently.

Results from the discovery, structure solution, and optical properties of $Sr_3Sc(BO_3)_3$ are presented in Chapters 2, 3, and 4. Since $Sr_3Sc(BO_3)_3$ was found to be only one member of a large structural family of oxide, the next two chapters present work involved with the preparation and selected properties of this family. Discovery of the family is reported in Chapter 5, and in Chapter 6 I present solid-solution behavior and luminescent properties of selected members of the family. I include a list of the 43 members that I synthesized during this work.

The mixed orthoborate-pyroborate $Sr_2Sc_2B_4O_{11}$ is

presented in Chapter 7 and a previously published paper on the very first material discovered during this work, $Sr_2ScLiB_4O_{10}$, is given in Chapter 8. Appendix 1 contains the unit cell parameters and indexed powder diffraction pattern for the new rhombohedral borate $Sr_3Sc_2(BO_3)_4$ that crystallizes in a very large unit cell. In Appendix 2 I give the unit cell parameters and powder diffraction pattern obtained for a unique trigonal borate, $LiSrY_2(BO_3)_3$.

References

[1] Kirk-Othmer: Encyclopedia of Chemical Technology, John Wiley & Sons, Inc. **14**, 527 (1981).

[2] T. H. Maiman, Nature **187**, 493 (1960).

[3] λ_{max} here and throughout the thesis designates the wavelength having the highest luminescence intensity.

[4] Y. Tanabe and S. Sugano, J. Phys. Soc. Jpn. **9**, 766 (1954).

[5] F. Kellendonk, T. van den Belt, and G. Blasse, J. Chem. Phys., **76(3)**, 1194 (1982).

[6] D. Vivien, B. Viana, A. Revcolevschi, J. D. Barrie, B. Dunn, P. Nelson, and O. M. Stafsudd, J. Lumin. **39**, 29 (1987).

[7] A. Budgor, New Lasers for Analytical and Industrial Chemistry **SPIE 461**, 62 (1984).

[8] F. Liebau, Structural Chemistry of Silicates, Springer-Verlag, Berlin, p. 48 (1985).

[9] R. D. Shannon, Acta Cryst., **A 32**, 751 (1976).

[10] T. M. Dunn and A. H. Francis, Phys. Rev. Lett., **25**, 705 (1970).

[11] G. P. Morgan, T. J. Glynn, G. F. Imbusch and J. P. Remeika, J. Chem. Phys. **69**, 4859 (1978).

[12] J.C. Walling, In Topics in Laser Physics, Tunable Lasers, Eds.: L.F. Mollenauer and J.C. White, Springer-Verlag, Berlin, **59**, p. 331 (1987).

[13] M. L. Shand and J. C. Walling, IEEE J. Quantum Elec., **QE-18**, 1152 (1982).

[14] S.T.Lai, SPIE High Power and Solid State Lasers, **22**, 146 (1986).

[15] S. A. Payne, L. L. Chase, L. K. Smith, W. L. Kway, and H. W. Smith, J. Appl. Phys., **66(3)** 1051 (1989).

[16] S. T. Lai, B. H. T. Chai, M. Long, and R. C. Morris, IEEE J. Quantum Elec. **QE-22**, 1931 (1986).

[17] D. A. Keszler and H. Sun, Acta Cryst. **C44**, 1505 (1988).

[18] H. Y-P. Hong and K. Dwight, Mat. Res. Bull., **9**, 1661 (1974).

[19] M. Gasperin, Acta Cryst., **B30**, 1181 (1974).

[20] H. König, R. Hoppe, and M. Jansen, Z. anorg. allg. Chemie, **449**, 91 (1979).

[21] H. Bartl and W. Schuckmann, Neues Jahrb. Mineral., **8**, 253 (1966).

[22] S. Berger, Acta Chem. Scand., **4**, 1054 (1950).

CHAPTER 2

THE NEW BORATE $Sr_3Sc(BO_3)_3$

Paul D. Thompson and Douglas A. Keszler*

Department of Chemistry and
Center for Advanced Materials Research
Oregon State University
Gilbert Hall 153
Corvallis, Oregon 97331-4003

Chem. Mater. 1, 292 (1989)

Sir:

Energy efficiency has long been an important and critical issue in the development of the science and technology of solid-state lasers, particularly in high-power systems. Additional interest in efficiency and efficient crystalline laser materials has recently developed from the potential to realize new and improved laser characteristics in laser-pumped laser geometries. For example, new compounds doped with the ion Cr^{3+} are of particular interest as potentially efficient lasers for high-intensity pumping and ground-state depletion of Nd^{3+} and other laser crystals [1].

We are involved in the systematic synthesis and study of new solid-state materials that will serve as hosts for the realization of small excited-state absorption cross sections when doped with the ion Cr^{3+}. Excited-state absorption has been reported to be the primary effect limiting the overall energy efficiency of several solid-state lasers operating from a d^3 transition-metal cation [2,3]. In this communication, we briefly describe our approach to synthesizing one class of these materials, complex scandium borates, presenting as an example the new compound $Sr_3Sc(BO_3)_3$.

The reported slope efficiency, 29%, of the laser material $Cr^{3+}:ScBO_3$ [4] ranks sixth among all Cr^{3+} lasers, providing a performance that is better than would be

predicted from consideration of the position (810 nm) of its maximum fluorescence intensity in the context of simple models of excited-state absorption for a d^3 cation [1,2,5]. Given the high efficiency of this material with what appear to be less than optimal optical features, it is likely that an even higher efficiency could be achieved if the characteristics of the scandium borate host were improved. One such characteristic would be an increase in the crystal field at the Sc site to blue-shift the luminescence band relative to that of the excited-state absorption band thereby reducing their overlap.

We have realized the blue-shift in new complex scandium borates containing basic cations. These cations increase the charge on the borate groups relative to those in the compound $ScBO_3$, affording a larger crystal field (more bonding electron density) at the Sc^{3+} (Cr^{3+}) center and the desired shift of the luminescence band [6]. The peak in the luminescence spectrum of the compound $Sr_3Sc(BO_3)_3$ doped to 2 mol% with the ion Cr^{3+} occurs at 750 nm (Figure 2.1), a blue-shift of approximately 60 nm relative to that of Cr^{3+}:$ScBO_3$. This peak compares with the maxima, 775 nm and 875 nm, that we observe in the borates Cr^{3+}:$Sr_2ScLi(B_2O_5)_2$ [7] and Cr^{3+}:$LaSc_3(BO_3)_4$ [8], respectively,and to the maxima near 750 nm reported for the efficient laser crystals Cr^{3+}:$LiCaAlF_6$ [9] and Cr^{3+}:$Be_3Al_2(SiO_3)_6$ [10]. We note the blue-shift observed

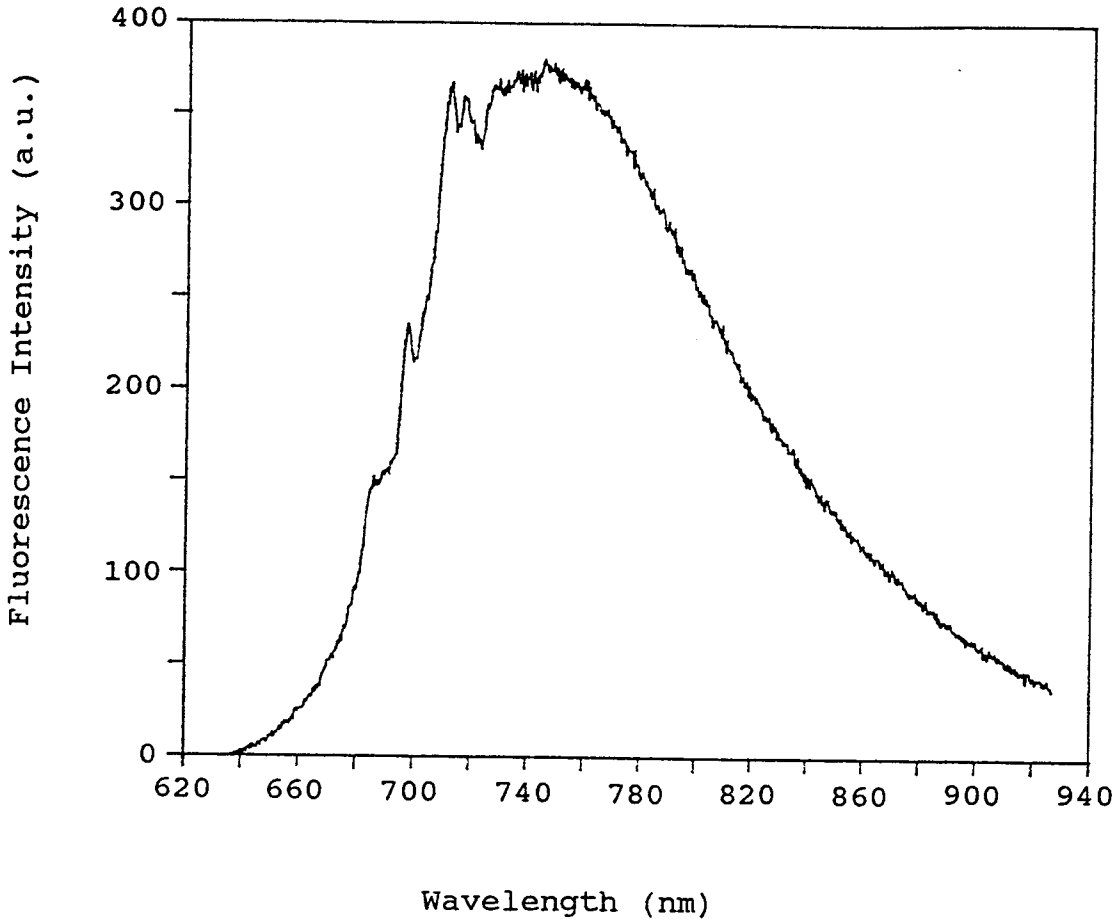

Figure 2.1. The luminescence spectrum of Cr^{3+}-doped $Sr_3Sc(BO_3)_3$ with excitation at 514.5 nm from an Ar^+ laser. The fluorescence intensity is given in arbitrary units here and in all succeeding figures.

in the borates as the average electronegativity of the matrix decreases.

The title compound was identified from our analysis of phase equibrilia in the system $SrO-Sc_2O_3-B_2O_3$. The single crystal used for the determination of the structure was grown from a melt of composition 40 mol% SrO, 10 mol% Sc_2O_3, 40 mol% B_2O_3, and 10 mol% Li_2O that was cooled from 1313 K to 773 K at 6 K/hour. Additional small single crystals grown by slowly cooling a stoichiometric melt from 1573 K to 1273 K at 5 K/hour exhibit identical lattice parameters. The powder sample used for the fluorescence measurement was prepared by heating a stoichiometric mixture of the reagents $Sr(NO_3)_2$, (99.99%, AESAR), $Sc_2(C_2O_4)_3 \cdot 4H_2O$ (99.9%, ALFA), $Cr(NO_3)_3 \cdot 8H_2O$ (99.99%, AESAR), and B_2O_3 (99.99%, ALFA) at 1223 K for 48 hours to afford a nominal 2% doping level of the Cr^{3+} ion.

The new compound crystallizes as a unique structure in a high symmetry, trigonal space group [11]. Atomic parameters are listed in Table 3.2 (next chapter) and the scandium borate framework is sketched in Figure 2.2. The structure is comprised of triangular BO_3 groups, two crystallographically independent Sc atoms occupying distorted octahedra, and a Sr atom residing in an irregular nine-coordinate site. Unlike the structures of a large number of simple orthoborates that adopt structures similar to calcite and dolomite with discrete

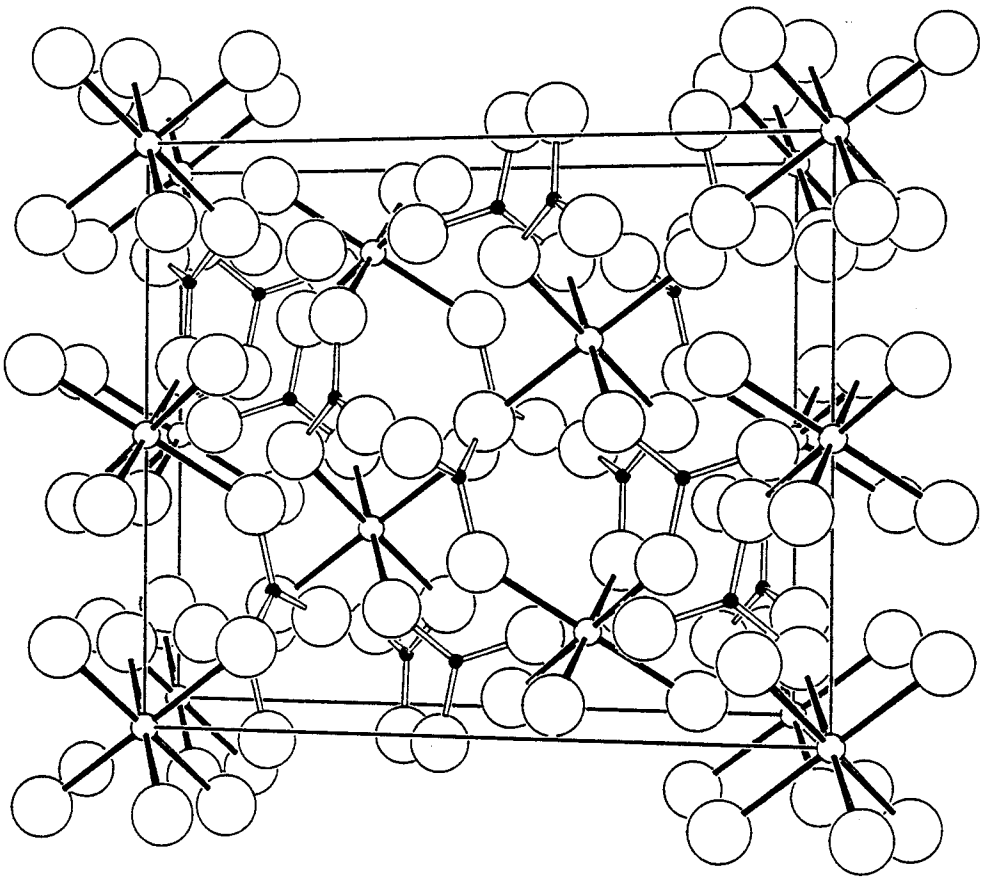

Figure 2.2. Drawing of the scandium borate framework of the compound $Sr_3Sc(BO_3)_3$. The small filled circles represent B atoms and the large open circles represent O atoms. Sc-O interactions are indicated by shaded bonds. The Sr atoms have been removed for clarity.

layers of BO_3 groups interleaved by cations, the present material exhibits a greater isotropic arrangement of the atoms. In particular, it may be noted that the principal atomic planes of the BO_3 groups are aligned approximately parallel to the threefold, **c** axis. The interatomic distances Sc(1)-O(1), 2.077(2) Å, and Sc(2)-O(2), 2.142(2) Å, compare to the value, 2.1200(4), observed in the compound $ScBO_3$ [12]. The small trigonal distortions of the octahedra are demonstrated by the angles O(1)-Sc(1)-O(1), 94.80(7)°, and O(2)-Sc(2)-O(2), 92.28(7)°. The distances Sr-O range from 2.500(2) to 2.857(2) Å.

Since the material is composed of basic oxides (SrO, Sc_2O_3) and a weakly acidic oxide (B_2O_3), the melt of the material is anticipated to be reasonably stable; DTA data indicate that the compound melts at 1250(7)°C. Additional syntheses have revealed that a variety of elements may be stoichiometrically substituted in place of the Sr and Sc atoms. Discussions of the structure and optical characterization of members of this new family of oxides appear in Chapters 3 through 6.

Acknowledgment

This research was supported by the US Department of Energy and Lawrence Livermore Laboratory under contract No. 2143103. The X-ray diffractometer was purchased with funds provided by the US National Science Foundation and by donors of the Foursight! program administered by the Oregon State University Foundation.

References

[1] W.F. Krupke and L.L. Chase, SPIE Int. Soc. Opt. Eng., **Vol. 1040**, in press.

[2] J.A. Caird, S.A. Payne, P.R. Staver, A.J. Ramponi, L.L. Chase, and W.F. Krupke, IEEE J. Quantum Electron. **QE-24**, 1077 (1988).

[3] S.A. Payne, L.L. Chase, and G.D. Wilke, Phys. Rev. B **37**, 998 (1988).

[4] S.T. Lai, B.H.T. Chai, M. Long, and R.C. Morris, IEEE J. Quantum Electron. **QE-22**, 1931 (1986). S.T. Lai, B.H.T. Chai, M. Long, M.D. Shinn, J.A. Caird, J.E. Marion, and P.R. Staver, In Tunable Solid-State Lasers II; A.B. Budgor, L. Esterowitz, and L.G. DeShazer, eds.; Springer-Verlag, Berlin, p. 145 (1986).

[5] L.J. Andrews and S.M. Hitelman, Ettore Majorana Int. Sci. Ser.: Phys. Sci. **30**, 515 (1987).

(6) The shift of the luminescence band is predicted from analysis of the Tanabe-Sugano diagram for a d^3 cation. An even stronger crystal field should afford a substantial population of the excited ^2E level. This population is likely to inhibit laser action, since the $^2E \rightarrow {}^4A_2$ luminescence is not vibronic in nature, consisting of zero-phonon character; there also exits a greater number of spin-allowed

excited-state absorption transitions for the doublet state (see ref. 5).

[7] P.D. Thompson and D.A. Keszler, Solid State Ionics, **32/33**, 521 (1989).

[8] H. Sun and D.A. Keszler, to be submitted.

[9] L.L. Chase, and S.A. Payne, IEEE J. Quantum Electron., in press.

[10] M.L. Shand and S.T. Lai, IEEE J. Quantum Electron. **QE-20**, 105 (1984).

[11] Crystal and refinement data: space group $R\bar{3}$, a = 12.135(1) Å, c = 9.184(1) Å, V = 1171.3(2) $Å^3$, Z = 6; 725 averaged data with $I > 3\sigma(I)$ and 51 variables; R = 0.018, R_w = 0.022. Single-crystal X-ray diffraction data were collected on a Rigaku AFC6R diffractometer with graphite monochromated Mo Kå radiation to sin θ_{max}/λ = 0.806 $Å^{-1}$.

[12] D.A.Keszler and H. Sun, Acta Crystallogr. C **44**, 1505 (1987).

CHAPTER 3

STRUCTURE OF $Sr_3Sc(BO_3)_3$

Paul D. Thompson and Douglas A. Keszler*

Department of Chemistry and
Center for Advanced Materials Research
Oregon State University
Gilbert Hall 153
Corvallis, Oregon 97331-4003

For Submission to Chem. Mater.

Abstract

The structure of the compound $Sr_3Sc(BO_3)_3$ is described. Crystal data: FW = 484.24 amu, $R\bar{3}$ (#148), hexagonal axes, a = 12.135(1), c = 9.184(1) Å, V = 1171.3(2) $Å^3$, Z = 6, Mo Kα (λ = 0.71069 Å), F(000) = 1332, μ = 206.38 cm^{-1}, T = 296 K, R = 0.018, R_w = 0.022 for 725 averaged reflections. The structure exhibits chains comprised of Sc-centered O octahedra and BO_3 triangles that are bridged by 9-coordinate Sr atoms. Each chain contains two crystallographically independent Sc atoms; the distorted octahedral environment about atom Sc1 is compressed along the trigonal axis, O1-Sc1-O1 = 85.20(7)°, while the environment about atom Sc2 is elongated along the same axis, O2-Sc2-O2 = 92.28(7)°. These angles are consistent with the chemical inequivalence of the environments as determined by their associations with neighboring Sr atoms.

Introduction

This report is the first in a series detailing the crystal chemistry of borates derived from the general formula $A_3M(BO_3)_3$ and represented by the structural types of the parent compounds $Sr_3Sc(BO_3)_3$ and $Ba_3Sc(BO_3)_3$. As we have reported [1], derivatives of the Sr compound now comprise one of the larger structural families of solid-state oxide discovered to date.

Here, following, we describe the structure of the compound $Sr_3Sc(BO_3)_3$, a material that exhibits potentially useful optical characteristics when doped with the ion Cr^{3+} [2]. In the ensuing papers in this series [3,4] we discuss the structure of the compound $Ba_3Sc(BO_3)_3$, the derivatives of both structural types, and the interrelationships between them.

Experimental

Single crystals of the title compound were grown from a melt of composition 40 mol% SrO, 10 mol% Sc_2O_3, 40 mol% B_2O_3, and 10 mol% Li_2O that was cooled from 1313 to 773 K at 6 K/h. Unit cell parameters were determined from least-squares refinement of 20 reflections in the range $17° \leq 2\theta \leq 35°$ that had been automatically centered on a Rigaku AFC6R diffractometer. A check of the Laue symmetry on the diffractometer revealed that the material crystallized in group $\bar{3}$. Crystal data and experimental conditions for the X-ray measurements are given in Table 3.1. Three standard reflections that were measured after each block of 200 data exhibited an overall average excursion of 1.6%.

Calculations were performed on a μVAX-II computer with programs from the TEXSAN system of programs [5]. Final least-squares refinement on F_o included 725 averaged data, 51 variables, and anisotropic thermal parameters on each atom. The largest peak in the final difference electron density map corresponds to 1.3% of a Sr atom. Analysis of the residuals as a function of Miller indices and $|F_o|$ reveals no unusual trends. Final atomic parameters and anisotropic thermal parameters are listed in Tables 3.2 and 3.3, respectively.

Table 3.1. Crystal Data and Experimental Conditions for $Sr_3Sc(BO_3)_3$.

formula	$Sr_3Sc(BO_3)_3$
FW, amu	484.24
space group	$R\bar{3}$
a, Å	12.135(1)
c, Å	9.184(1)
V, Å^3	1171.3(2)
Z	6
F(000)	1332
T of data collection, K	296
ρ_{calcd}, g cm^{-3}	4.12
crystal size, mm	0.1 x 0.1 x 0.15
radiation	graphite monochromated Mo Kα (λ(Kα) = 0.71079 Å)
μ, cm^{-1}	206.38
transmission factors	0.932 - 1.089
scan type	$\omega - 2\theta$
scan width	$\Delta\omega = (1.25 + 0.3\tan\theta)°$
2θ limits	$2° < 2\theta < 70°$
data collected	$\pm h, k, \pm l$
no. unique data	725
p factor	0.03
R_{int}	0.032
extinction coefficient	0.107 x 10^{-6}
no. variables	51
$R_w(F_o)$	0.022
$R(F_o)$ for $F_o^2 > 3\sigma(F_o^2)$	0.018
Error in observn. of unit wt.	0.95

Table 3.2. Atomic Parameters for $Sr_3Sc(BO_3)_3$.

atom	x	y	z	B_{eq}
Sr	0.03998(2)	0.46988(2)	0.30855(2)	0.636(9)
Sc1	0	0	½	0.45(2)
Sc2	0	0	0	0.46(2)
B	-0.1406(3)	0.4699(3)	0.0994(3)	0.65(8)
O1	0.0522(2)	0.1644(2)	0.3809(2)	0.79(6)
O2	-0.1779(2)	0.3683(2)	0.1934(2)	0.72(5)
O3	0.0047(2)	0.2637(2)	0.1865(2)	0.81(6)

Table 3.3. Anisotropic temperature factors for $Sr_3Sc(BO_3)_3$.

	U_{11}	U_{22}	U_{33}	U_{12}	U_{13}	U_{23}
Sr	0.0074(1)	0.0077(1)	0.0079(1)	0.00282(9)	-0.00049(8)	-0.00018(8)
Sc1	0.0061(3)	0.0061	0.0049(5)	0.0031	0	0
Sc2	0.0057(3)	0.0057	0.0061(5)	0.0028	0	0
O1	0.0133(9)	0.0102(8)	0.0073(8)	0.0065(7)	0.0008(6)	0.0014(7)
O2	0.0099(8)	0.0103(8)	0.0086(8)	0.0060(7)	0.0016(6)	0.0019(7)
O3	0.0129(9)	0.0100(9)	0.010(1)	0.0075(7)	-0.0018(7)	0.0002(7)
B	0.006(1)	0.009(1)	0.010(1)	0.005(1)	-0.000(1)	0.000(1)

Results and Discussion

A labeled drawing of the contents of the unit cell is given in Figure 3.1. The structure is simple and readily described as a collection of 1-dimensional chains, Figure 3.2, extending along the *c* axis. Each chain contains Sc-centered distorted octahedra that are linked by triangular BO_3 groups. Two inequivalent Sc sites are present in each chain, and they alternate in their lodgments along the chain axis. The chains, packing according to the rhombohedral centering conditions of the cell, are bridged by Sr atoms occupying 9-coordinate environments. Linkage of these Sr-centered polyhedra in all directions, however, mitigates the anisotropy to be expected from the chain description, affording instead a dense, pure 3-dimensional structure.

Selected interatomic distances and angles are listed in Table 3.4. Atoms Sc1 and Sc2 occupy distorted octahedral sites having S_6 ($\bar{3}$) point group symmetry. The Sc1-O1 distance is 2.077(2) Å and the O1 octahedron is slightly compressed along the trigonal axis, O1-Sc1-O1 = 85.20(7)°. The Sc2-O2 distance, 2.142(2) Å, is longer and the O2 octahedron is now trigonally elongated, O2-Sc2-O2 = 92.28(7)°. These interatomic distances and angles may be compared to the Sc-O distance 2.120(2) Å and the trigonal elongation O-Sc-O = 92.28(1)° observed in the

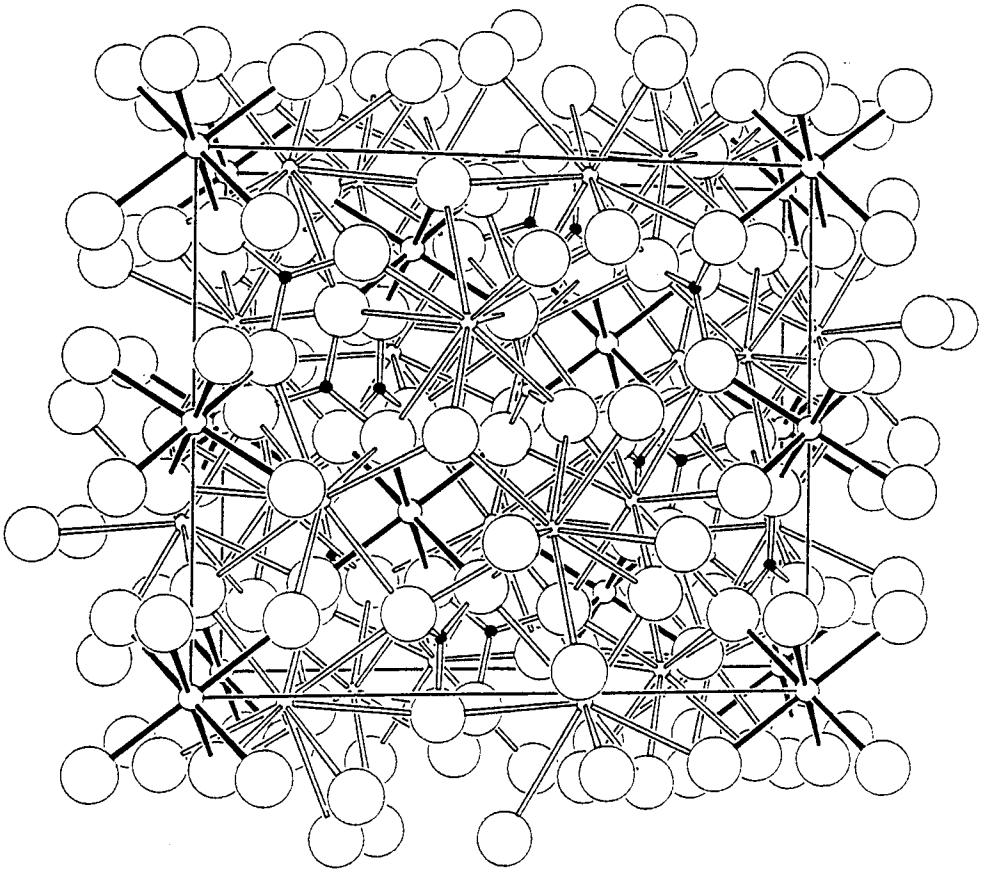

Figure 3.1. Sketch of the contents of the unit cell for the compound $Sr_3Sc(BO_3)_3$. Sr atoms are indicated as small circles with unshaded bonds, Sc atoms as open circles with shaded bonds, B atoms as small filled circles, and O atoms as large circles.

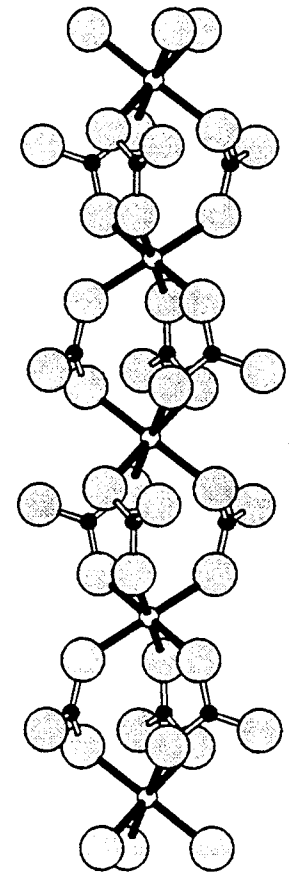

Figure 3.2. Sketch showing how the Sc-centered octahedra form a chain along the **c** axis of the unit cell. The compressed Sc1-O octahedra alternate with the elongated Sc2-O octahedra in the chain.

Table 3.4. Interatomic Distances (Å) and Angles (°) for $Sr_3Sc(BO_3)_3$.

Sr-O3	2.500(2)	O1-Sr-O2	51.20(6)
Sr-O2	2.524(2)	O1-Sr-O1	61.19(7)
Sr-O3	2.574(2)	O2-Sr-O3	70.12(5)
Sr-O1	2.714(2)	O2-Sr-O3	84.48(6)
Sr-O1	2.758(2)	O1-Sr-O2	94.50(6)
Sr-O3	2.760(2)	O2-Sr-O3	109.20(6)
Sr-O2	2.760(2)	O1-Sr-O2	125.40(6)
Sr-O1	2.765(2)	O1-Sr-O2	144.64(6)
Sr-O3	2.857(2)		
Sr-O (avg.)	2.69(12)		
Sc1-O1	2.077(2)	O1-Sc1-O1	85.20(7)
Sc2-O2	2.142(2)	O2-Sc2-O2	92.28(7)
B-O1	1.388(3)	O3-B-O2	121.2(2)
B-O2	1.383(3)	O3-B-O1	119.9(2)
B-O3	1.364(3)	O2-B-O1	118.7(2)
B-O (avg.)	1.38(1)		

compound $ScBO_3$ [6].

The distances and angles in the title compound are consistent with the chemical inequivalence of the two Sc sites. The origin of this inequivalence is best appreciated by considering the associations between the Sc and Sr environments as depicted in Figure 3.3. The O1 octahedron shares triangular faces with Sr-centered polyhedra while the O2 octahedron shares only vertices. Because the symmetry of each O octahedron is S_6, each of the 6 triangular faces of the O1 polyhedron related by the improper rotation axis is shared by a Sr-centered polyhedron and each vertex of the O2 polyhedron is shared by two Sr-centered environments. This results in placement of a distorted octahedron of Sr atoms about the coordination environment of atom Sc1 and a distorted icosahedron about Sc2. The trigonal compression of the O1 octahedron results from the decrease in its edge lengths from face sharing. The trigonal height of the O2 octahedron is determined by the span Sr-(O3···O3)-Sr in conjunction with the metrical and electrostatic requirements of the Sr and Sc atoms; the disposition of atom O3 is largely fixed through its interaction with the B atom to from the triangular planar BO_3 group.

Sr-O distances, 2.500(2) - 2.857(2) Å, are normal with the average length 2.69(12) Å comparing well to the value 2.71 Å computed from empirically derived radii [7].

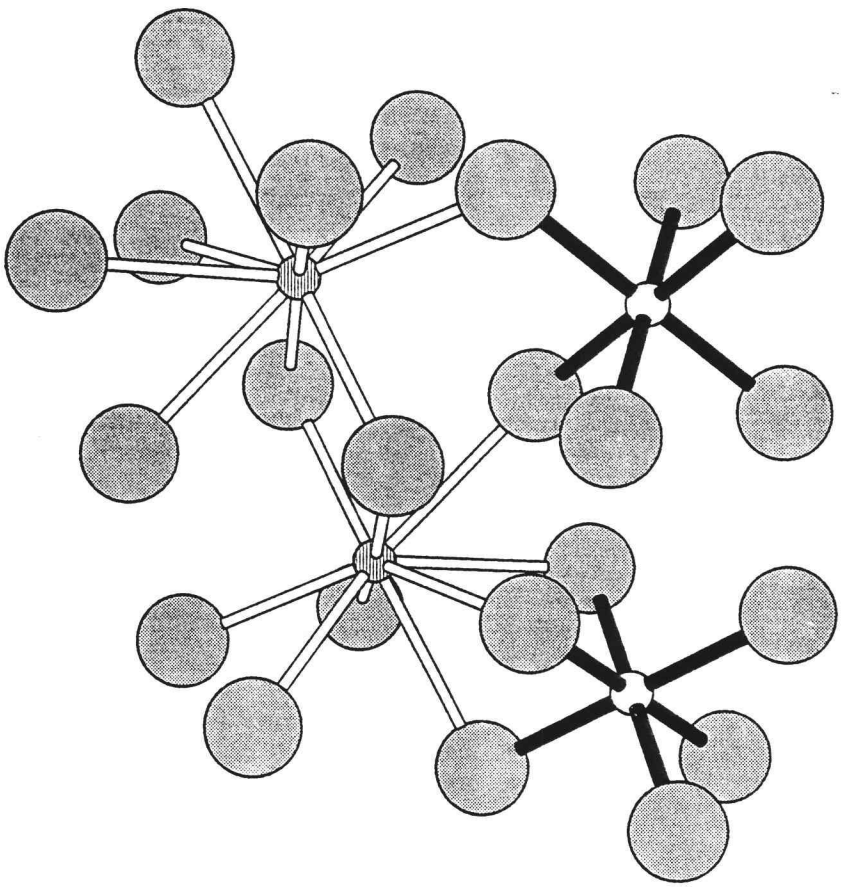

Figure 3.3. A drawing of a portion of the structure of $Sr_3Sc(BO_3)_3$ emphasizing linkages between the Sr- and Sc-centered polyhedra.

By sharing vertices, edges, and faces, each Sr-centered polyhedron associates with 11 other polyhedra of the same type to from a complete three-dimensional network.

The borate group is regular with the average B-O distance 1.38(1) Å comparing well to the value 1.379 Å deduced from crystal radii. The packing of the borate groups, however, is unique, affording the unique pinwheel pattern as seen in the view along the *c* axis in Figure 3.4. This contrasts to the more common packings of orthoborate groups that are typically found in layered-type structures related to calcite, dolomite, and huntite.

Atoms O1 and O3 occupy 5-coordinate sites best described as highly distorted triangular bipyramids; atom O1 binds 3 Sr, 1 Sc, and 1 B (Sc-O1-B = 135.0(2)°) while atom O3 binds 4 Sr and 1 B. Two Sr, 1 Sc, and 1 B reside at the vertices of a distorted 4-coordinate tetrahedral site about atom O2 (B-O2-Sc2 = 114.5(2)°). Each of these coordination numbers is greater than the 3-coordination of the O atom in the calcite derivative $ScBO_3$ which contributes to the high density of the title compound and its thermodynamic stability with respect to a physical mixture of the phases $Sr_3(BO_3)_2$ and $ScBO_3$. The formula volume for the compound $Sr_3Sc(BO_3)_3$, 195.2 $Å^3$, is smaller than that computed for the mixture $Sr_3(BO_3)_2$ + $ScBO_3$, 198.1 $Å^3$, indicating a greater lattice energy and stability for $Sr_3Sc(BO_3)_3$ in its temperature range of

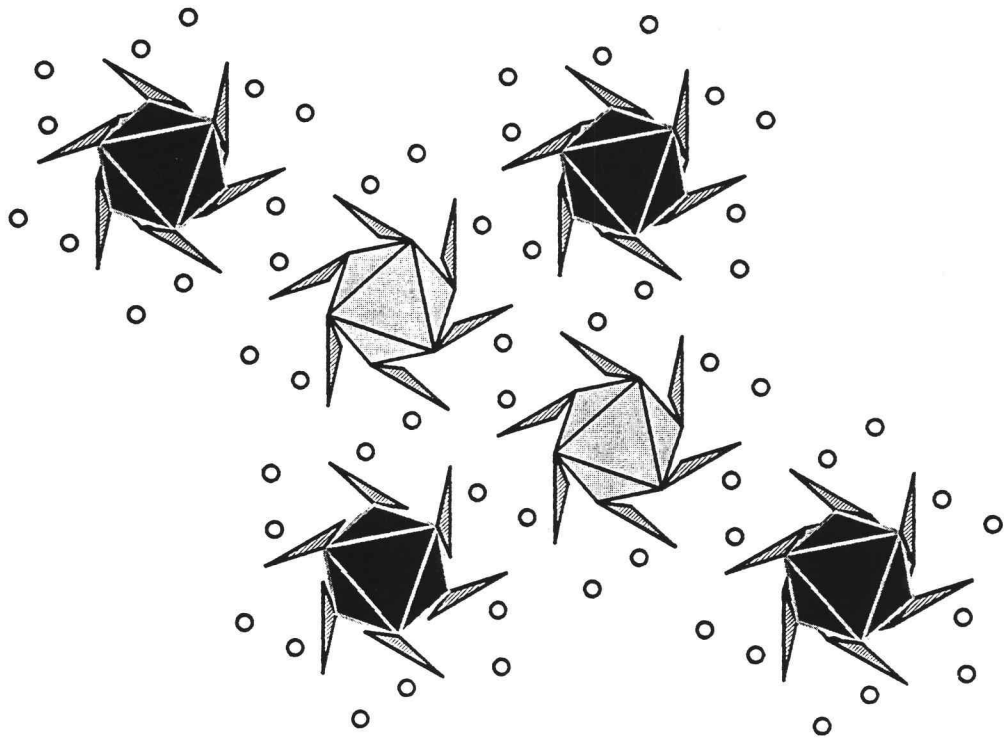

Figure 3.4. A drawing of the unit cell looking along the **c** axis. The Sc1-O octahedra are darkened and the Sc2-O octahedra are lightened in this figure. The relationship between the BO_3 triangular planar groups and the Sc-centered octahedra is apparent in this drawing. Sr atoms are the small open circles.

existence even though the Sr atom is 9-coordinate and the Sc atom is 6-coordinate in each compound.

We conclude by noting that the results indicate the structure to be highly ordered. In particular, there is no evidence for any significant disorder between the Sr and Sc sites.

Acknowledgments

This work was performed with funds provided through Lawrence Livermore National Laboratory (contract no. 2143103). DAK thanks the Alfred P. Sloan Foundation for a fellowship, 1989 - 91.

References

[1] K.I. Schaffers, T. Alekel III, P.D. Thompson, J.R. Cox, and D.A. Keszler, J. Am. Chem. Soc. **112**, 7068 (1990).

[2] P.D. Thompson and D.A. Keszler, Chem. Mater. **1**, 292 (1989).

[3] J. Huang and D.A. Keszler, to be submitted.

[4] K.I. Schaffers, P.D. Thompson, T. Alekel III, J.R. Cox, and D.A. Keszler, to be submitted.

[5] TEXSAN: Single Crystal Structure Analysis Software, Version 5.0. Molecular Structure Corporation, The Woodlands, TX 77381 (1989).

[6] D.A. Keszler and H. Sun, Acta Crystallogr. C **49**, 1505 (1988).

[7] R.D. Shannon, Acta Crystallogr. A **32**, 751 (1976).

CHAPTER 4

OPTICAL CHARACTERISTICS OF $Cr^{3+}:Sr_3Sc(BO_3)_3$ AND $Cr^{3+},Nd^{3+}:Sr_3Sc(BO_3)_3$

Paul D. Thompson and Douglas A. Keszler*

Department of Chemistry and

Center for Advanced Materials Research

Oregon State University

Corvallis, Oregon, 97331-4003 USA

Abstract

Room temperature and 77 K emission spectra for the new material $Sr_3Sc(BO_3)_3$ doped with Cr^{3+} are presented. The wavelength of maximum room-temperature emission intensity (λ_{max}) is 745 nm, blue-shifted by 55 nm from λ_{max} of the reference material $Cr^{3+}:ScBO_3$. Characteristics of the R-lines and associated phonon spectrum at low temperature are discussed. Spectra of samples with high Cr^{3+} dopant concentrations exhibit broad inhomogeneous peaks at 77 K with little emission quenching. Spectra also indicate that $Cr^{3+} \rightarrow Nd^{3+}$ energy transfer occurs at room temperature in both $Sr_3Sc(BO_3)_3$ and the reference material.

Introduction

In this chapter I describe the two spectrometers used to acquire optical spectra, the room temperature emission characteristics of the new material $Sr_3Sc(BO_3)_3$ doped with Cr^{3+}, and their comparison to the known laser host $Cr^{3+}:ScBO_3$.

The room temperature spectrum of $Sr_3Sc(BO_3)_3$ is compared to the 77 K spectrum and three important characteristics of the low temperature spectrum are discussed. These are the following: the reason $^2E \rightarrow {}^4A$ emission is split into two R-lines, the blue-shift of the R-lines at lower temperature, and the phonon emission spectrum associated with the R-line emission. Then inhomogeneous broadening at 77 K and inter-ion energy transfer at room temperature are discussed. Finally the room temperature spectrum of the Cr^{3+}-doped derivative $Sr_6ScAl(BO_3)_6$ is compared to the room temperature emission spectrum of $Cr^{3+}:Sr_3Sc(BO_3)_3$.

Experimental

Emission spectra were obtained in the ECE Optics Lab by using the 514.5 nm line from a Spectra-Physics Ar^+ ion laser operated at 12 mW output power. The beam was focused onto powdered samples mounted on 0.25" squares of aluminum. Fluorescence was passed through a yellow filter to eliminate any scattered green light from the laser and collected at 90° to the excitation beam by a 0.5 m Jarrell-Ash monochromator containing a holographic grating. Monochromated light was detected by an RCA 7102 (type S-1) photomultiplier tube cooled to 80-90 K by N_2 vaporized from the liquid state. The signal from the PMT was collected with a lock-in amplifier with reference to a mechanical chopper running at 670 Hz in the excitation beam path; output data were acquired and stored with a PC.

Room temperature and 77 K emission spectra, and 77 K excitation spectra were obtained with the Keszler group spectrometer using excitation light from an Oriel 300 W Xe lamp dispersed by a 0.4 m Cary prism monochromator. The exciting beam was focused onto powdered or crystalline samples mounted either on a pedestal or in an empty dewar for room temperature spectra. The dewar was filled with liquid nitrogen for 77 K data acquisition. Powder samples were mounted onto black squares of metal using non-fluorescent vacuum grease. Bubbles passing the sample

squares from boiling of the $N_2(l)$ caused some noise which was reduced by setting a longer time constant for data acquisition. Emitted light was scanned at 90° to the source beam by an Oriel 22500 0.125 m grating monochromator and detected by a Hamamatsu R636 photomultiplier tube. The signal was amplified by a Keithley model 602 picoammeter and transformed into a voltage signal suitable for processing by a PC. The spectral resolution of this instrument is 1 nm or better, depending on slit width.

Results

In Chapter 1, I stated the thesis that the presence of Sr in a scandium borate matrix would act to shift the Cr^{3+} emission band to higher energies. Spectra I obtained in the ECE Optics Lab and presented in Figure 4.1 verify this thesis. The room temperature emission spectra for Cr^{3+}-doped $Sr_3Sc(BO_3)_3$ and $ScBO_3$ as reference are plotted together using the same wavelength scale on the abscissa. The spectra show that λ_{max} for the $^4T \rightarrow {}^4A$ broad band of $Sr_3Sc(BO_3)_3$ at 745 nm is blue-shifted 55 nm from the broad band maximum of $ScBO_3$ occurring at 800 nm. The spectral changes on going from Cr^{3+}:$ScBO_3$ to Cr^{3+}:$Sr_3Sc(BO_3)_3$ are similar to the changes evident in the Ga-garnet sequence shown in Figure 1.7 of Chapter 1. Inclusion of the larger, electropositive Sr has increased the crystal field strength at the Cr^{3+} site with two results: blue-shift of the broad band and emergence of the $^2E \rightarrow {}^4A$ sharp lines in the spectrum. These two changes both occur in the garnet sequence and are ascribed to shortening of the Cr-O bond producing a higher crystal field strength at the Cr^{3+} site [1,2].

Room temperature and 77 K spectra for $Sr_3Sc(BO_3)_3$ (2% Cr^{3+}) are displayed together in Figure 4.2. The room temperature spectrum shown in this figure was taken on the Keszler group spectrometer and is essentially identical to

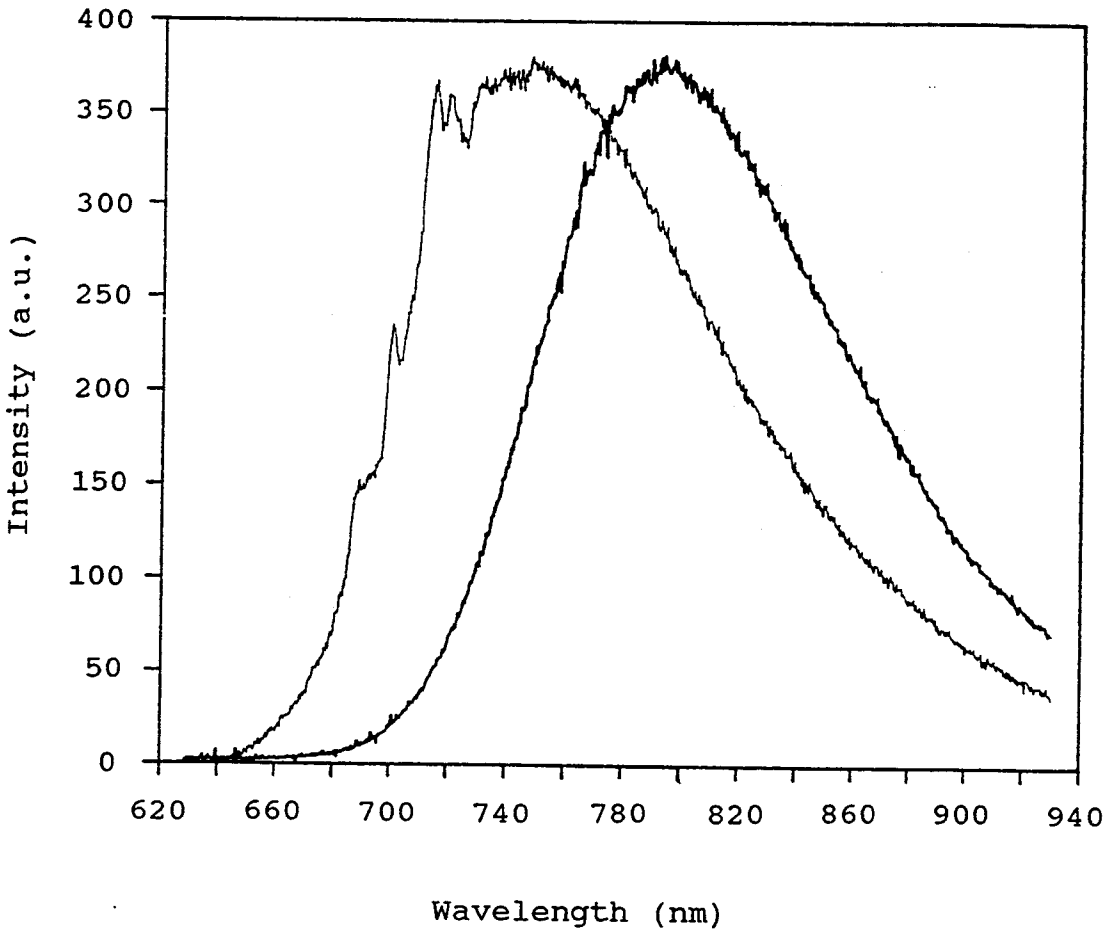

Figure 4.1. Room temperature fluorescence of $Cr^{3+}:Sr_3Sc(BO_3)_3$ (broad band plus sharp peaks) and $Cr^{3+}:ScBO_3$ (broad band only). Emission intensity for the former material was multiplied by 7.5.

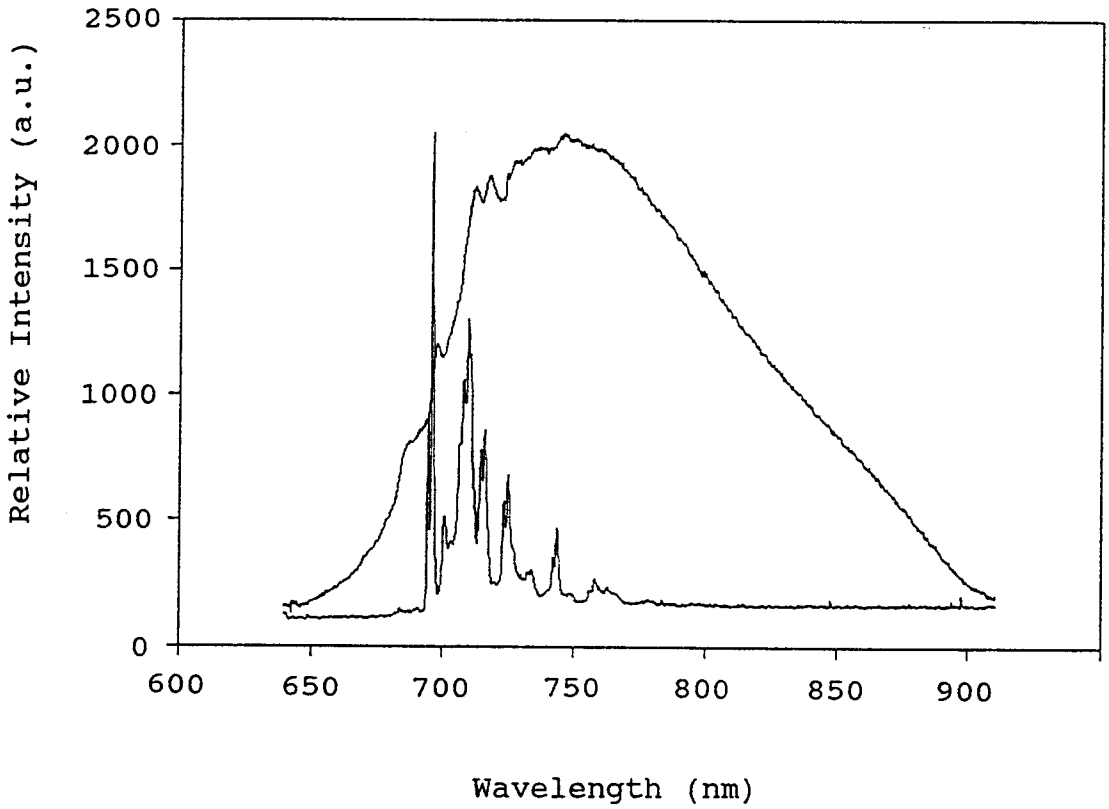

Figure 4.2. Room temperature and 77 K emission spectra of $Cr^{3+}:Sr_3Sc(BO_3)_3$. Low temperature spectrum exhibits disappearance of broad band. Room temperature intensity was multiplied by 40.

the room temperature spectrum for $Sr_3Sc(BO_3)_3$ in Figure 4.1 obtained by using the Ar^+ ion laser-excited spectrometer in the ECE Optics Lab. Acquisition of essentially identical spectra from two different spectrometers and two different samples gives me confidence that I have accurately measured the actual emission characteristics of the material.

The room temperature spectrum of $Cr^{3+}:Sr_3Sc(BO_3)_3$ is composed of two prominent features: the $^4T \rightarrow {}^4A$ broad band and sharp peaks resulting from the $^2E \rightarrow {}^4A$ transition. Both features are present in the fluorescence spectra of numerous Cr^{3+} containing materials such as emerald [3], alexandrite [4] (Figure 1.8), garnets such as YGG (Figure 1.5) and $Cr^{3+}:ß\text{-}Ga_2O_3$ [5].

The combined plot of room temperature and 77 K spectra in Figure 4.2 provide evidence that the ^2E state is lower in energy than the ^4T state and that the ^4T state is populated by a Boltzmann distribution of excited electrons just as for the $Cr^{3+}:YAl_3(BO_3)_4$ material that was discussed in Chapter 1 (Figure 1.6) [6]. $Cr^{3+}:Sr_3Sc(BO_3)_3$ shows the same disappearance of the broad band as the temperature is lowered.

Low temperature spectra were taken in $N_2(l)$ to reduce or eliminate thermal population of the ^4T state which is a few kT above the ^2E state. This attempt succeeded in removing the broad band from the spectrum revealing R-

lines at 694.0 nm and 695.4 nm, and a complex frequency modulated vibronic side-band on the low-energy side of the R-lines. The R-line at lower energy (694.5 nm) is the primary $^2E \rightarrow {}^4A$ line designated "R1" and the higher energy, lower intensity line is designated "R2" in all succeeding discussion and figures.

R-Line Origins

Two R-lines appear in the spectrum instead of one because the ^2E state is split into two Kramers doublets ($^2E \rightarrow \bar{E} + 2\bar{A}$) [7] in which the $\bar{A}$-levels are at a higher energy than the $\bar{E}$-levels. An imposed magnetic field can split the doublets even further into four R-lines but the levels remain degenerate in the absence of a magnetic field. The half-integral sum of orbital and spin multiplicities for the ^2E term ($J = 5/2$) requires a double group to reduce the term [8]. The bars over the resultant irreducible representations ($\bar{E} + \bar{A} + \bar{A}$) indicate their origin from a double group. Splitting of the ^2E state is caused by the low symmetry trigonal component of the crystal field at the Sc^{3+} (Cr^{3+}) site and spin-orbit coupling in the excited d-electron [5,7,9]. Distortions of the octahedron along the $\bar{3}$ axis have reduced the site symmetry from O_h to S_6 ($\bar{3}$). The higher energy R2 transition ($2\bar{A} \rightarrow {}^4A$) has less intensity than the R1

transition ($\bar{E} \rightarrow {}^4A$) because the upper $2\bar{A}$ levels are thermally occupied by excited electrons in a Boltzmann distribution. Fewer electrons populate the upper energy levels of the split ^2E state.

Existence of two sharp R-lines is evidence that all luminescence is from Cr^{3+} on only one of the two Sc^{3+} sites. If a significant proportion of the Cr^{3+} dopant ion occupied both sites two sets of R-lines would be observed. (This is assuming instrument resolution is high enough to separate the resultant 4 peaks.) Lifetime measurements of both R-lines will be obtained when a laser spectrometer is set up in the Chemistry Department this summer. These measurements are expected to give the same value and establish that only one site is occupied by the Cr^{3+} ion. Both R-lines having an identical lifetime would be proof that they involve electronic transitions on the same site and exist because of the two ^2E levels. Presence of two R-lines shows that the material is similar to $Cr^{3+}:YAl_3(BO_3)_4$ [10], ß-Ga_2O_3 [5,10], and ruby [10,11] in which the $^2E \rightarrow \bar{E} + 2\bar{A}$ split produces the two R-lines. All of these materials have trigonally-distorted octahedral Cr^{3+} sites as in $Sr_3Sc(BO_3)_3$ (see Table 4.1).

The higher energy line (at 694.0 nm) could not be from a $^2T \rightarrow {}^4A$ transition because the ^2T state is much higher than 29 cm^{-1} above the ^2E state. This is evident in the Tanabe-Sugano diagram included in Figure 1.1. The

Table 4.1. Site symmetry and R-line Splitting in Spectra of Cr^{3+}-containing Materials.

Compound	Site	cm^{-1}	Reference
YGG	S_6 ($\bar{3}$)	24.0	20
Ruby	C_3 (3)	29.0	10, 22
$Sr_3Sc(BO_3)_3$	S_6 ($\bar{3}$)	29.8	This work
α-Ga_2O_3	C_3 (3)	32.5	18, 22
YSGG	S_6 ($\bar{3}$)	34.0	20
GGG	S_6 ($\bar{3}$)	35.0	20
Alexandrite	C_{3v} (3m)	41.2	4[a]
$YAl_3(BO_3)_4$	C_2 (2)	51.0	This work, 21
Emerald	D_3 (32)	57.6	This work
ß-Ga_2O_3	C_s (m)	146.0	5, 22

[a]Computed from peaks in Figure 4 of reference [4].

$^2T \rightarrow {}^4A$ sharp line transition is located at higher energies than the R-lines in the emission spectra of such materials as alexandrite [12] and GSGG [13].

Extent of R-line splitting is related to the symmetry of the dopant site. When comparing compounds with similar composition and structure, the greater the trigonal distortion the more the R-lines are split. This is evident for the two materials α- and ß-Ga_2O_3 listed in Table 4.1. The latter oxide has lower site symmetry than the former and a larger R-line split.

Low Temperature R-Line Blue-shift

A phenomenon observed in many Cr^{3+}-containing solid-state materials that exhibit $^2E \rightarrow {}^4A$ emission is a gradual shift of the R-lines to higher energy as the temperature is lowered. Researchers observe this shift in materials such as ruby [14,15,16], ß-alumina:Cr^{3+} [9], MgO:Cr^{3+} [17] and MgO:V^{2+} [17]. Experimental plots of lineshift ($\Delta\omega$ in cm^{-1}) versus temperature (T in K) reveal a smoothly increasing function as temperature increases. A schematic representation of graphs depicting real behavior is included in Figure 4.3. The slope of the function decreases at higher temperatures indicating larger lineshifts. The lines shift to the red from their position at absolute zero as temperature is raised. The

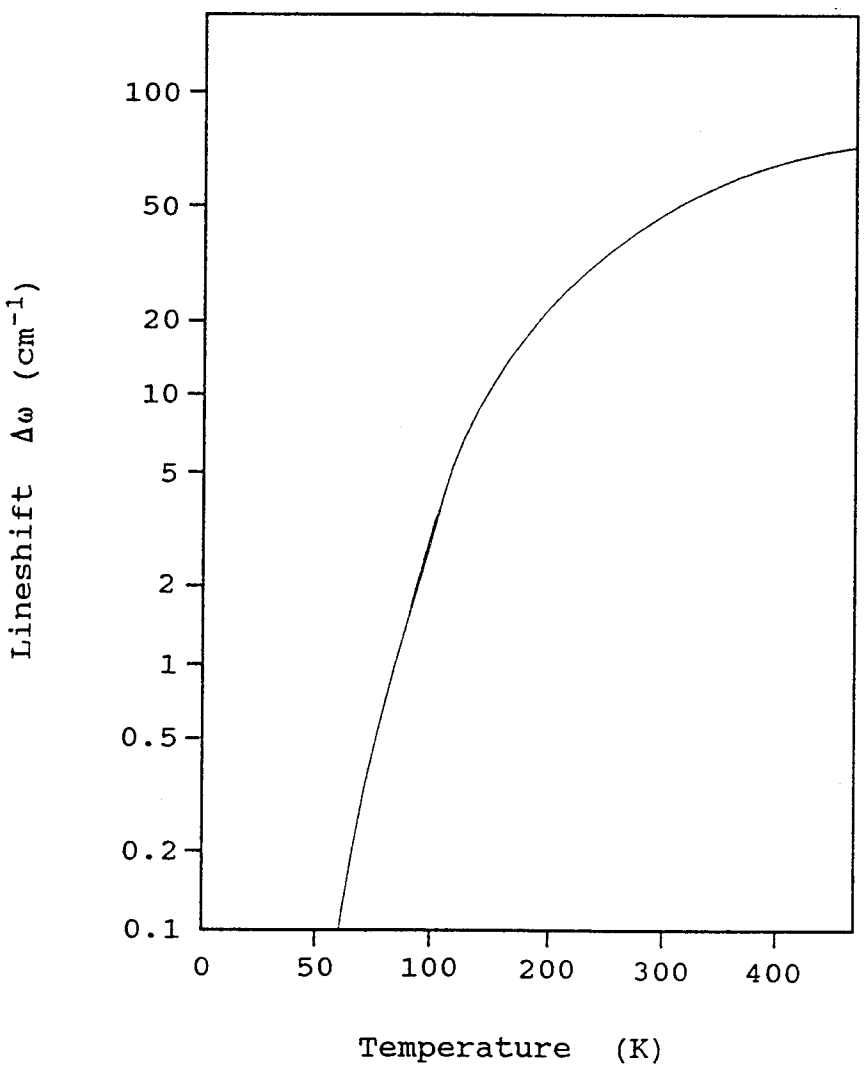

Figure 4.3. Schematic representation of frequency shift ($\Delta\omega$) v.s. T (K) observed in the emission spectra of many solid-state materials.

shift is caused by two factors that gradually decrease the crystal field strength imposed on the d-electrons as temperature goes up. The most important factor causing the shift is zero-point motion of the emitting ion about its equilibrium position. This motion is affected by Raman scattering of phonons by the emitting ion in the host lattice [14,15]. The amplitude of zero-point vibration is a smoothly increasing continuous function of temperature.

The other factor is composed of direct processes, mainly the expansion of the lattice that is also a smoothly increasing function as temperature increases. The net result of both factors is to decrease the energy difference between the excited and ground states for the transition as temperature is raised.

Comparison of the R-line positions in the room temperature and 77 K spectra in Figure 4.2 show that these peaks are blue-shifted at 77 K from their room temperature position where they occur as a small peak on the high energy side of the broad band at about 697 nm. Because lineshift is caused primarily by the effect of Raman-scattered phonons on the zero-point motion of the impurity ion, it is dependent on the density of phonon states in the crystal. McCumber and Sturge modeled this relationship as:

$$\Delta\omega = \alpha/2\pi \int_0^\infty \rho(\omega)\, n(\omega)\, d\omega$$

where $\rho(\omega)$ = effective density of phonon states, $n(\omega) = [\exp(\omega\hbar/kT)-1]^{-1}$, the Bose-Einstein distribution coefficient, and α is a constant [14]. McCumber and Sturge assumed a Debye spectrum of acoustic phonons to evaluate $\rho(\omega)$ resulting in the following expression for the lineshift:

$$\Delta\omega = k\int_0^{\omega D}\omega^3[\exp(\omega\hbar/kT)-1]^{-1}d\omega$$

where k is a constant. For materials obeying this equation, a larger frequency shift would be expected for R-lines occurring at higher frequencies. The size of the frequency shift would also increase as the temperature increases.

The frequency shift to lower energy at higher temperature is the result of the termination of $^2E \rightarrow {}^4A$ photon emission on a near-continuum of phonon states in the lattice and is a continuous, smooth function. Because of this behavior, the lineshift is not a discontinuous quantum jump caused by phonon emission that occurs at a particular temperature. Consequently, the blue-shift of the R-lines in $Sr_3Sc(BO_3)_3:Cr^{3+}$ can be represented simply by pushing the $\upsilon = 0$ ground state vibrational level deeper toward the bottom of the ground state potential well as temperature is lowered to 77 K.

Low Temperature Phonon Spectrum

Because at low temperatures phonons can only be emitted, peaks in the spectrum caused by combined photon and phonon emission occur to the red of the sharp R-lines [17]. The many sharp peaks at lower energies than the R-lines in the emission spectrum shown in Figure 4.4 are a result of the complex phonon spectrum of $Sr_3Sc(BO_3)_3:Cr^{3+}$. By analyzing the pattern of relative intensities and energy spacings between sets of peaks it is possible to pick one single-phonon progression out of all the peaks. Since a phonon is emitted each time an electronic transition terminates on an excited vibrational level of the ground state, there are peaks in the single-phonon spectrum coupled to emission of photons from both the $\bar{E}$ and $2\bar{A}$ levels of the split ^2E excited state. Hence, paired peaks resulting from photon emission coupled to emission of a phonon of particular energy are separated by the same energy that separates the two R-lines. This separation is 30(6) cm^{-1} in $Sr_3Sc(BO_3)_3$.

I have noted the relative intensity differences and measured the energy differences between peaks in the vibronic sideband and found four sets of peaks with relative intensities similar to the relative intensities of the two R-lines and with energy separations comparable to the energy separation of the R-lines. I have marked

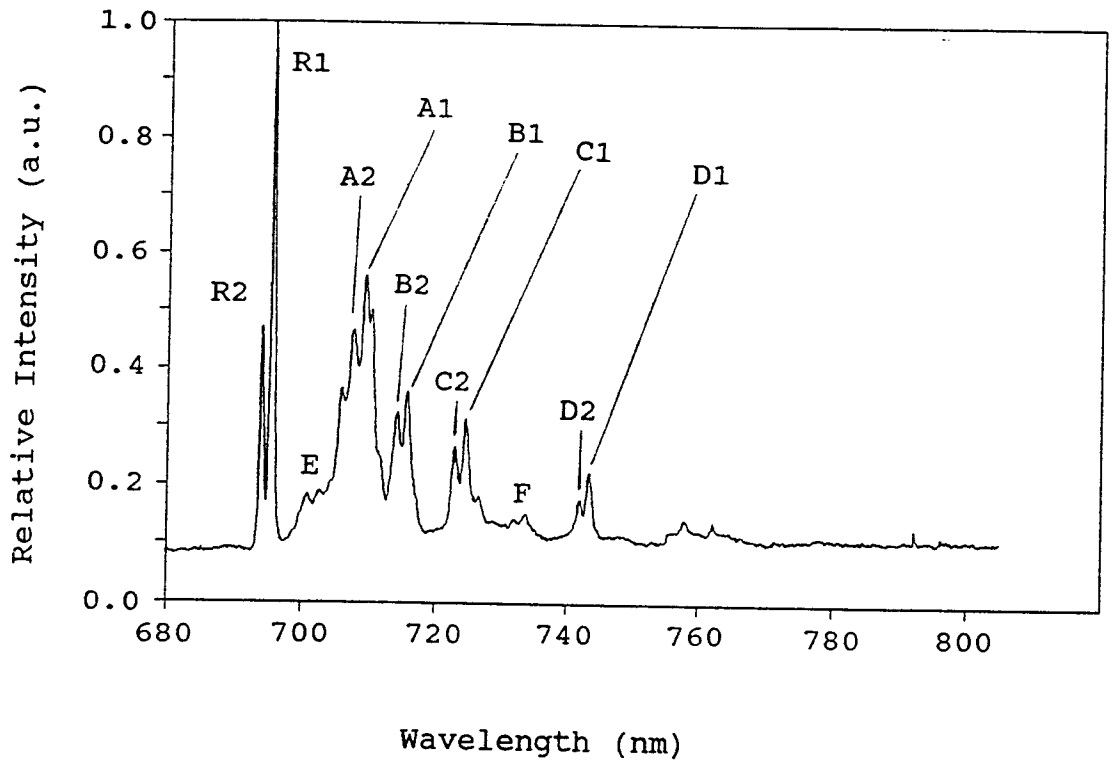

Figure 4.4. Low temperature (77 K) emission spectrum of $Cr^{3+}:Sr_3Sc(BO_3)_3$. Zero-phonon lines are labeled R1 and R2. Phonon-assisted lines are labeled A1 through D1 for the lines associated with R1 and A2 through D2 for the lines associated with R2.

these four sets A through D on the low temperature spectrum in Figure 4.4 and numbered them 1 or 2 to indicate which peaks go with R1 and R2 respectively. A configurational coordinate diagram given in Figure 4.5 shows the upper ^2E potential energy well unshifted from the ground state well and shows the levels resulting from the ^2E split and the ground state vibrational levels. Ten arrows represent the two R-line and the eight phonon-assisted transitions observed in the $Sr_3Sc(BO_3)_3$ spectrum. Peak positions and energies for each of the ten transitions are listed in Table 4.2 along with the energy difference between the peaks in each pair. The average energy difference between sets A through D is 30(6) cm^{-1}, and compares well with the 30(6) cm^{-1} energy difference between the two R-lines. Table 4.3 gives the energy differences between the phonon-assisted peak and the R-line from the same ^2E level it originates from. I averaged each pair of values to obtain an estimate of the size of the phonons emitted in each case: 278(6), 407(6), 578(6), and 931(6) cm^{-1} respectively.

I confirmed these peak assignments by examining the room temperature infrared absorption spectrum of $Sr_3Sc(BO_3)_3$ which contains peaks caused by absorption of light into normal vibrational modes of the compound. Three of the phonons identified in the 77 K emission spectrum occur in the IR spectrum, at 407, 578, and 931

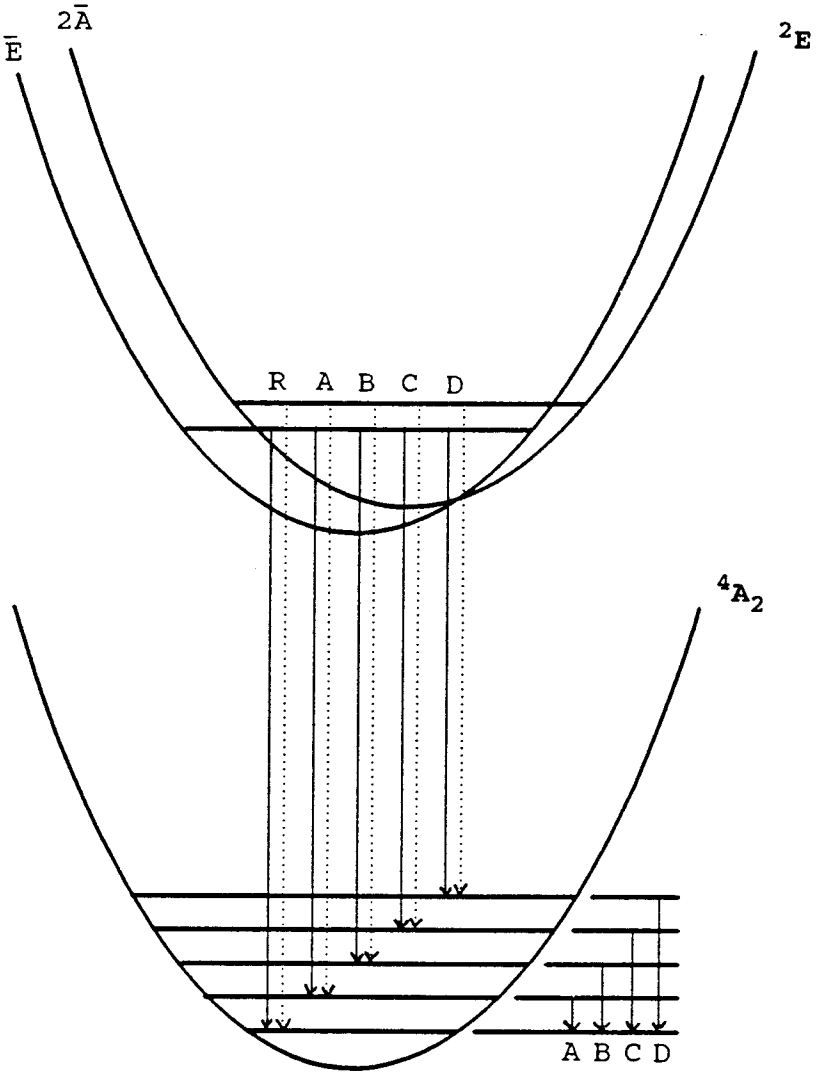

Figure 4.5. Configurational coordinate diagram showing the ten $^2E \rightarrow {}^4A$ transitions that were identified in Figure 4.4. Transitions that originate from the $\bar{E}$ level are labeled "1" and those that originate from the $2\bar{A}$ level are labeled "2" in Figure 4.4. To the right of the ^4A energy well the phonons are labeled A through D.

Table 4.2. Positions (λ) and energies (E) of zero-phonon (R-line) and phonon-assisted peaks in the 77 K spectrum of $Sr_3Sc(BO_3)_3$. The energy difference (ΔE) between peaks 1 and 2 of each set is listed in the fourth column.

Peak	λ (nm)	E (cm^{-1})	ΔE (cm^{-1})
Zero-phonon peaks:			
R2	694.0(2)	14410(4)	
R1	695.4(2)	14380(4)	30(6)
Phonon-assisted Peaks:			
A2	707.5(2)	14134(4)	
A1	709.2(2)	14101(4)	33(6)
B2	714.2(2)	14002(4)	
B1	715.6(2)	13974(4)	28(6)
C2	722.9(2)	13833(4)	
C1	724.6(2)	13801(4)	32(6)
D2	742.0(2)	13478(4)	
D1	743.4(2)	13451(4)	27(6)
			$\bar{x}$ = 30(6)

Table 4.3. Energy difference (ΔE) between each R-line and each phonon-assisted peak associated with it. The average value gives an estimate of phonon size in the second column.

	ΔE (cm^{-1})	E (cm^{-1})
R2-A2	276(6)	
R1-A1	279(6)	278(6)
R2-B2	408(6)	
R1-B1	406(6)	407(6)
R2-C2	577(6)	
R1-C1	579(6)	578(6)
R2-D2	932(6)	
R1-D1	929(6)	931(6)

cm^{-1} respectively. These peaks are indicated in the infrared spectrum shown in Figure 4.6. The 407 and 578 cm^{-1} peaks probably correspond to Sc-O stretching or bending modes [8], and the 931 cm^{-1} peak is the symmetric breathing mode of the BO_3 group. This mode that is absent in $ScBO_3$ is allowed in this compound because the symmetry of the group has been lowered from D_3 in $ScBO_3$ to C_1 in $Sr_3Sc(BO_3)_3$. The BO_3 group in the latter compound is a distorted triangular plane of O atoms with the B atom slightly displaced from the three O atoms of the plane. The 278 cm^{-1} phonon is too low in energy to appear in the IR spectrum which has been cut off at 400 cm^{-1} to eliminate KBr absorption peaks.

I computed the energies separating the E and F sets of peaks which differ by 38(6) and 35(6) wavenumbers respectively. These may also be phonons associated with photon emission but have slightly higher energy separations than the R-line peaks. These peaks along with the other peaks in Figure 4.4 probably result from multi-phonon processes associated with the $^2E \rightarrow {}^4A$ transition. I detect no relation of these peaks to the R-line peaks as obvious as the A - D progressions so assignment of these other peaks will not be attempted in this work.

Other prominent peaks in the IR spectrum at 630, 760, and 1250 cm^{-1} are of vibrational modes in the $Sr_3Sc(BO_3)_3$ crystal that do not have the correct symmetries to cause

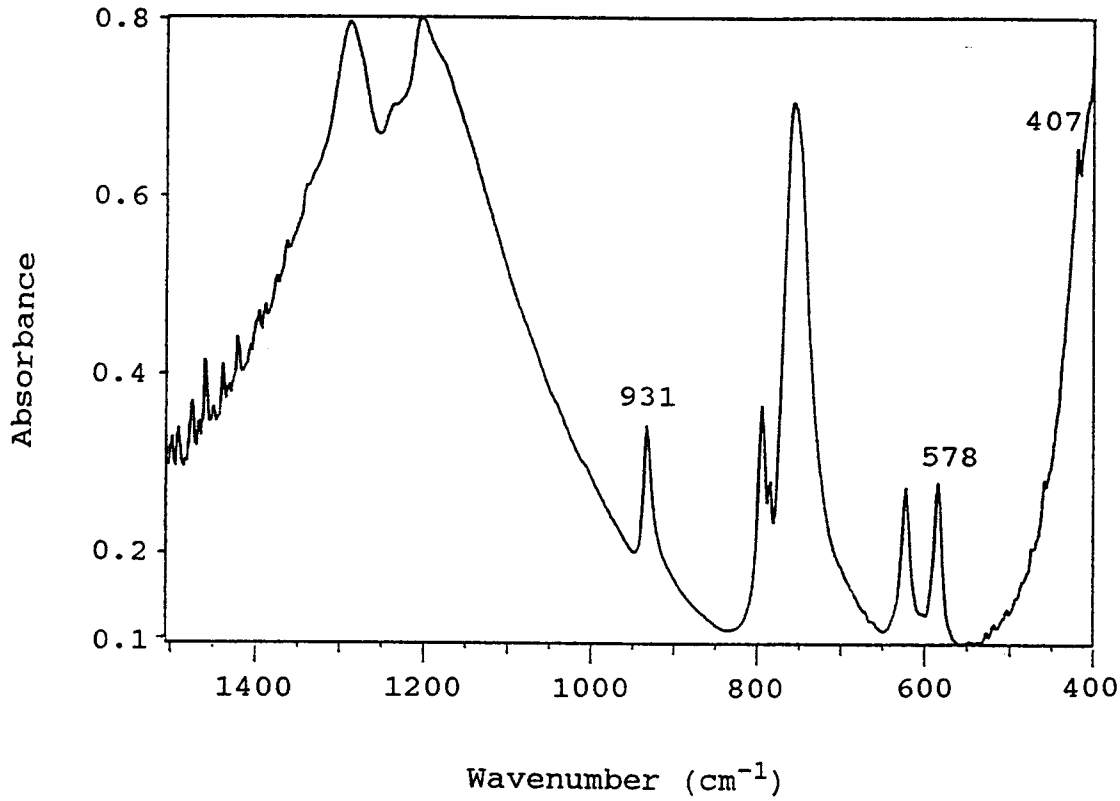

Figure 4.6. Room temperature infrared spectrum of $Cr^{3+}:Sr_3Sc(BO_3)_3$. Three of the phonons identified in the 77 K emission spectrum are labeled in the IR spectrum.

phonon-assisted electronic transitions in the compound. This is the reason phonons with energies comparable to these peaks do not show up in the phonon emission spectrum of the material.

Inhomogeneous Peak Broadening

Low temperature (77 K) spectra of $Sr_3Sc(BO_3)_3$ doped with 2% and 5% Cr^{3+} respectively are shown in Figure 4.7. The material exhibits inhomogeneous broadening because of the increase in number of Sc^{3+} sites occupied at the higher concentration. The 5% Cr^{3+} spectrum exhibits R-line and vibronic progression peaks that have overlapped with neighbor peaks forming much broader peaks and consequent loss of detail.

Excitation spectra obtained for a series of Cr^{3+}-doped samples ($Sr_6Sc_{2-x}Cr_x(BO_3)_6$ with x = 0.04 to 0.6) exhibited no shift in λ_{max} for the $^4A \rightarrow {}^4T_2$ and $^4A \rightarrow {}^4T_1$ absorptions indicating that up to 30% occupation of the Sc^{3+} site by Cr^{3+} does not affect the crystal field strength enough to change ^4T energies relative to the ground state.

Energy Transfer in $Sr_3Sc(BO_3)_3$

An emission spectrum (Figure 4.8) of $Sr_3Sc(BO_3)_3$

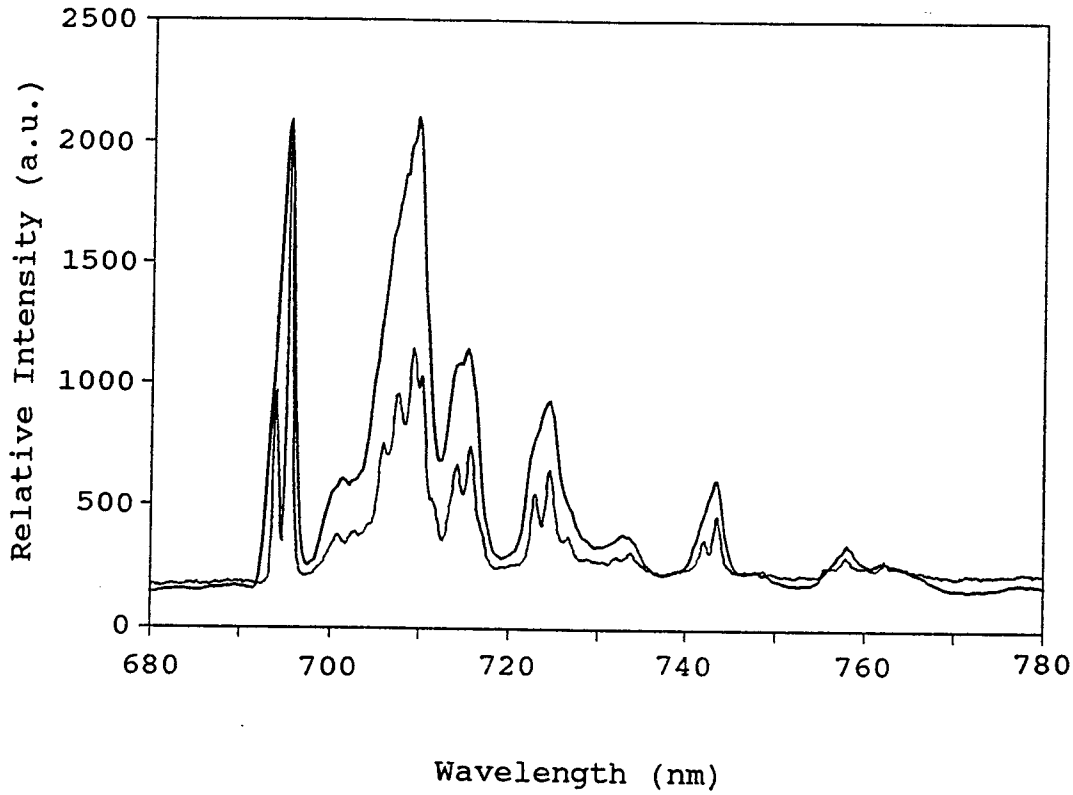

Figure 4.7. Low temperature emission spectra of $Sr_3Sc(BO_3)_3$ doped with 2% Cr^{3+} on the Sc^{3+} site (sharp peaks) and with 5% Cr^{3+} on the Sc^{3+} site (broad peaks).

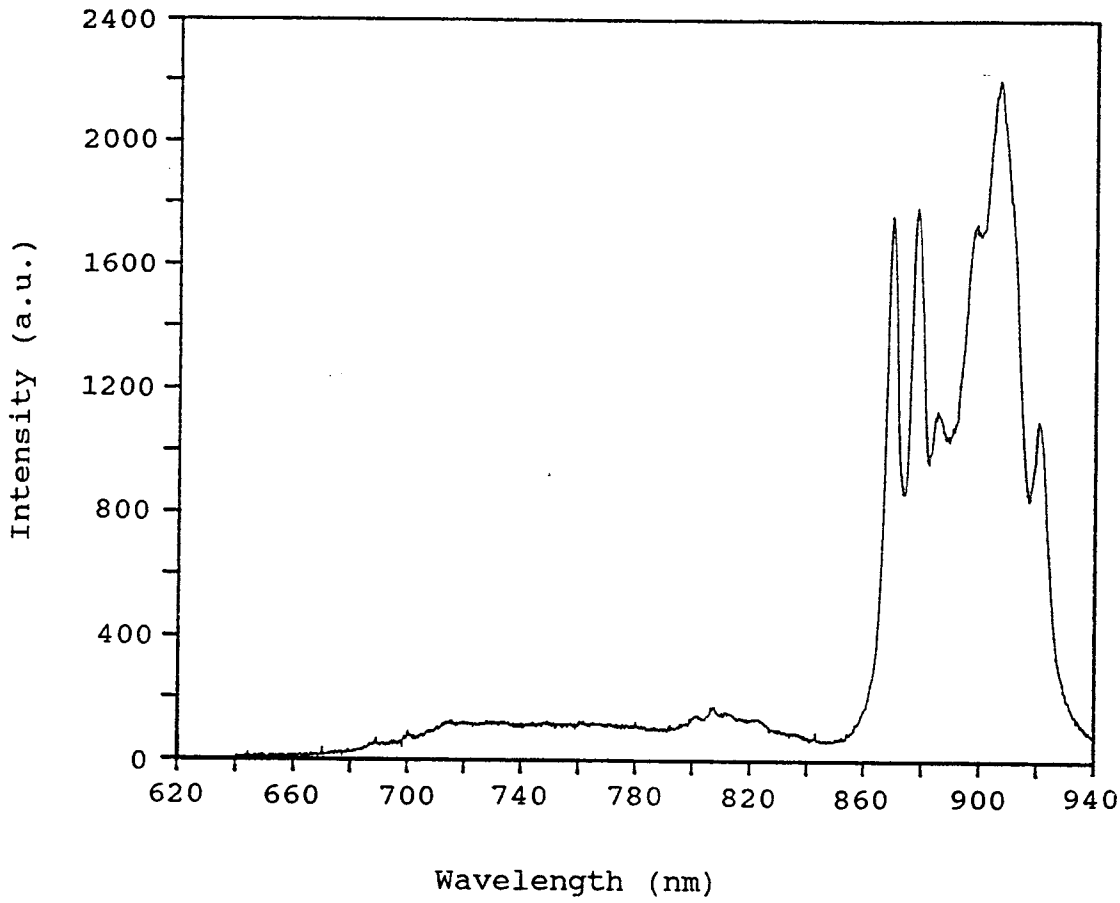

Figure 4.8. Room temperature emission spectrum of $Sr_3Sc(BO_3)_3$ codoped with Cr^{3+} and Nd^{3+}.

codoped with the transition metal ion Cr^{3+} and the rare-earth ion Nd^{3+} provides evidence that energy is transferred from the Cr^{3+} ion to the Nd^{3+} ion following selective excitation of Cr^{3+}. This spectrum exhibits almost complete disappearance of the Cr^{3+} emission peak (Figure 4.1) between 680 nm and 800 nm and presence only of the $^4F_{3/2} \rightarrow {}^4I_{9/2}$ emission multiplet of the Nd^{3+} ion. A schematic representation is presented in Figure 4.9 showing that the ^2E storage level of the Cr^{3+} ion is higher than the ^4F emission states of Nd^{3+}. The spectrum in Figure 4.8 reveals that pathways (either radiative or nonradiative) exist for energy transfer from the ^2E (Cr^{3+}) to ^4F (Nd^{3+}) states in the host lattice. $Cr^{3+} \rightarrow Nd^{3+}$ energy transfer has been observed in other compounds such as $YAlO_3$ [19].

Existence of energy transfer is also observed in the codoped reference compound $ScBO_3$ (Figure 4.10). This spectrum exhibits the broad band of Cr^{3+} emission with intensity reduction in several narrow regions where photon emission from the donor Cr^{3+} has been pre-empted by energy transfer into Nd^{3+} excited state levels. This is a transfer-loss spectrum for Cr^{3+} in the $ScBO_3$ matrix accompanied by the $^4F_{3/2} \rightarrow {}^4I_{9/2}$ emission multiplet of Nd^{3+} and constitutes proof that inter-ion energy transfer occurs in the reference material as well, though not as completely as it occurs in the new material $Sr_3Sc(BO_3)_3$.

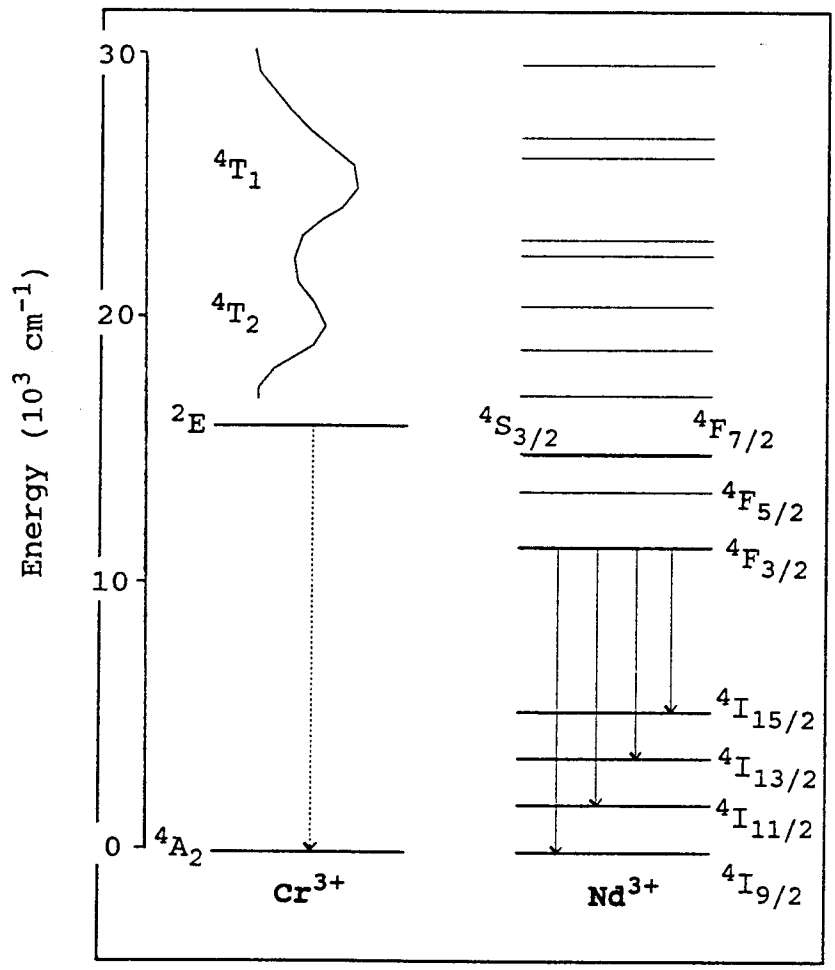

Figure 4.9. Diagram of the energy levels in Cr^{3+} and Nd^{3+} ions. The ^4T and ^2E levels of Cr^{3+} are higher in energy than the ^4S and three ^4F levels of Nd^{3+}. Four transitions from the lowest excited state to the four ground state levels in Nd^{3+} are shown.

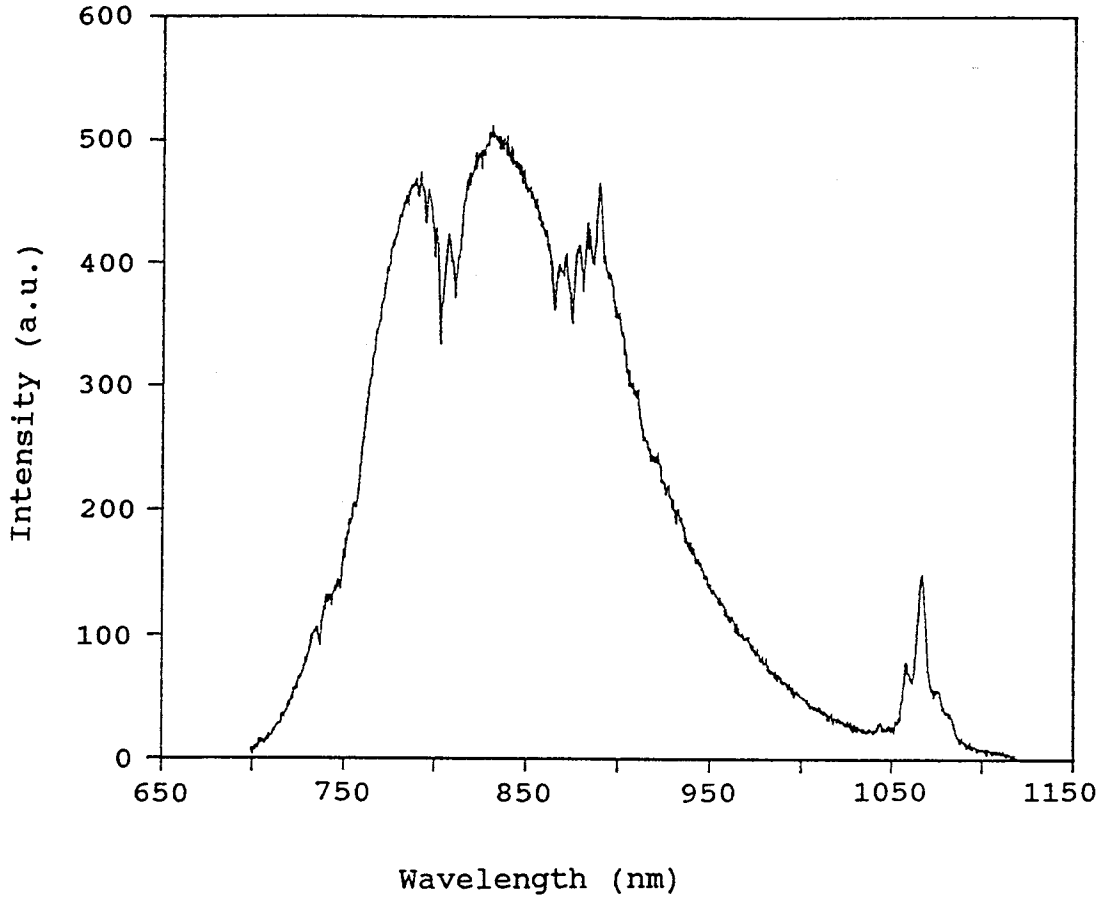

Figure 4.10. Room temperature emission spectrum of $ScBO_3$ co-doped with Cr^{3+} and Nd^{3+}. Energy transfer between the two ions has caused intensity losses in the Cr^{3+}:$ScBO_3$ broad band and presence of two Nd^{3+} emission multiplets.

$Cr^{3+}:Sr_6ScAl(BO_3)_6$ Characteristics

Comparison of emission characteristics to the related material $Sr_6ScAl(BO_3)_6$ confirms the site occupancy preference of the Cr^{3+} ion and the effects of crystal field strength on the $^4T \rightarrow {}^2E$ energy separation in this material. Figure 4.11 presents the room temperature emission spectrum for the analogue $Cr^{3+}:Sr_6ScAl(BO_3)_6$ in which the smaller M' site is almost exclusively occupied by the Al^{3+} ion. In this case substitution of the smaller, harder ion Al^{3+} for Sc^{3+} in the smaller site increases the crystal field strength at the Cr^{3+} site. The resultant increase in ΔE between the ^2E and ^4T states decreases thermal population of the upper state with subsequent loss of emission intensity by the broad band.

Even though the 77 K spectra are expected to be quite similar for the two materials, the room temperature spectrum of the Al-containing analogue shows a marked decrease in the intensity of the $^4T \rightarrow {}^4A$ broad band emission relative to the $Cr^{3+}:Sr_3Sc(BO_3)_3$ broad band shown in Figure 4.1. This is a direct result of the smaller Al^{3+} ion allowing the unit cell to contract producing a higher crystal field at the Cr^{3+} site. The shift to higher crystal field (Dq/B) has increased the separation between the ^2E and ^4T state which lies above the doublet state and is thermally fed from electron residence in the

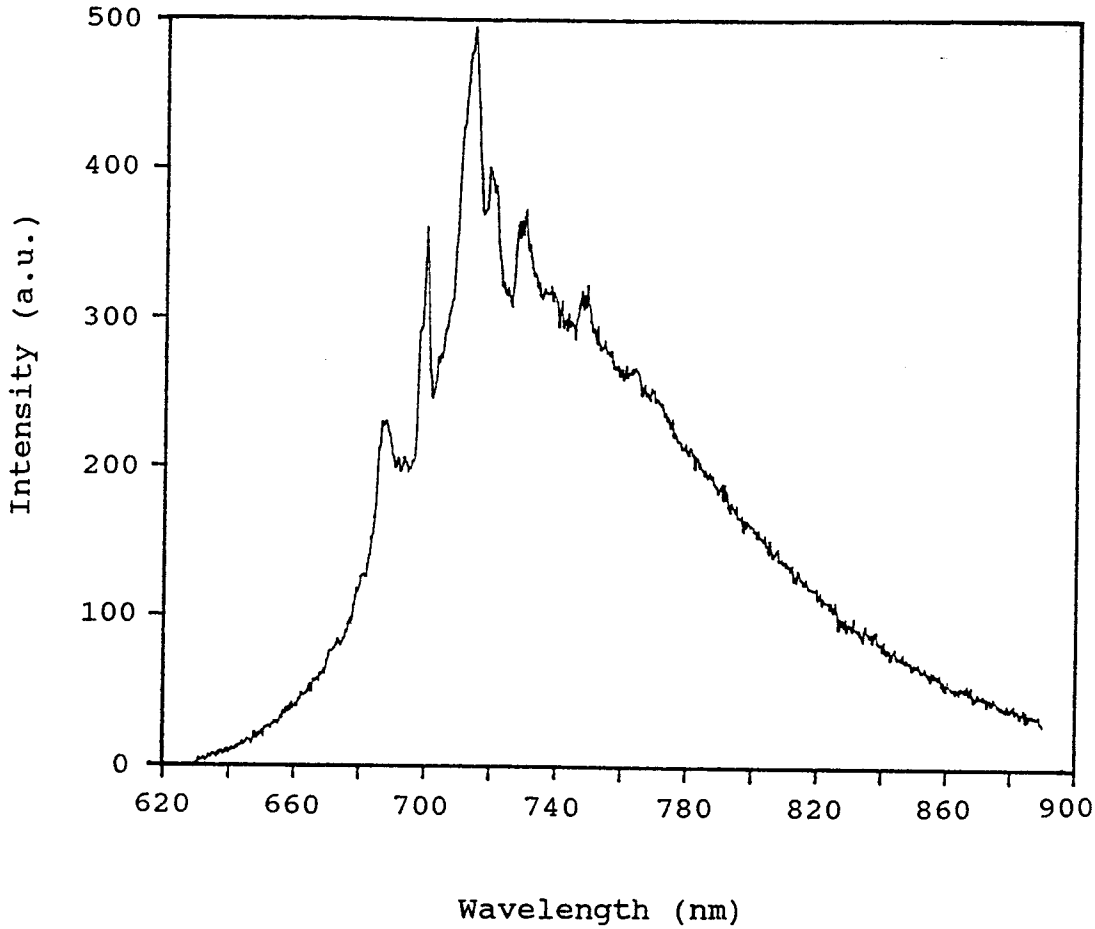

Figure 4.11. Room temperature emission spectrum of $Cr^{3+}:Sr_6ScAl(BO_3)_6$. In contrast to $Cr^{3+}:Sr_3Sc(BO_3)_3$, the $^4T \rightarrow {}^4A$ broad band has lost intensity relative to the $^2E \rightarrow {}^4A$ peaks in this material.

^2E state. This increase in ΔE between the two states leaves the ^4T state less populated by excited electrons and results in a decrease of the broad band transition intensity. As the broad band peak is reduced in size the sharp peaks resulting from the $^2E \rightarrow {}^4A$ transition which were buried in the broad band emerge.

Evidence that Al^{3+} does not occupy the larger Sc^{3+} site is found in the sequence of room temperature emission spectra taken for the series $Cr^{3+}:Sr_6Sc_{2-x}Al_x(BO_3)_6$ (x = 0 to 1.6). As Al^{3+} content varied from x = 0 to 1 the broad band gradually decreased in intensity. However, as soon as Al^{3+} content exceeded x = 1 the emission spectra did not change indicating x = 1 is the maximum amount of Al^{3+} incorporated into the structure. Synthesis experiments indicate that the proposed compound "$Sr_3Al(BO_3)_3$" does not form.

Conclusion

$Sr_3Sc(BO_3)_3:Cr^{3+}$ is potentially an efficient new laser material because it has an emission band that is blue-shifted away from λ_{max} of the $ScBO_3:Cr^{3+}$ emission band. The material melts congruently and can potentially be grown as large single crystals by the Czochralski method. The compound also exhibits energy transfer from Cr^{3+} to Nd^{3+}, allowing for the potential to develop an efficient codoped laser material.

Acknowledgments

Thomas A. Reynolds provided the spectra presented in Figures 4.2 and 4.3. These were taken on the Keszler group spectrometer built by Thomas and interfaced by Theodore Alekel III.

I obtained the other emission spectra either on the Keszler group spectrometer or on the Electrical and Computer Engineering Optics Lab spectrometer provided for my use by Dr. John R. Arthur.

References

[1] B. Struve and G. Huber, Appl. Phys. B, **36**, 195 (1985).

[2] A. Budgor, SPIE **vol 461**, New Lasers for Analytical and Industrial Chemistry, 62 (1984).

[3] S.T. Lai, SPIE **vol 622**, High Power and Solid State Lasers, 146 (1986).

[4] M.L. Shand and J.C. Walling, IEEE J. Quant. Elec. **QE-18**, No. 7, 1152 (1982).

[5] D. Vivien, B. Viana, A. Revcolevschi, J.D. Barrie, B. Dunn, P. Nelson and O.M. Stafsudd, J. Lumin. **39**, 29 (1987).

[6] F. Kellendonk, T. van den Belt and G. Blasse, J. Chem. Phys. **76(3)**, 1194 (1982).

[7] S. Sugano and Y. Tanabe, J. Phys. Soc. Jpn. **13(8)**, 880 (1958).

[8] T.A. Reynolds, private communication.

[9] G. Mariotto, M. Montagna and F. Rossi, J. de Phys. **46**, C7-343 (1985).

[10] This work.

[11] T.M. Dunn and A.H. Francis, Phys. Rev. Lett. **25(11)**, 705 (1970).

[12] J.C. Walling, Topics in Applied Physics, Tunable Lasers, eds: L.F. Mollenauer and J.C. White, Springer-Verlag, Berlin, **59**, 331 (1987).

[13] K.P. O'Donnell, A. Marshall, M. Yamaga and B. Henderson, J. Lumin. **42**, 365 (1989).

[14] D.E. McCumber and M.D. Sturge, J. Appl. Phys. **34(6)**, 1682 (1963).

[15] T. Muramoto and T. Hashi, Phys. Lett. **51A(7)**, 423 (1975).

[16] W.H. Fonger and C.W. Struck, Phys. Rev. B **11(9)**, 3251 (1975).

[17] G.F. Imbusch, W.M. Yen, A.L. Schawlow, D.E. McCumber and M.D. Sturge, Phys. Rev. **133(4A)**, 1029 (1964).

[18] G.P. Morgan, T.J. Glynn, G.F. Imbusch and J.P. Remeika, J. Chem. Phys. **69**, 4859 (1978).

[19] M.J. Weber, J. Appl. Phys. **44(9)**, 4058 (1973).

[20] A. Monteil, C. Garapon and G. Boulon, J. Lumin. (1987).

[21] D.L. Graf and W.F. Bradley, Acta Cryst. **15**, 238 (1962).

[22] R.W.G. Wyckoff, Crystal Structures, 2nd ed., Interscience Publishers, **2**, p. 6 and 13 (1964).

CHAPTER 5

NEW STRUCTURAL CLASS OF SOLID-STATE OXIDE

Paul D. Thompson, Kathleen I. Schaffers,
Theodore Alekel III, James R. Cox,
and Douglas A. Keszler*

Department of Chemistry and
Center for Advanced Materials Research
Oregon State University
Gilbert Hall 153
Corvallis, Oregon 97331-4003

J. Am. Chem. Soc. **112**, 7068 (1990).

Contribution of Authors

Kathleen I. Schaffers synthesized and determined the structure of the $Sr_6HoSc(BO_3)_6$ derivative.

Theodore Alekel III developed the powder data processing software for determination of unit cell parameters.

James R. Cox synthesized the Ba analogues of the family.

All three of the above authors synthesized and determined unit cell parameters for many of the family members.

We recently described the relevance of the optical properties of the new borate $Sr_3Sc(BO_3)_3$ doped with the ion Cr^{3+} to the development of new laser materials [1]. We have now found that this material is only one example of a large and versatile family of solid-state oxides. It currently comprises the borates of formula $A_6MM'(BO_3)_6$ where A = Sr or Ba; M = lanthanide, Y, Sc, In, Bi, Ca, Mg, or Cd; and M' = small lanthanide, Y, Sc, Cr, Mn, Fe, Co, Ni, Zr, Sn, Ru, Rh, Hf, Al, Ga, In, or Mg. We have prepared more than 130 members of the family; representative formulas and their lattice parameters are listed in Table 5.1 [2]. All derivatives are readily prepared by standard high-temperature techniques with annealing temperatures ranging from 1175 K to 1375 K.

The structure adopted by these materials is best appreciated by inspection of Figures 5.1 and 3.4 (Chapter 3). Atoms M and M' occupy octahedral sites that are bridged by triangular BO_3 groups to form a one-dimensional chain, Figure 5.1. These chains pack in a trigonal manner according to the view in Figure 3.4 along the chain axis; the Sr atoms (small open circles) bridge adjacent chains by occupation of 9-coordinate sites. In each chain the octahedral sites of M and M' are crystallographically and chemically distinct. The site M is larger and exhibits an elongation along the chain axis whereas site M' is smaller and compressed along the same axis. This dissimilar

Table 5.1. Cell parameters for selected members of the family $A_6MM'(BO_3)_6$.

	a (Å)	c (Å)	V (Å^3)
$Sr_3Sc(BO_3)_3$*	12.135(1)	9.184(1)	1171.3(3)
$Sr_3Ho(BO_3)_3$	12.509(1)	9.254(1)	1254.0(2)
$Sr_6HoSc(BO_3)_6$*	12.285(3)	9.268(2)	1211.2(5)
$Sr_6YAl(BO_3)_6$	12.190(2)	9.109(5)	1172.3(1)
$Ba_6YFe(BO_3)_6$	12.797(1)	9.372(2)	1329.1(2)
$Sr_6CaZr(BO_3)_6$	12.453(1)	9.367(1)	1258.0(5)
$LaSr_5YMg(BO_3)_6$	12.237(2)	9.215(3)	1194.9(4)
$La_2Sr_4SrMg(BO_3)_3$	12.318(1)	9.254(2)	1216.1(2)

*single-crystal data

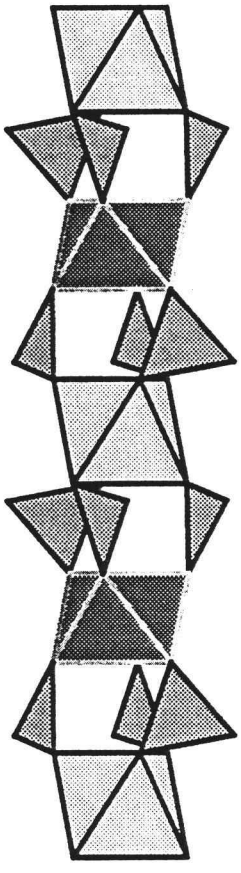

Figure 5.1. Sketch showing how the Sc-centered octahedra form a chain along the **c** axis of the unit cell. The compressed Sc1-O octahedra are darkened and the elongated Sc2-O octahedra are lightened in this figure.

nature of the octahedra contributes to the existence of the large number of ordered materials within the family.

The largest subgroup of the structural type forms with M and M' as tripositive cations in conjunction with the A atom Sr. The formula with M = M' = Sc corresponds to the material $Sr_3Sc(BO)_3$, and the formula with M = Ho and M' = Sc corresponds to the material $Sr_6HoSc(BO_3)_6$. The ordering that occurs between the two different octahedral sites when occupied by atoms M and M' of disparate sizes is one of the critical issues concerning the crystal chemistry of this family. A structure determination of the derivative $Sr_6HoSc(BO_3)_6$ indicates that it crystallizes in a selective manner with the Ho atom preferring the larger octahedral site and the Sc atom the smaller site [3]. The Ho-O and Sc-O distances, 2.296(4) Å and 2.092(4) Å, respectively, are consistent with values computed from crystal radii [4]. The crystal used for the structure determination was grown by melting the stoichiometric compound at 1773 K in a Pt crucible followed by cooling at 4 K/hr to 1273 K and 40 K/hr to 298 K. A small, light pink crystal was cleaved from the resulting transparent button and mounted for X-ray analysis.

We have found that Ba analogues crystallize in this structure type only in those instances where atoms M and M' have dissimilar sizes; derivatives with atoms M and M'

of similar sizes form a different, unique family of layered materials [5]. For example, the compound $Ba_6TbSc(BO_3)_6$ crystallizes in the chain structure whereas the compound $Ba_6HoSc(BO_3)_6$ crystallizes in the layered structure. The total formal charge (+6) of atoms M and M' may be realized by the combination of charges 2 + 4 as exemplified by the compounds $Sr_6CaZr(BO_3)_6$ and $Sr_6CdSn(BO_3)_6$. Smaller dipositive cations may be incorporated in compounds of the type $LaSr_5YMg(BO_3)_6$ and $La_2Sr_4SrMg(BO_3)_6$ where the La atom likely occupies a 9-coordinate site. In this way, a variety of derivatives containing, for example, dipositive transition-metal ions may be accessed. From consideration of current results it appears likely that all cations of formal charge +2, +3, or +4 that prefer octahedral or 9-coordinate environments can be incorporated into this structural type in significant amounts.

A full account of the crystal chemistry of these families of materials [5] as well as results on the optical and magnetic properties of selected members will be given in future articles.

Acknowledgments

This work was supported by the National Science Foundation, Solid State Chemistry Program and by the Department of Energy (W-7405-ENG-48) under subcontracts B076260 and 2143103 administered by Lawrence Livermore National Laboratory. DAK is grateful to the Alfred P. Sloan Foundation for a research fellowship, 1989 - 1991.

References

[1] P.D. Thompson and D.A. Keszler, Chem. Mater. **1**, 292 (1989).

[2] Each cell parameter was determined by least-squares analysis of 11 reflections obtained with an automated Philips powder diffractometer and corrected by using NBS Si standard 640b.

[3] Crystal and refinement data: space group $R\bar{3}$, a = 12.285(3) Å, c = 9.268(2) Å, V = 1211.2(5) $Å^3$, Z = 6; 693 observations with $I > 3\sigma(I)$ and 50 variables; R = 0.027, R_w = 0.041. A constrained refinement indicates a disorder of 8% between the Ho and Sc sites. Single-crystal X-ray diffraction data were collected on a Rigaku AFC6R diffractometer with graphite-monochromated Mo Kα radiation to sin θ_{max}/λ = 1.22 $Å^{-1}$.

[4] R.D. Shannon, Acta Crystallogr. A **32**, 751 (1976).

[5] K.I. Schaffers, P.D. Thompson, T. Alekel III, J.R. Cox, and D.A. Keszler, J. Solid State Chem., to be published.

CHAPTER 6

CHARACTERISTICS OF SELECTED MEMBERS OF A NEW STRUCTURAL FAMILY OF BORATES

Paul D. Thompson and Douglas A. Keszler*

Department of Chemistry and

Center for Advanced Materials Research

Oregon State University

Gilbert Hall 153

Corvallis, Oregon 97331-4003

Abstract

Synthetic techniques and crystal chemistry of a new family of orthoborates of formula $A_6MM'(BO_3)_6$, A = Sr, Pb, or Ln (Ln = lanthanide), M and M' = +2, +3, or +4 metal cation are presented. These oxides crystallize in the trigonal space group $R\bar{3}$ (#146) with unit cell volumes ranging from 1143.8(1) to 1227.6(2) $Å^3$. Over 135 individual members of the family have been synthesized with A = Sr providing materials with smaller cell volumes in comparison with those derivatives having A = Ba. Only Sr analogues are covered in this chapter. In this work I detail metal site occupancies, solid solubility characteristics, variations in unit cell volume, and luminescence characteristics of nine different members.

Introduction

In a recent communication we reported the discovery of a new material $Sr_3Sc(BO_3)_3$ [1] that was later found to be only one member of a new structural class of solid-state oxide, the largest family of orthoborates prepared to date [2]. I prepared 43 members of the family listed in Table 6.1. The materials have several features that make the family a potential source for many new phosphors and laser hosts. These include moderately high melting points (950 to 1650 °C), a 3-dimensional distribution of BO_3 groups (Chapter 3), and two distinct octahedral sites suitable for transition metal or small lanthanide doping. Separation of the octahedra by intervening BO_3 and SrO_9 groups should decrease or eliminate the concentration quenching that can limit emission efficiency in phosphors and laser materials.

Members form in space group $R\bar{3}$ with stoichiometry $A_6MM'(BO_3)_6$ wherein A = Sr, Ba, Pb, La, Pr, Nd, or Sm; M = Sc, Y, Bi, Sr, Eu, Tb, Ho, or Er; and M' = Mg, Al, Cr, Fe, Co, Ni, Zn, Sc, Y, In, Zr, Hf, or Sn. The materials crystallize in a trigonal structure in which MO_6 and $M'O_6$ octahedra are stacked alternately and linked by triangular planar BO_3 groups to form chains that extend along the **c**-direction in the unit cell. The MO_6 and $M'O_6$ octahedra are respectively elongated and compressed via trigonal

distortions along the **c**-axis of the unit cell (Figures 3.2, 3.4 and 5.1 and accompanying discussions). These chains of octahedra are bridged by AO_9 polyhedra in the **a** and **b** directions in the unit cell. Two current publications submitted by members of our research group detail the crystal structure of the entire family including A = Ba compounds [3] and a different material $Ba_3M(BO_3)_3$ (M = Y, Sc) that forms a layered structure [4]. The $A_6MM'(BO_3)_6$ structure forms when A = Sr or when the cations M and M' have disparate sizes and A = Ba. The layered $Ba_3Y(BO_3)_3$ structure forms when A = Ba and M and M' are identical or have similar sizes.

For reference, Table 6.1 contains the 43 members that I prepared. The materials in Table 6.1 are arranged into four different types, depending on the valences and site occupancies of the A, M, and M' atoms constituting the compound. Group I has A = Sr or Pb and M,M' = +3 transition metal or rare earth cation. In two cases (Sc and Y), M and M' sites are occupied by the same metal atom. A lone unique material included with Group I is $Pb_2Sr_4ScSc(BO_3)_6$ that has two Sr atoms replaced by two Pb atoms. I expect that Pb would substitute in varying amounts for Sr in many of the materials in which A = Sr.

Group II has A = Sr with M = larger +2 cation Cd, Ca or Sr, and M' = smaller +4 cation Zr, Hf, or Sn. In Group III one Sr^{2+} ion has been replaced by one Ln^{3+} ion (Ln =

Table 6.1. Members of the $A_6MM'(BO_3)_6$ family. Count = 43.

Compound	a (Å)	c (Å)	V (Å^3)[a]
Group I: M,M' = III,III			
$Sr_6ScAl(BO_3)_6$	12.082(1)	9.047(1)	1143.8(1)
$Sr_6ScCr(BO_3)_6$	12.104(1)	9.095(2)	1154.0(2)
$Sr_6ScGa(BO_3)_6$	12.143(1)	9.146(1)	1167.8(2)
$Sr_6ScSc(BO_3)_6$	12.135(1)	9.184(1)	1171.3(3)
$Pb_2Sr_4ScSc(BO_3)_6$	12.171(1)	9.186(1)	1178.4(2)
$Sr_6YAl(BO_3)_6$	12.190(2)	9.109(5)	1172.3(5)
$Sr_6YCr(BO_3)_6$	12.213(1)	9.146(1)	1181.5(2)
$Sr_6YSc(BO_3)_6$	12.284(1)	9.268(2)	1211.2(4)
$Sr_6YY(BO_3)_6$	12.503(2)	9.248(2)	1252.1(4)
$Sr_6EuAl(BO_3)_6$	12.254(1)	9.126(2)	1186.7(2)
$Sr_6BiAl(BO_3)_6$	12.279(1)	9.142(2)	1193.7(2)
$Sr_6BiFe(BO_3)_6$	12.310(2)	9.215(2)	1209.4(3)
$Sr_6TbIn(BO_3)_6$	12.329(1)	9.219(1)	1213.5(3)
$Sr_6EuIn(BO_3)_6$	12.361(1)	9.234(1)	1221.9(2)
Group II: M,M' = II,IV			
$Sr_6CdSn(BO_3)_6$	12.434(2)	9.236(2)	1236.5(3)
$Sr_6CdHf(BO_3)_6$	12.412(1)	9.346(2)	1246.8(3)
$Sr_6CaHf(BO_3)_6$	12.460(2)	9.358(3)	1258.3(4)
$Sr_6CdZr(BO_3)_6$	12.469(2)	9.371(2)	1261.7(4)
$Sr_6SrZr(BO_3)_6$	12.512(1)	9.392(1)	1273.5(1)
Group III: A = RE,Sr M,M' = III,II			
$SmSr_5YNi(BO3)_6$	12.175(2)	9.159(3)	1175.9(3)
$PrSr_5YNi(BO_3)_6$	12.182(2)	9.170(2)	1178.4(3)
$NdSr_5YNi(BO_3)_6$	12.208(2)	9.169(2)	1183.4(3)
$LaSr_5ErNi(BO_3)_6$	12.199(1)	9.184(1)	1183.6(2)
$LaSr_5EuNi(BO_3)_6$	12.254(1)	9.214(1)	1198.3(1)
$LaSr_5ScNi(BO_3)_6$	12.295(1)	9.250(1)	1210.9(1)
$NdSr_5YMg(BO_3)_6$	12.185(1)	9.180(2)	1180.4(2)
$SmSr_5YMg(BO_3)_6$	12.213(1)	9.171(2)	1184.6(3)
$PrSr_5YMg(BO_3)_6$	12.227(1)	9.188(2)	1189.5(2)
$LaSr_5TbMg(BO_3)_6$	12.273(1)	9.216(2)	1202.1(2)
$SmSr_5YZn(BO_3)_6$	12.205(1)	9.177(2)	1183.9(3)
$PrSr_5YZn(BO_3)_6$	12.217(2)	9.197(3)	1188.8(4)
$NdSr_5YZn(BO_3)_6$	12.257(2)	9.199(3)	1196.8(3)
$NdSr_5ErZn(BO_3)_6$	12.272(1)	9.198(1)	1199.7(2)

Table 6.1. (cont'd)

$NdSr_5EuZn(BO_3)_6$	12.273(1)	9.212(1)	1201.7(2)
$NdSr_5HoCo(BO_3)_6$	12.218(1)	9.179(1)	1186.7(1)
$NdSr_5ErCo(BO_3)_6$	12.251(1)	9.180(2)	1193.1(2)
$LaSr_5HoCo(BO_3)_6$	12.241(1)	9.204(1)	1194.3(2)
$NdSr_5TbCo(BO_3)_6$	12.269(1)	9.199(2)	1199.2(2)
$NdSr_5ScCo(BO_3)_6$	12.257(1)	9.220(2)	1199.6(2)
$LaSr_5ScCo(BO_3)_6$	12.290(1)	9.251(2)	1210.1(2)
Group IV: A = RE,Sr M,M' = II,II			
$Nd_2Sr_4SrMg(BO_3)_6$	12.268(1)	9.212(1)	1200.5(2)
$La_2Sr_4SrZn(BO_3)_6$	12.319(2)	9.264(2)	1217.4(3)
$La_2Sr_4SrCd(BO_3)_6$	12.364(1)	9.273(2)	1227.6(2)

[a] Values were found to be within +/- 0.1% for **a**, +/- 0.2% for **c** and +/- 0.5% for V. Transformed into actual distances and volumes: **a** +/- 0.013 Å, **c** +/- 0.019 Å, and V +/- 6 $Å^3$.

Sm, Pr, Nd, or La) to charge-compensate for one +2 cation placed in the M' site (Ni, Mg, Zn, or Co). In Group IV, two A = Sr atoms have been replaced by +3 cations La or Nd to charge-compensate for Sr^{2+} on the larger M site and Mg^{2+}, Zn^{2+}, or Cd^{2+} occupying the smaller M' site.

When the M and M' atoms are more dissimilar in size a stronger preference of the large cation for the M site and small cation for the M' site can occur, as in $Sr_6YAl(BO_3)_6$ which can be made as an ordered compound with Y:Al = 1:1. (Synthesis may also result in compositions with excess Y occupying some of the Al sites.) Further single crystal studies are expected to reveal varying amounts of site disorder in different family members. I expect that, in general, as the $R_M/R_{M'}$ ratio becomes smaller the materials become more highly disordered.

Synthesis

Powders of each of the $A_6MM'(BO_3)_6$ (A = Sr) derivatives were synthesized by ordinary solid-state methods. Stoichiometric ratios of the starting reagents (nitrates, carbonates, oxalates, and oxides) with a 5 mol % excess of B_2O_3 were ground and heated at 923 K for 1-2 hr to decompose the reactants. The samples were then reground and heated at 1023 K for 4-6 hr, 1123 K for 12 hr, and a final sintering temperature between 1173 and

1400 K for 24 hr with intermittent grindings. X-ray powder diffraction data confirmed formation of the desired product. Further synthesis studies have revealed that pure powders of many of the derivatives can also be synthesized by utilizing a flash-synthesis technique. The reagents were ground and heated at 923 K for 1 hr. The mixture was then ground and flashed at 1223 or 1273 K for 2-4 hr. The parameters for the flash method were determined by initially heating a sample at 1123 K, then increasing the temperature in 50 K increments to the point where the sample sintered. If the desired product formed, the reaction mixture was flashed directly to the sintering temperature following decomposition of the starting reagents.

Results and Discussion

Powder data for the materials were collected on an automated Philips diffractometer, and peak positions were corrected by using NIST Si Standard 640b. Unit cell parameters were determined by least squares analysis of eleven corrected peaks in the range $26° < 2\theta < 58°$. The hkl assignment of each reflection was made from comparison to the powder pattern of the parent material $Sr_3Sc(BO_3)_3$ [6].

To establish experimental error in unit cell parameters, six pairs of samples were compared to determine the variation of cell parameters **a** and **c**, and unit cell volumes **V**. The maximum differences found (Δa, Δc, and ΔV) were used as an estimate of maximum deviation from an average value. Reported values were found to be within +/- 0.1 % for **a**, +/- 0.2 % for **c**, and +/- 0.5 % for **V**. Variations in metrical units (Å and $Å^3$) are included in the subscript to Table 6.1. The variability inherent in reported cell parameters explains why some members seem to be misplaced on the list, as is the case with $NdSr_5YMg(BO_3)_6$ and $SmSr_5YMg(BO_3)_6$. In each case inclusion of a larger cation must result in a larger unit cell but this may not show up if the enlargement is less than the experimental error associated with the synthetic procedure and cell parameter determination. Reported standard

deviations in Table 6.1 originate from the least squares program and reflect the certainty with which the least squares fit has settled on a specific value. Actual variations in unit cell parameter values up to 0.019 Å are an order of magnitude larger than standard deviations derived from the computer program. Sources of experimental error include impure starting reagents, weighing errors, broad diffraction peaks from poor sample crystallinity, inhomogeneous skewing of peak shapes, and the elements of selecting peak positions.

Solid Solution Behavior

Formation of solid solutions was examined by synthesizing two series: $Sr_6Sc_{2-x}Al_x(BO_3)_6$ (x = 0 to 1.2) at 950 °C, and $Sr_6Y_{2-x}Al_x(BO_3)_6$ (x = 0 to 2.0) at 1000 to 1050 °C; the examinations yielded different results. Results from the first series are shown in Figure 6.1. The cell parameter **a** decreases linearly as the Sc atom is replaced by the smaller Al atom on the M' site. The **c** cell parameter exhibits similar behavior. Cell parameters level off beyond x = 1 indicating Al does not occupy the larger M site to any appreciable extent. This observation is further supported by the nonexistence of the material $Sr_3Al(BO_3)_3$ under the same synthesis conditions. The Al atom is too small to support the structure by itself yet

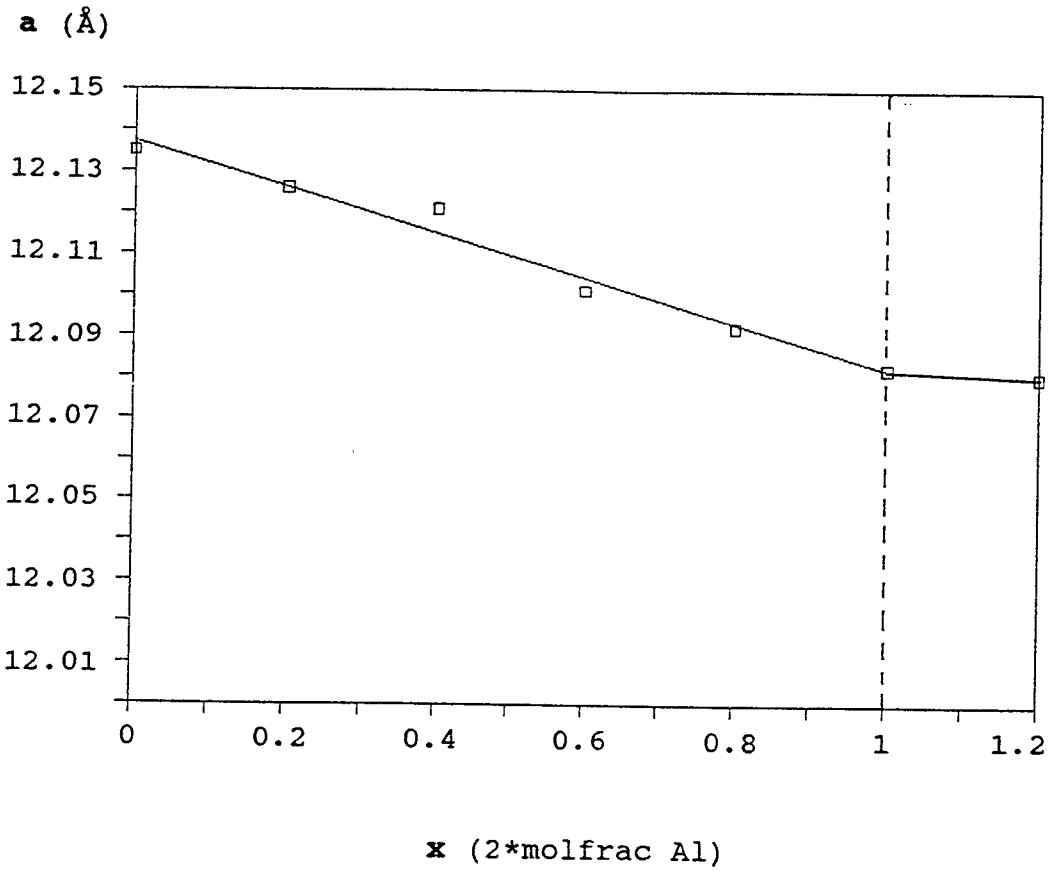

Figure 6.1. A plot of the **a** cell parameter of the solid solution series $Sr_6Sc_{2-x}Al_x(BO_3)_6$ (x = 0 to 1.2). The plot shows steady decrease of unit cell edge length as Al content increases. The **c** parameter and cell volume exhibit the same trend.

readily forms the x = 0 to 1 solid solution.

Results (Figure 6.2) from the series $Sr_6Y_{2-x}Al_x(BO_3)_6$ indicated a much different behavior. A plot of unit cell parameter **a** versus Al-content in Figure 6.2 reveals a limited solubility of Al in $Sr_3Y(BO_3)_3$ and a very limited solubility of Y on the M' site in $Sr_6Y_{1+x}Al_{1-x}(BO_3)_6$. A miscibility gap is observed at the temperature of the experiment.

The behavior of forming a solid solution in the first series and not in the second is consistent with the relative ion sizes: R_{Sc}/R_{Al} = .885/.675 = 1.31 and R_Y/R_{Al} = 1.06/.675 = 1.57 [5]. The similar sizes of the Sc and Al atoms allow occupation of the M' site by either atom, maintaining structural integrity. In the Y-Al series, the disparate sizes of the atoms would afford a chain in the structure incommensurate with the surrounding Sr borate matrix. Hence, phase segregation is observed with primary retention of the phases $Sr_3Y(BO_3)_3$ and $Sr_6YAl(BO_3)_6$. Also, in general, highly stable, ordered materials form in the family when the M/M' ratio is large. This behavior is especially observed for members with A = Ba. Cations with large M/M' ratio form the $A_6MM'(BO_3)_6$ structure and cations of similar sizes form the $Ba_3Y(BO_3)_3$ layered structure.

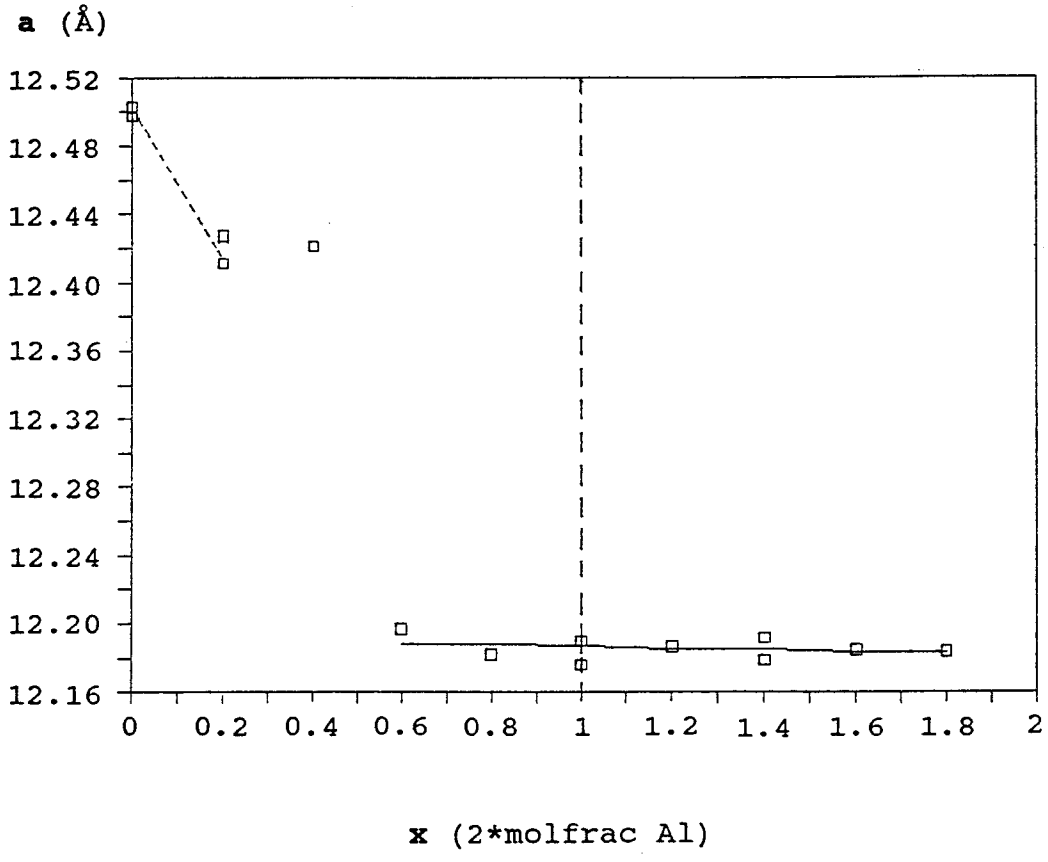

Figure 6.2. A plot of the **a** cell parameter of the series $Sr_6Y_{2-x}Al_x(BO_3)_6$ (x = 0 to 1.8). The plot reveals the existence of two distinct phases, $Sr_3Y(BO_3)_3$ (at x = 0) and $Sr_6YAl(BO_3)_6$ (at x = 1). Data points at x = 0.2 and 0.4 indicate that some Al is dissolved in the $Sr_3Y(BO_3)_3$ phase. The line between x = 0.6 and 1.8 indicates no solubility of Y and little solubility of Al in $Sr_6YAl(BO_3)_6$.

Luminescence Characteristics

Experiments reveal that family members with M and M' cations having sizes and electronegativities similar to Sc^{3+} exhibit similar optical properties when doped with the ion Cr^{3+}. Results were obtained from materials with A = Sr, M = In, Sc, and Y; and M' = In, Sc, Al, and Cr. A room-temperature emission spectrum of $Cr^{3+}:Sr_3In(BO_3)_3$ (Figure 6.3) exhibits $^2E \rightarrow {}^4A$ sharp peaks and a $^4T \rightarrow {}^4A$ broad band just as observed for the sample $Cr^{3+}:Sr_3Sc(BO_3)_3$ (Figure 2.2). The broad band of the In analogue is narrower than the broad band of the Sc compound. This indicates that the slope of the ^4T state is steeper in the Sc compound than in the In analogue. The substitutional site in the latter compound is not affected as strongly by crystal field strength as in the Sr compound.

Concentration Quenching

I have found that increasing the concentration of the emitting ion from dopant levels to stoichiometric amounts (with M' = Cr^{3+}) does not result in a complete loss of emission as with materials that show concentration quenching. The room temperature emission spectra for $Sr_6InSc(BO_3)_6$ doped with 2 mol % Cr^{3+} and $Sr_6InCr(BO_3)_6$ (50 mol % Cr^{3+}) shown in Figures 6.4 and 6.5, respectively,

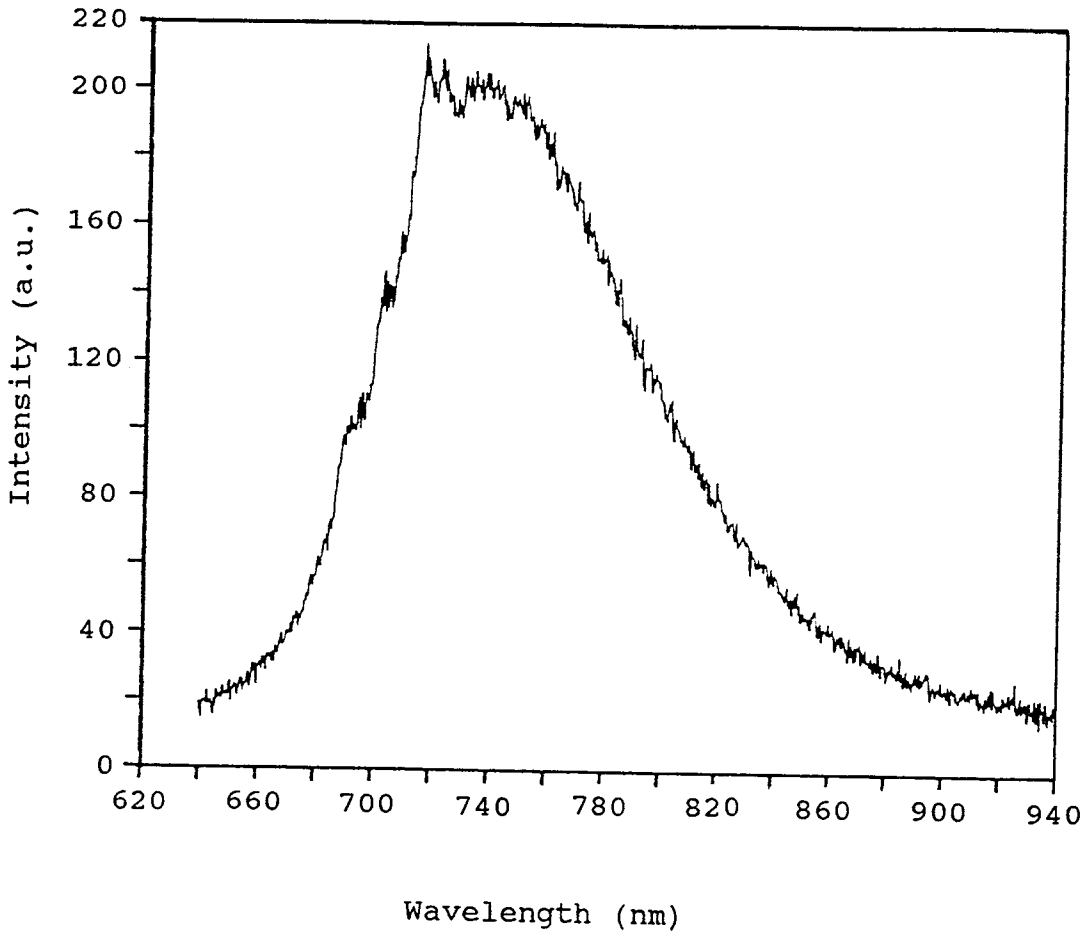

Figure 6.3. Room temperature luminescence spectrum of $Cr^{3+}:Sr_3In(BO_3)_3$ showing a broad band that is narrower than the broad band in $Cr^{3+}:Sr_3Sc(BO_3)_3$ (Figure 2.2).

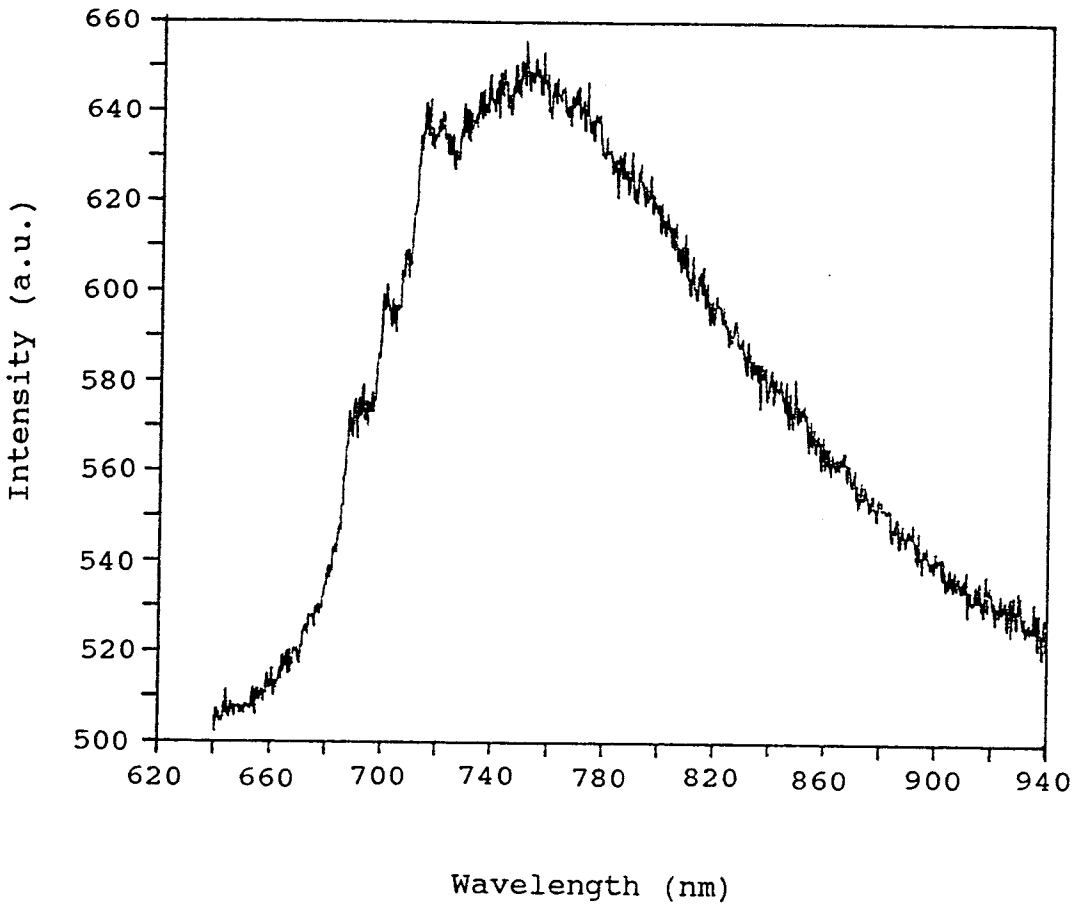

Figure 6.4. Room temperature luminescence spectrum of $Cr^{3+}:Sr_6InSc(BO_3)_6$.

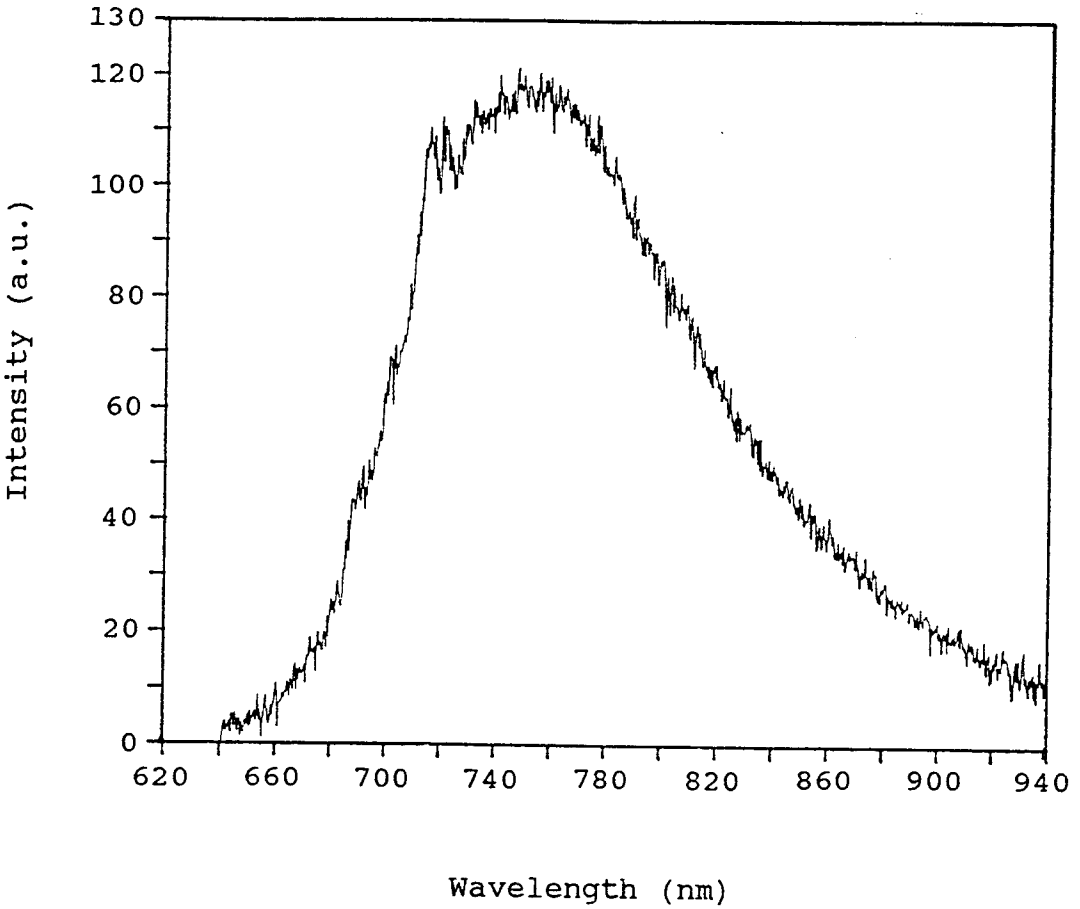

Figure 6.5. Emission spectrum of the stoichiometric material $Sr_6InCr(BO_3)_6$.

confirm this property.

The lack of total concentration quenching is also exhibited by the material $Sr_6ScCr(BO_3)_6$ which displayed an intense luminescence spectrum given in Figure 6.6. In both $Sr_6ScCr(BO_3)_6$ and $Sr_6InCr(BO_3)_6$ lack of complete concentration quenching is probably caused by isolation of the MO_6 and $M'O_6$ octahedra from each other. Because of this separation the rate of energy transfer to neighboring Cr^{3+} ions that are in the ground state is probably low. Another material exhibiting an intense room temperature emission (Figure 6.7) is $Sr_6YCr(BO_3)_6$.

$Sr_6YAl(BO_3)_6$ Phonon Spectrum

A combined plot of room temperature and 77 K emission spectra of $Cr^{3+}:Sr_6YAl(BO_3)_6$ showing similar characteristics to $Cr^{3+}:Sr_3Sc(BO_3)_3$ (Figure 2.2) is presented in Figure 6.8. The room temperature spectrum is more intense and inhomogeneously broadened relative to the $Sr_3Sc(BO_3)_3$ spectrum. The low temperature spectrum exhibits R-line blue shift and variations of intensity of the two sets of phonon peaks at 744 nm and 725 nm. Insufficient resolution has prevented me from analyzing any single-phonon progression that may be present. The R-line split for this material (39 cm^{-1}) is larger than the split exhibited by $Cr^{3+}:Sr_3Sc(BO_3)_3$ (29.8 cm^{-1}) indicating

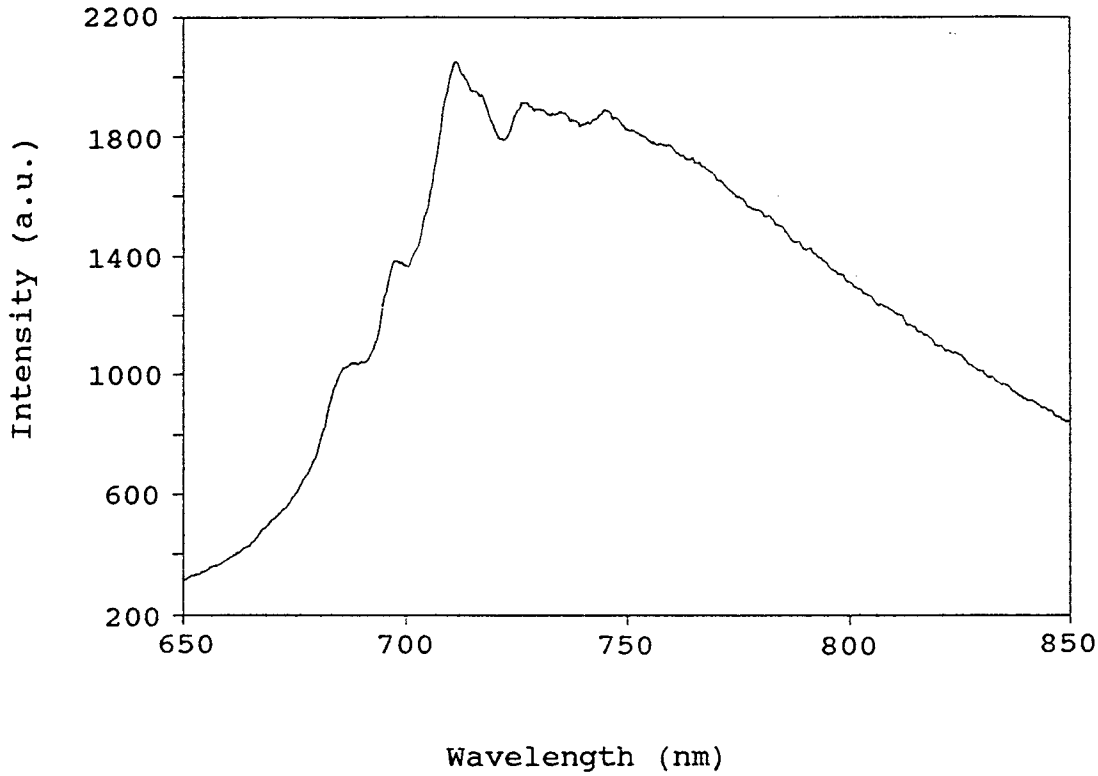

Figure 6.6. Intense emission spectrum displayed by the stoichiometric material $Sr_6ScCr(BO_3)_6$. Excitation wavelength (λ_x) was 462 nm.

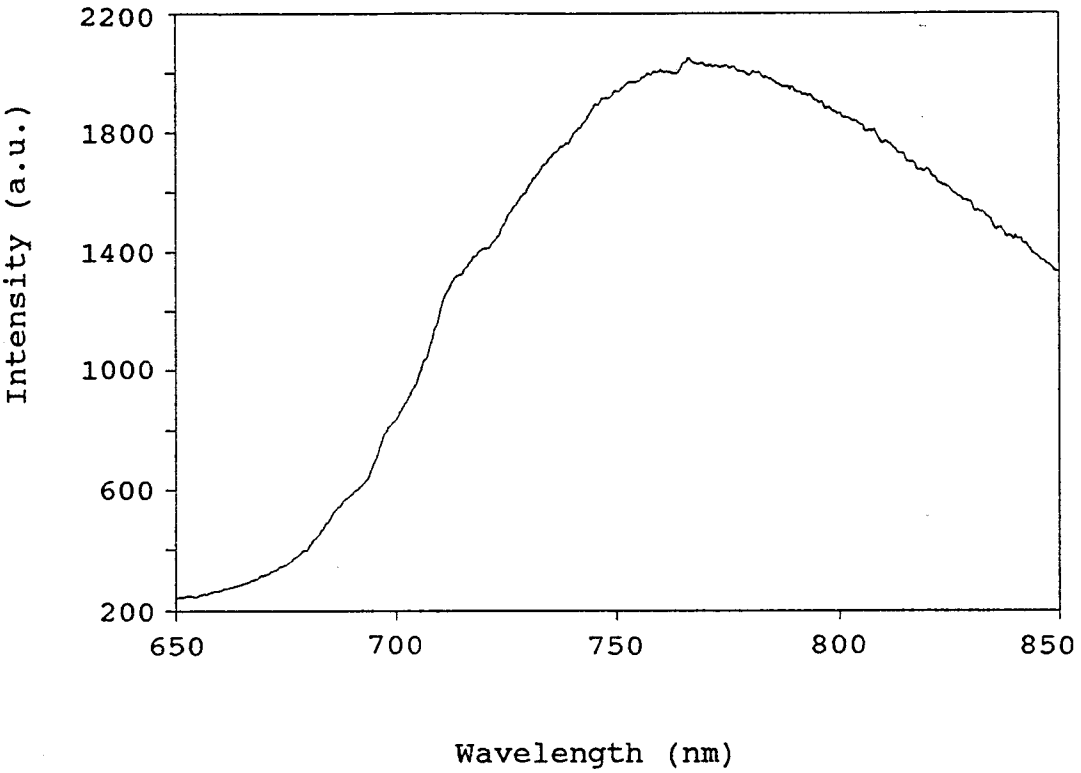

Figure 6.7. Emission spectrum of $Sr_6YCr(BO_3)_6$ showing disappearance of sharp lines and red-shift of λ_{max} for the broad band relative to $Sr_6ScCr(BO_3)_6$ shown in the previous figure.

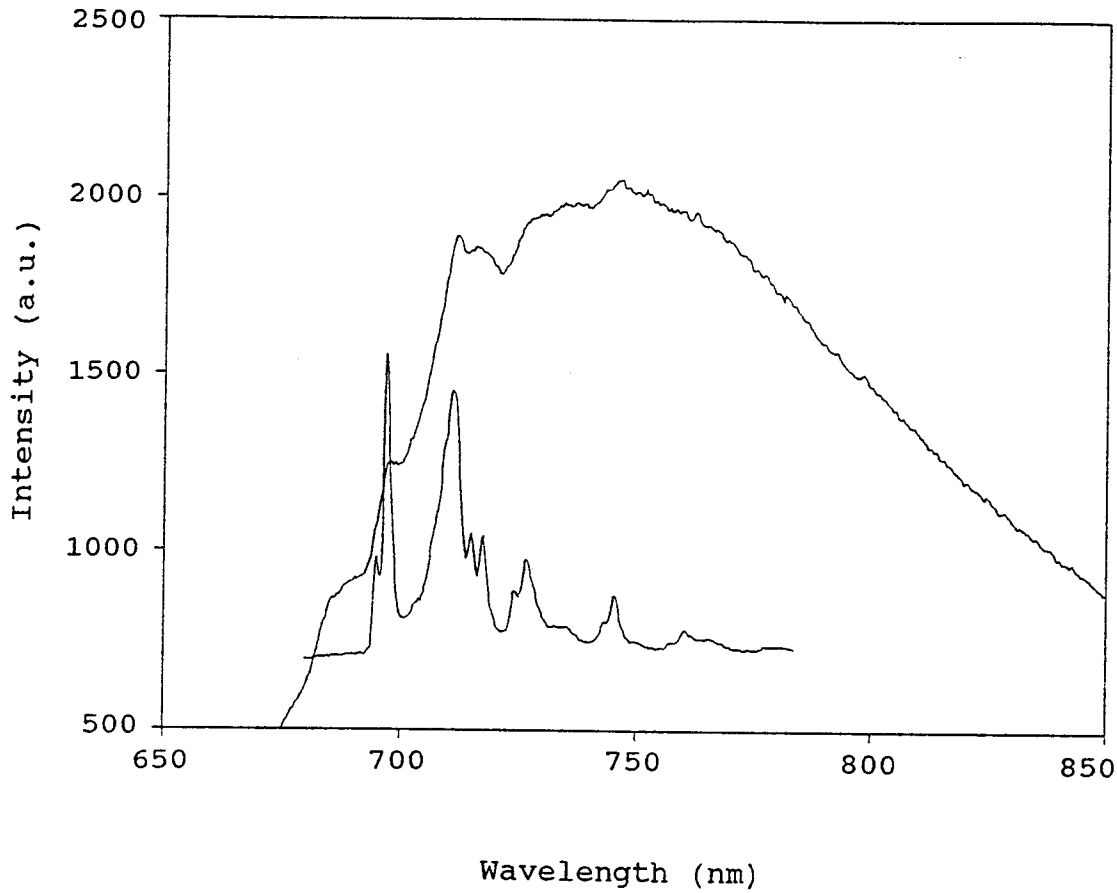

Figure 6.8. Room temperature and 77 K emission spectra for $Cr^{3+}:Sr_6YAl(BO_3)_6$ plotted together. The 77 K spectrum exhibits R-line blue shift and phonon-assisted peaks.

that the $^2E \rightarrow \bar{E} + 2\bar{A}$ separation is larger for the YAl analogue. As a result the R2/R1 intensity ratio is larger for the YAl analogue than for the Sc compound. The lowered intensity of the R2 peak is the result of a smaller Boltzmann distribution into the upper ^2E state ($2\bar{A}$) caused by the larger energy separation.

Rare Earth Luminescence

I synthesized several family members with rare earth cations present in stoichiometric amounts. I expect rare earth cations to occupy primarily the larger M site, although cations such as Eu^{3+} could also be on the A site. The room temperature luminescence spectra for $Sr_6EuSc(BO_3)_6$ and $Sr_6TbAl(BO_3)_6$ (Figures 6.9 and 6.10) reveal characteristic emission peaks for these rare earth ions without complete concentration quenching. Reagent expense would limit production of phosphors to materials such as $Pb^{2+},Eu^{3+},Tb^{3+}:Sr_6YAl(BO^3)_6$ with the rare earth cations and Pb^{2+} present in dopant amounts. The Nd^{3+} ion in $NdSr_5EuZn(BO_3)_6$ completely quenches Eu^{3+} luminescence in that compound.

Low Temperature Quench of Non-radiative Pathway

Room temperature and 77 K luminescence spectra for

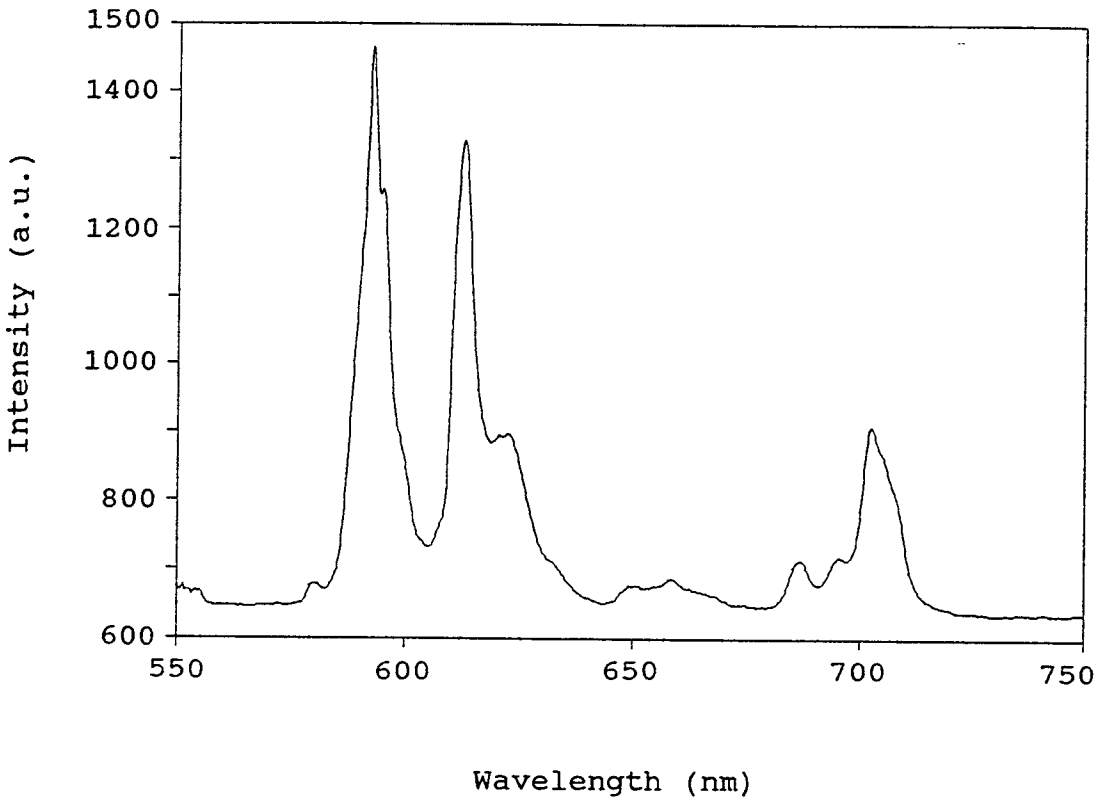

Figure 6.9. Room temperature emission spectrum of $Sr_6EuSc(BO_3)_6$. λ_x was 396.5 nm.

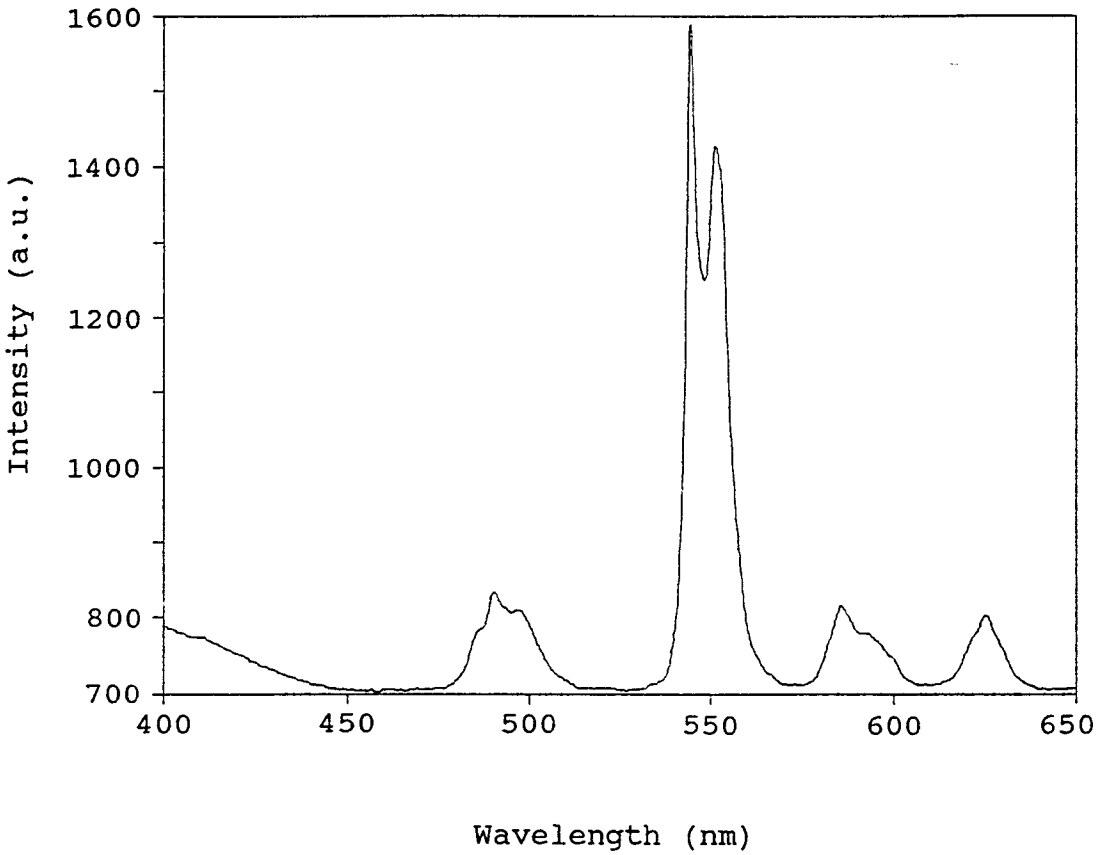

Figure 6.10. Room temperature luminescence spectrum of $Sr_6TbAl(BO_3)_6$.

$Sr_6TbIn(BO_3)_6$ presented in Figures 6.11 and 6.12, respectively, are similar except for the group of highest energy peaks occurring between 452 and 487 nm in the low temperature spectrum. The four peaks occurring at 491, 545, 591, and 619 nm are nearly the same in both spectra because the rare earth 4f-electrons are well shielded by 4d, 5s, and 5p electrons and have minimal interaction with host lattice electrons for that reason. The primary difference in the spectra is the appearance of the additional high energy peaks when the sample temperature is 77 K. Since these peaks do not occur in the room temperature spectrum nonradiative pathways must exist at room temperature to remove the energy of electrons excited into these higher levels.

An energy-level diagram from Dieke of the 4f energy levels in Tb^{3+} is presented in Figure 6.13. The most intense peak occurring at 545 nm is the $^5D_4 \rightarrow {}^7F_6$ transition. Two lower energy peaks and one higher energy peak exist in both the room temperature and the low temperature spectra. I have drawn four solid arrows in the diagram to indicate four transitions that are consistent with the 545 nm transition. The dotted arrow indicates the higher energy transitions that exist only when the material is cooled to 77 K.

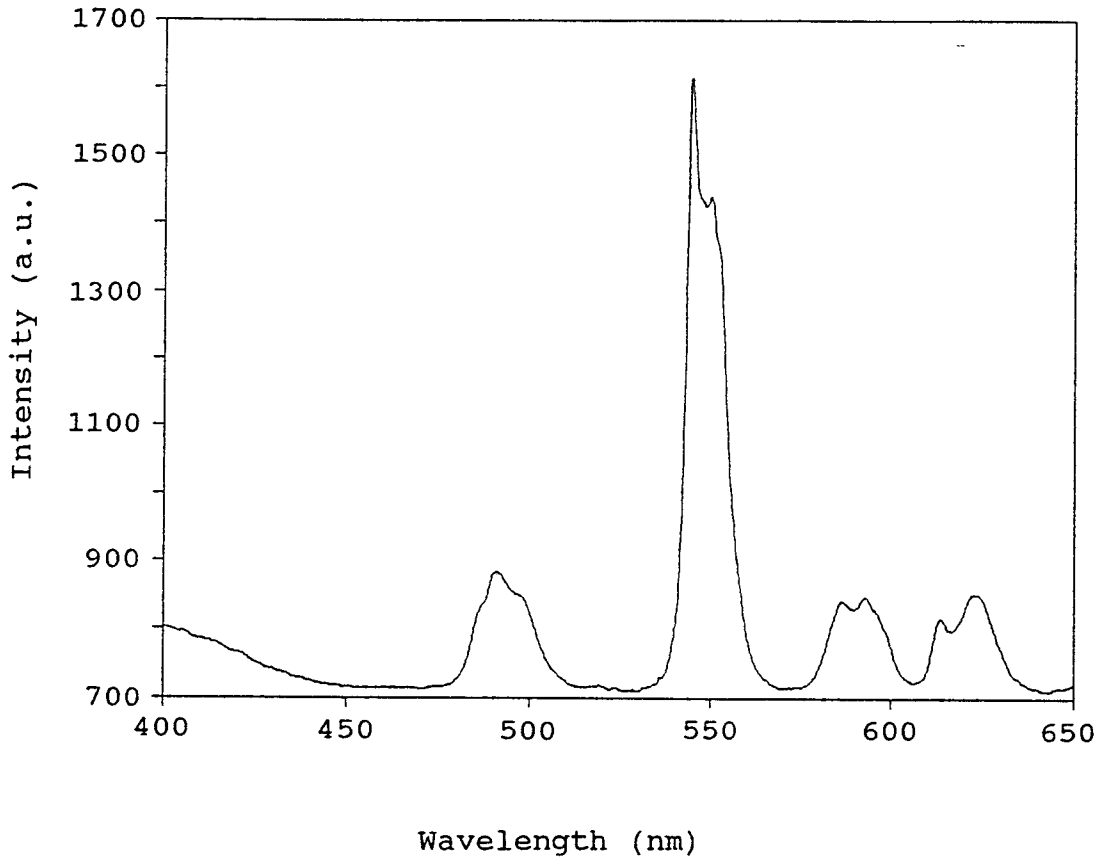

Figure 6.11. Room temperature luminescence spectrum of $Sr_6TbIn(BO_3)_6$ exhibiting four sets of peaks. λ_x was 377 nm.

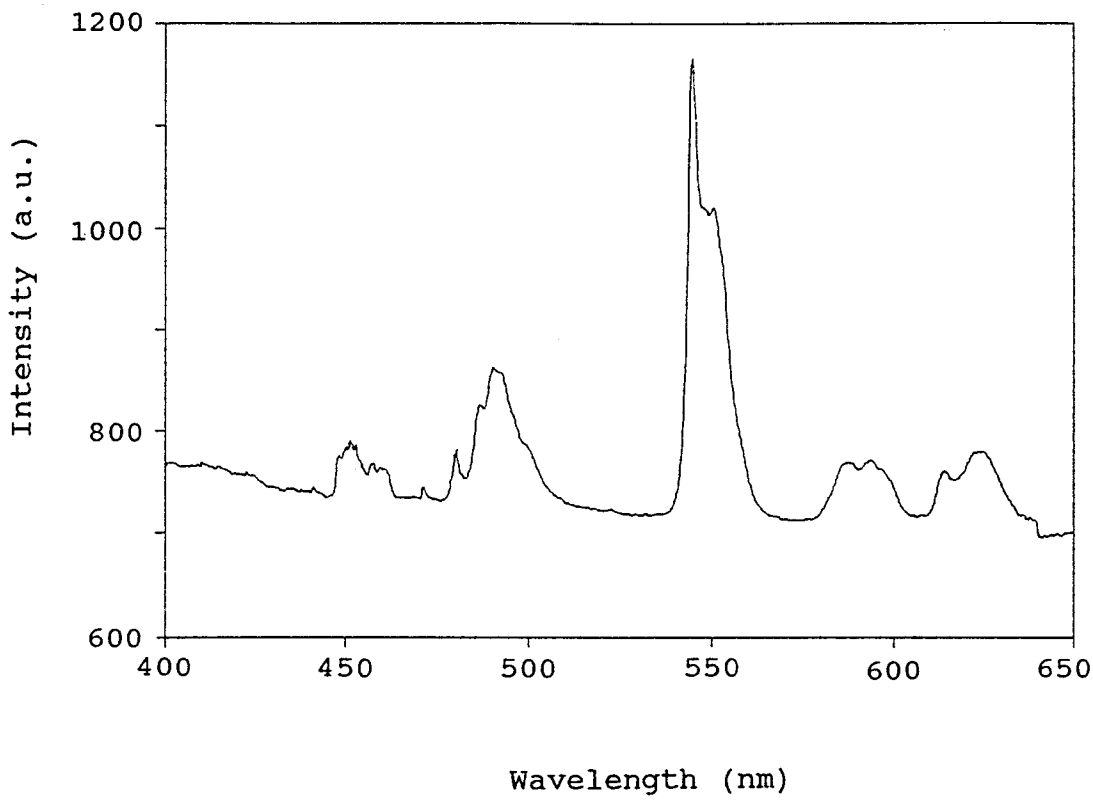

Figure 6.12. 77 K luminescence spectrum of $Sr_6TbIn(BO_3)_6$ exhibiting appearance of higher energy peaks between λ = 452 and 481 nm.

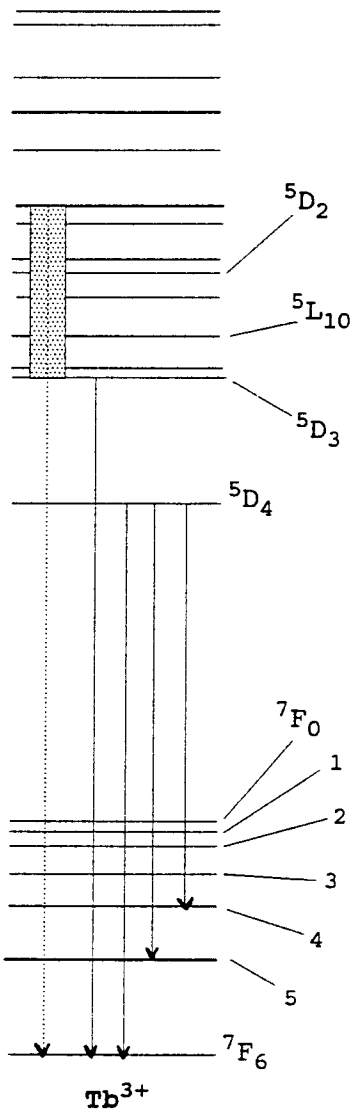

Figure 6.13. Electronic energy level diagram for the Tb^{3+} ion. The four solid arrows show the transitions that give rise to the four sets of peaks observed in the room temperature spectrum. The rectangular box and dotted arrow shows the higher energy levels from which the new peaks in the low temperature spectrum originate.

Conclusion

The large borate family $A_6MM'(BO_3)_6$ contains many members that are potentially useful as phosphors or laser crystals. I expect that growth of large single crystals of selected family members and spectroscopic characterization of many of the compounds in the family will facilitate eventual application of these compounds as valuable optical materials.

Acknowledgment

Kathleen I. Schaffers provided the samples for optical studies that I present in Figures 6.3 and 6.5.

References

[1] P.D. Thompson and D.A. Keszler, Chem. Mater. **1**, 292 (1989).

[2] K.I. Schaffers, T. Alekel III, P.D. Thompson, J.R. Cox, and D.A. Keszler, J. Am. Chem. Soc. **112**, 7068 (1990).

[3] K.I. Schaffers, P.D. Thompson, T. Alekel III, J.R. Cox, and D.A. Keszler, to be submitted.

[4] J. Huang and D.A. Keszler, to be submitted.

[5] R.D. Shannon, Acta Crystallogr. A, **32**, 751 (1976).

[6] P.D. Thompson and D.A. Keszler, to be submitted.

CHAPTER 7

THE MIXED ORTHOBORATE PYROBORATE $Sr_2Sc_2B_4O_{11}$, FIRST OF A KIND

Paul D. Thompson and Douglas A. Keszler*

Department of Chemistry and

Center for Advanced Materials Research

Oregon State University

Gilbert Hall 153,

Corvallis, Oregon 97331-4003 USA

Excerpts from J. Solid State Chem., in press.

Abstract

A new alkaline-earth scandium borate, the mixed orthoborate pyroborate $Sr_2Sc_2B_4O_{11}$ has been synthesized and structurally characterized by single-crystal X-ray diffraction methods. The compound may be represented by the descriptive formula $Sr_2Sc_2(BO_3)_2(B_2O_5)$ which indicates two orthoborate groups and one pyroborate group for each formula unit. This compound represents the first known instance of both groups occurring together in the same material. The compound crystallizes in the triclinic system in space group $P\bar{1}$ (#2) with cell parameters a = 6.293(3), b = 7.285(3), c = 5.084(3) Å, α = 90.71(5), β = 104.68(4), γ = 78.07(4)°, and V = 220.4(4) Å^3. The structure exhibits layers composed of an admixture of orthoborate and pyroborate groups. These layers are interleaved by Sr atoms occupying 8-coordinate sites and Sc atoms occupying distorted octahedral sites. The geometry of the pyroborate group is unusual, all atoms residing in the same plane and exhibiting the angle B-O-B = 180°.

Introduction

The simplest condensation of triangular groups in borate chemistry affords the pyroborate anion $B_2O_5^{4-}$, Figure 7.1. In reported examples of pyroborates [1-14], the terminal BO_2 planes pivot about the torsion angles τ_1 and τ_2 to afford deviations from coplanarity that range from 1.6° to 67.0° while the central B-O-B angle ranges from 111.8° to 138.7°. In this paper we describe the new, mixed orthoborate pyroborate $Sr_2Sc_2B_4O_{11}$ in which the pyroborate group adopts a unique planar geometry with B-O-B angle constrained by symmetry to be 180°. A simple analysis of the bonding in the group and pyroborate groups in other compounds is also presented.

The compound $Sr_2Sc_2B_4O_{11}$ has resulted from our continuing interest in phase equilibria in the system SrO-Sc_2O_3-B_2O_3 [15].

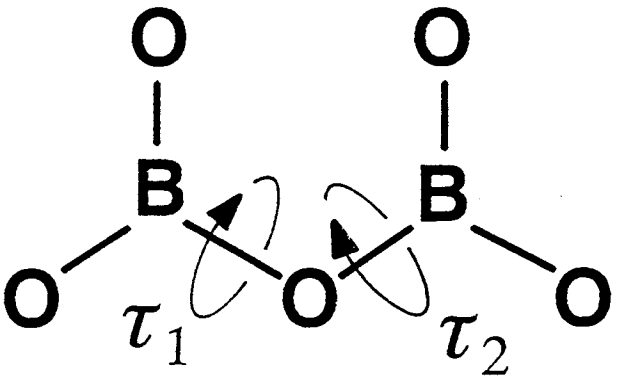

Figure 7.1. Diagram showing the two angles, τ_1 and τ_2, about which the two BO_2 ends of the pyroborate group can rotate.

Preparation and X-ray Work

Powdered samples of the material $Sr_2Sc_2B_4O_{11}$ were prepared by separately heating the stoichiometric mixtures $Sr_2B_2O_5 + 2ScBO_3$ and $\frac{2}{3}Sr_3B_2O_6 + 2ScBO_3 + \frac{1}{3}B_2O_3$. The binary borates were prepared by heating stoichiometric quantities of the reagents $Sr(NO_3)_2$ (reagent grade, J. T. Baker), Sc_2O_3 (reagent grade, Boulder Scientific), and B_2O_3 (99.99% ALFA) at 950°C for 12 hr. Combinations of the binary borates were pressed into pellets and annealed at 950°C for 12 hr and 1050°C for 12 hr. The X-ray powder diffraction pattern of the samples compares well to the pattern calculated by using the program LAZY-PULVERIX [16] and the results of the structure determination.

Single crystals of the compound were isolated from a mixture containing the phases $Sr_3B_2O_6$ and $ScBO_3$ in the molar ratio 1:4 that was melted at 1465°C and cooled to room temperature by simply turning the power to the furnace off. A crystal of dimensions 0.1 x 0.2 x 0.25 mm was physically separated from the matrix and mounted on a Rigaku AFC6R diffractometer for data collection. Unit cell parameters were established by least-squares analysis of 24 reflections in the range $30.14 \leq 2\theta \leq 34.10°$; crystal data are listed in Table 7.1. Data were collected by using the ω-2θ scan method with a scan speed of 32°/min in 2θ to $\sin \theta_{max}/\lambda = 0.648$ Å^{-1}. From 1125 reflections

Table 7.1. Crystallographic Data for $Sr_2Sc_2B_4O_{11}$.

formula	$Sr_2Sc_2B_4O_{11}$
formula weight, amu	484.39
a, Å	6.293(3)
b, Å	7.285(3)
c, Å	5.084(3)
α, °	90.71(5)
ß, °	100.68(4)
γ, °	78.07(4)
V, $Å^3$	220.4(4)
Z	1
space group	$P\bar{1}$ (#2)
T, K	296
λ	0.71069 Å, Mo Kα (graphite monochromated)
D_{calc}, g cm^{-3}	3.65
μ, cm^{-1}	132.11
transmission coefficients	0.775 - 1.333
R (F_o)	0.024
R_w (F_o)	0.034

measured in the range of indices $-7 \leq h \leq 7$, $-9 \leq k \leq 9$, and $0 \leq l \leq 6$, a total of 970 data were observed ($F_o^2 > 3\sigma(F_o^2)$). The structure was solved and refined with programs from the TEXSAN crystallographic software package [17]. Patterson methods afforded the location of the Sr and Sc atoms. The positions of the remaining atoms were subsequently found by analysis of difference electron density maps. Following refinement of the model with isotropic thermal parameters on each atom, the data were corrected for absorption with the computer program DIFABS [18]. Final least-squares refinement on $|F|$ with anisotropic thermal parameters on each atom resulted in the final residuals $R = 0.024$ and $R_w = 0.034$ with $\Delta/\sigma = 0.002$. The final difference electron density map afforded a maximum peak = 0.962 e/Å^3, corresponding to 2.5 % of a Sr atom. Final positional and thermal parameters are listed in Table 7.2.

Table 7.2. Positional Parameters and Equivalent Isotropic Thermal Parameters for $Sr_2Sc_2B_4O_{11}$.

	x	*y*	*z*	B_{eq}
Sr	0.19241(5)	0.16409(4)	0.77598(6)	0.64(2)
Sc	0.2833(1)	0.64716(9)	0.8147(1)	0.45(3)
B1	0.6569(7)	0.1017(5)	0.6456(8)	0.6(2)
B2	0.2188(6)	0.3918(5)	0.2785(8)	0.6(1)
O1	0.7933(4)	0.1517(4)	0.5066(5)	0.8(1)
O2	0.0524(4)	0.2952(4)	0.1764(5)	0.9(1)
O3	0.6598(5)	0.1331(4)	0.9081(5)	0.9(1)
O4	0.2567(5)	0.4440(4)	0.5381(5)	0.9(1)
O5	0.3564(4)	0.4419(3)	0.1101(5)	0.7(1)
O6	½	0	½	1.8(2)

Structure

A labeled drawing of the contents of the unit cell of the compound $Sr_2Sc_2B_4O_{11}$ is shown in Figure 7.2, and a perspective view along the *c* axis is shown in Figure 7.3. The structure is built from mixed orthoborate, pyroborate layers, Figure 7.4, stacking along the direction [1 $\bar{1}$ 0] in the sequence ABCABC....; Sr and Sc atoms are interleaved between successive layers. The Sr atom occupies an 8-coordinate site resembling a highly distorted cube. The Sc atom occupies a distorted octahedron; two of these octahedra share an edge (O5···O5) across the borate layer to form a bioctahedral dimer (Figure 7.3). These dimers are separated and isolated along the *c* axis by intervening borate groups.

Selected interatomic distances and angles are listed in Table 7.3. Sr-O distances range from 2.519(3) to 2.807(3) Å with an average length of 2.64(11) Å that compares to the value 2.63 Å computed from crystal radii [19]. The Sc-O distances in the distorted octahedron range from 2.032(3) to 2.152(3) Å with an average distance of 2.11(5) Å that compares to the value 2.125 Å computed from crystal radii. The angles O5-Sc-O5, 88.1(1)°, and O1-Sc-O5, 99.3(1)°, demonstrate the extent of the distortion from an ideal octahedral geometry.

The triangular orthoborate group is normal with B-O

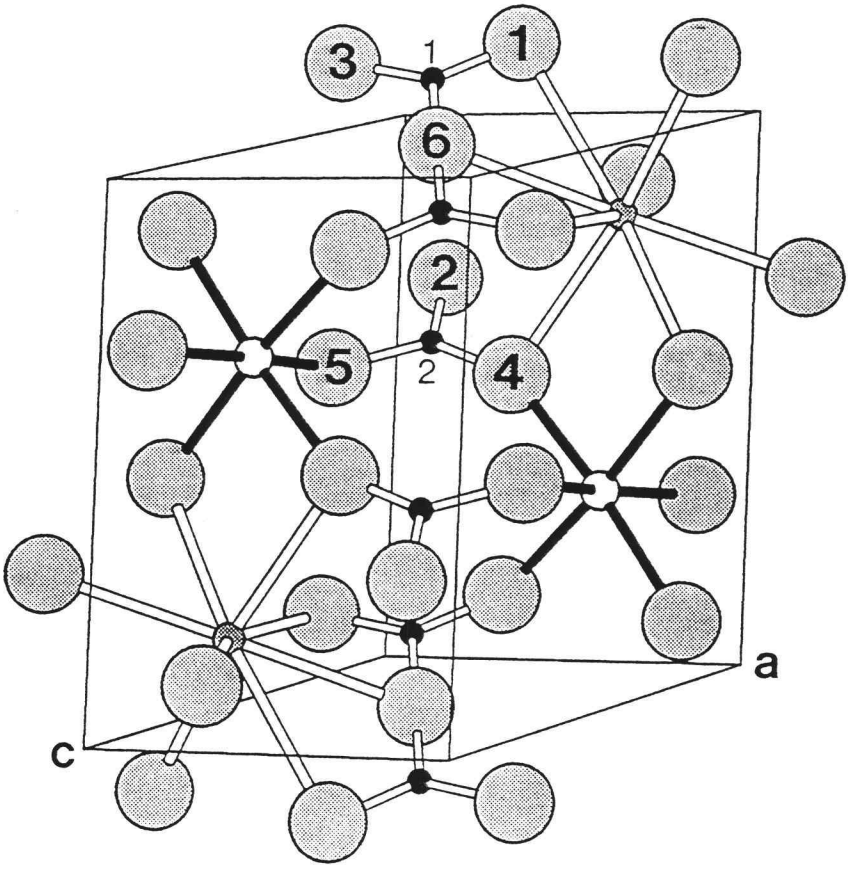

Figure 7.2. Labeled sketch of the contents of a unit cell of the compound $Sr_2Sc_2B_4O_{11}$. The small shaded circles represent Sr atoms, the open circles represent Sc atoms, the small filled circles represent B atoms, and the large shaded circles represent O atoms, here, and in ensuing figures.

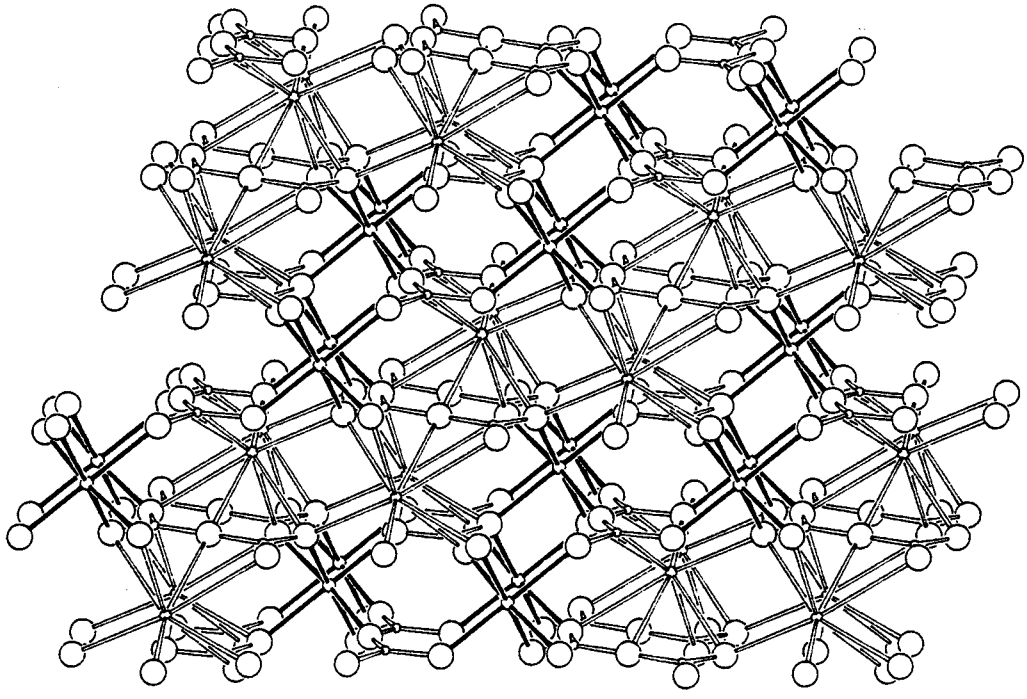

Figure 7.3. Perspective view of the structure of $Sr_2Sc_2B_4O_{11}$ along the *c* axis.

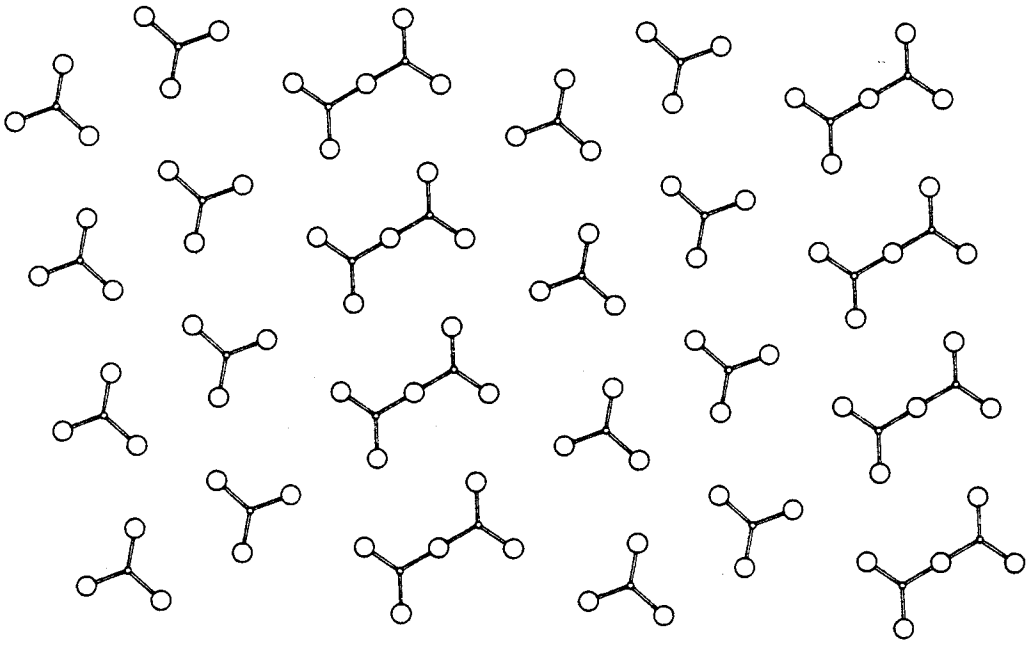

Figure 7.4. Diagram showing how orthoborate (BO_3^{3-}) and pyroborate ($B_2O_5^{4-}$) groups pack together in planes in the $Sr_2Sc_2B_4O_{11}$ structure.

Table 7.3. Selected Bond Distances (Å) and Angles (°) for $Sr_2Sc_2B_4O_{11}$.

Sr-O1	2.695(3)	O1-Sr-O6	50.79(6)
Sr-O1	2.557(3)	O3-Sr-O6	50.23(6)
Sr-O2	2.519(3)	O1-Sr-O3	93.89(8)
Sr-O3	2.807(3)	O1-Sr-O2	138.14(8)
Sr-O3	2.574(3)	O3-Sr-O5	63.37(8)
Sr-O4	2.536(3)	O3-Sr-O5	100.5(1)
Sr-O5	2.693(3)	O1-Sr-O1	71.2(1)
Sr-O6	2.743(1)	O5-Sr-O6	115.05(9)
Sc-O1	2.101(3)	O1-Sc-O2	89.8(1)
Sc-O2	2.079(3)	O1-Sc-O5	173.9(1)
Sc-O3	2.145(3)	O1-Sc-O5	99.3(1)
Sc-O4	2.032(3)	O2-Sc-O5	90.6(1)
Sc-O5	2.145(3)	O2-Sc-O4	96.0(1)
Sc-O5	2.152(3)	O2-Sc-O5	168.8(1)
B1-O1	1.346(5)	O1-B1-O3	127.1(3)
B1-O3	1.348(5)	O1-B1-O6	115.6(3)
B1-O6	1.411(4)	O3-B1-O6	117.3(3)
B2-O2	1.346(5)	O1-B1-O3	127.1(3)
B2-O4	1.345(5)	O2-B2-O5	117.7(3)
B2-O5	1.406(4)	O4-B2-O5	122.1(3)

distances ranging from 1.345(5) to 1.406(4) Å, and the largest angular distortion is exhibited by O2-B2-O4, 117.7(3)°. The pyroborate group, however, adopts an unusual geometry, exhibiting a planar orientation with a crystallographically imposed B-O-B angle of 180°. The B1-O6 distance involving the central O atom is longer than the B-O distances involving the terminal O atoms. The magnitude of the thermal parameter for the central O6 atom is consistent with the long nonbonded O6···O distances. The O6···O1 and O6···O3 distances, 2.332(3) and 2.356(3) Å, respectively, of the terminal BO_2 groups are comparable to the average O···O distance, 2.37(3) Å, within each BO_3 triangle. Outside the triangle the shortest O6···O distance is 3.240(3) Å (O6···O2) which contrasts to each of the other O atoms having five O···O interactions in the range 2.891(4) to 3.241(4) Å. With contacts to two Sr atoms and two B atoms the central atom O6 exhibits a distorted square-planar coordination; atoms O2 and O4 bind three cations, and the remaining O atoms are bound by four cations in distorted tetrahedral arrangements. By using the coordination geometries described above and the bond-valence method [20], we have found the valences of all atoms to be within 4% of their characteristic integral values.

Infrared Measurements

Infrared spectra for the phases $Sr_2Sc_2B_4O_{11}$ and $ScBO_3$ are shown in Figure 7.5. Powdered samples were examined as dispersions (2 wt%) in KBr pellets by using a Starlab Sirius 100 FTIR spectrometer (Mattson Instruments Inc.). The spectrum of $ScBO_3$ exhibits three symmetry-allowed bands with contributions from two B isotopes present in their natural abundance ($^{10}B/^{11}B$ = 18/82). These bands are the out-of-plane bending modes (ω_2) occurring at 763 and 740 cm^{-1}, the doubly degenerate antisymmetric stretch (ω_3) at 1265 and 1234 cm^{-1}, and the degenerate in-plane mode at 639 cm^{-1}. These values correspond to those reported in the literature [21]. Because the planar BO_3 group has D_3 symmetry in $ScBO_3$, the symmetric stretching mode (ω_1) is IR inactive whereas the BO_3 groups in the pyroborates have no imposed symmetry, making the modes active. This vibration has been observed near 950 cm^{-1} in other orthoborates, and is likely present in the spectra of the title compound. The remaining peaks in the spectra of the Sr compound arise from the fundamental modes of absorption of the pyrborate group. Assignment of the modes requires analyses of isotopically substituted samples; the data are presented here primarily for identification purposes.

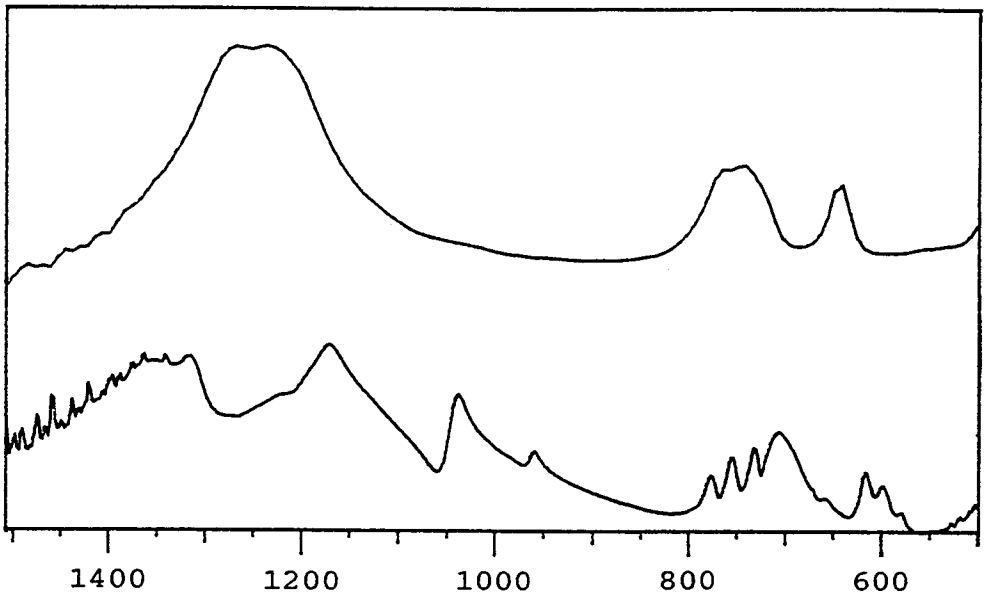

Figure 7.5. Infrared absorption spectra for $Sr_2Sc_2B_4O_{11}$ (bottom) and $ScBO_3$ (top).

Pyroborate Geometry

A broad distribution of B-O-B angles and torsion angles, τ_1 and τ_2, of the terminal BO_2 groups, Figure 7.1, have been observed for the pyroborate group; B-O-B and interplanar angles for all structurally characterized examples are listed in Table 7.4. The B-O-B angle is observed to vary from 125° to 180° while a nearly planar arrangement is maintained. In Figure 7.6 we have drawn selected conformations of the $B_2O_5^{4-}$ group that have been examined by the extended Hückel method [22]. The planar geometry at left with the angle B-O-B = 180° is observed in the mixed Sr orthoborate pyroborate, and the second geometry from left, also planar, exhibits the angle B-O-B = 120°; calculations were also performed on geometries with B-O-B angles = 110°, 140°, and 160°. In each calculation all B-O distances were fixed at 1.37 Å. The most stable geometry in this series corresponds to B-O-B=180° with a total energy = -787.9 eV. As the angle approaches 120° the magnitude of the total energy decreases only slightly. Below 120°, a steep rise in the energy occurs from increased O···O repulsive interactions. These repulsive interactions can be relieved by torsional motions about τ_1 and τ_2. The total energy for a planar unit with B-O-B = 110° is -786.3 eV compared with the energy of a group with the same B-O-B angle and an

Table 7.4. B-O-B and Interplanar Angles for Pyroborates.

Compound	S.G.	B-O-B angle	Interplanar angle	Ref.
$Sr_2Sc_2B_4O_{11}$	$P\bar{1}$	180°	0°	this work
$Sr_2ScLiB_4O_{10}$	$P2_1/n$	129.2°	1.6°	1
$Sr_2B_2O_5$	$P2_1/a$	140°	4.0°	2
$Sr_2ScLiB_4O_{10}$	$P2_1/n$	133.8°	8.9°	1
$Tl(NbO)B_2O_5$	$Pna2_1$	125.6°	10.6°	3
$Rb(NbO)B_2O_5$	Pn	116.5°	11.1°	4
$Rb(NbO)B_2O_5$	Pn	120.5°	11.8°	4
$Rb(NbO)B_2O_5$	Pn	127.0°	15.4°	4
$Rb(NbO)B_2O_5$	Pn	126.9°	15.7°	4
$Mg_2B_2O_5$	$P\bar{1}$	133.9°	16.1°	5
$Rb(NbO)B_2O_5$	Pn	127.7°	16.4°	4
$Co_2B_2O_5$	$P\bar{1}$	138.7°	18.8°	6
$Mg_2B_2O_5$	$P2_1/a$	138.0°	22.3°	7
$CaMgB_2O_5$	$Pca2_1$	123.3°	32.3°	8
$CaMgB_2O_5$	$P2_1/b$	122.0°	33.6°	9
$CaMgB_2O_5$	$Pca2_1$	124.1°	36.1°	8
$CaMnB_2O_5$	$P2_1/b$	120.1°	36.5°	10
$CaMgB_2O_5$	$Pca2_1$	115.6°	53.7°	8
$CaMgB_2O_5$	$Pca2_1$	118.1°	54.0°	8
$CaMgB_2O_5$	$P2_1/b$	119.5°	54.8°	9

Table 7.4. (cont'd)

$CaMgB_2O_5$	$Pca2_1$	113.4°	55.0°	8
$CaMgB_2O_5$	$Pca2_1$	118.0°	56.5°	8
$CaMnB_2O_5$	$P2_1/b$	111.8°	56.8°	10
$Na_4B_2O_5$	C2/c	120.2°	67.0°	11
$Ba_2Sc_2B_4O_{11}$	C2/c	112.1°	76.8°	27

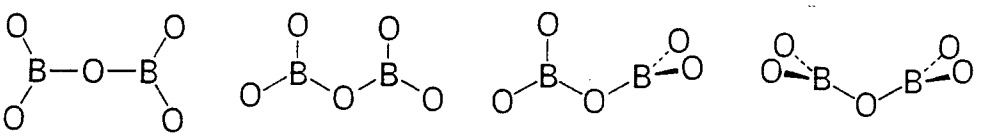

-787.9 eV *-787.3* *-787.4* *-787.4*

Figure 7.6. Diagram showing four different pyroborate conformations in which total energy changes only slightly.

interplanar angle of 45° that is -787.0 eV. The difference in energy arises from the repulsive interactions of the O lone pairs among the higher occupied orbitals. The smaller B-O-B angles are predominantly associated with the larger interplanar angles (Table 7.4). In silicates, as the Si-O-Si angle widens, the bridging Si-O interatomic distances shorten by a small amount. A similar trend in the experimental data on pyroborates is not observed, although such a trend would be anticipated from our Hückel results. Overlap populations for the B-O bonds in the planar arrangement range from $B\text{-}O_{bridge}$, 0.61, and $B\text{-}O_{terminal}$, 0.67, for B-O-B = 110° to $B\text{-}O_{bridge}$, 0.66, and $B\text{-}O_{terminal}$, 0.65, for B-O-B = 180°. For larger B-O-B angles, a greater overlap between B(p)-O(p) orbitals increases the population that is commonly associated with a shorter bond length. Of course, this treatment neglects the nature and interactions of additional cations associated with the bridging O atom.

Values in Table 7.4 also indicate a relatively smooth variation of interplanar angle from 0° to 76.8°. From consideration of charge distributions in simple electron-dot diagrams (Figure 7.7), the extent of π-electron delocalization through the central O atom is expected to be minimal because of the formal positive charge on the central O atom of the hybrid at the far right of Figure 7.7. With little π-electron density delocalized through

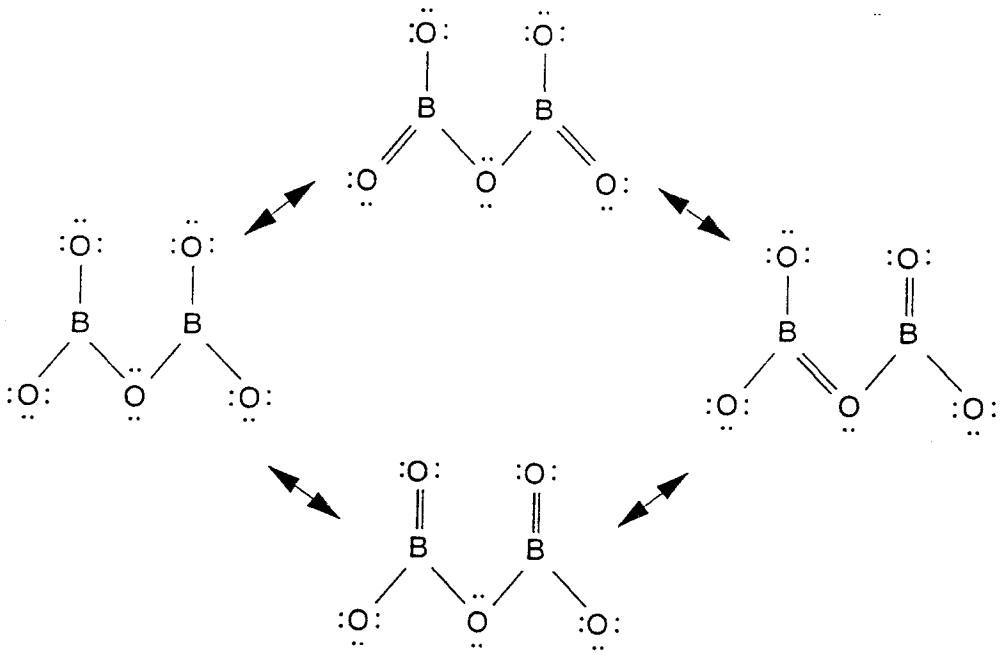

Figure 7.7. Electron-dot diagrams showing four different resonance structures possible for the pyroborate group.

the central O atom, no significant barriers to rotations about τ_1 or τ_2 are anticipated. This expectation is borne out by the results of calculations on the third and fourth groups from left depicted in Figure 7.6. The third geometry represents a rotation of the terminal BO_2 group by 90° about τ_2, and the fourth geometry is produced by an additional rotation of 90° about τ_1. Calculations were also performed on geometries produced by incremental changes in τ_1 and τ_2 of 10°, and no significant energetic differences or barriers were noted for any of the intermediate geometries. These results are consistent with those listed in Table 7.4 as well as the molecular structure of the isoelectronic species N_2O_5 [23] which has been modeled as a dynamic rotor with τ_1 and $\tau_2 \approx 30°$. Hence, in solids where the coordination and bonding requirements of all atoms must be simultaneously satisfied, a variety of geometries for the pyroborate group are observed.

Significance of Pyroborate Geometry

The geometry of the pyroborate group is important and relevant to the continued development of borates similar to LiB_3O_5 (LBO) [24] as nonlinear optical materials. The frequency converter LBO exhibits a threshold for second harmonic generation that is 100 times smaller than that of

KDP (potassium dihydrogen phosphate) with an optical damage threshold near 25 GW/cm^2 with a 100 ps laser pulse. The polyborate anion in the structure has commonly been described as a fusion of B_3O_7 rings built from two B atoms in triangular coordination and one in tetrahedral coordination. An alternative description that emphasizes the principal chromophore in the structure is to consider the material to be a pyroborate with the pyroborate groups linked by tetrahedrally coordinated B atoms, Figure 7.8. Because the pyroborate groups do not pack in distinct layers as in the materials $Sr_2Sc_2B_4O_{11}$, BaB_2O_4, and many other borates, the magnitude of the birefringence is relatively small. This feature coupled with a suitable constructive summation of microscopic hyperpolarizability coefficients affords a useful material with characteristics of small threshold for conversion and a relative angular insensitivity to phasematching.

The largest microscopic hyperpolarizability coefficients associated with LBO derive from the pyroborate section of the borate matrix. These groups are not optimally aligned in the material to afford the highest possible nonlinearity. Hence, the synthesis of new *acentric* pyroborates could well afford nonlinearities higher than that of LBO. The higher nonlinearities should be observed in those materials crystallizing in layered structures having nearly planar groups identically

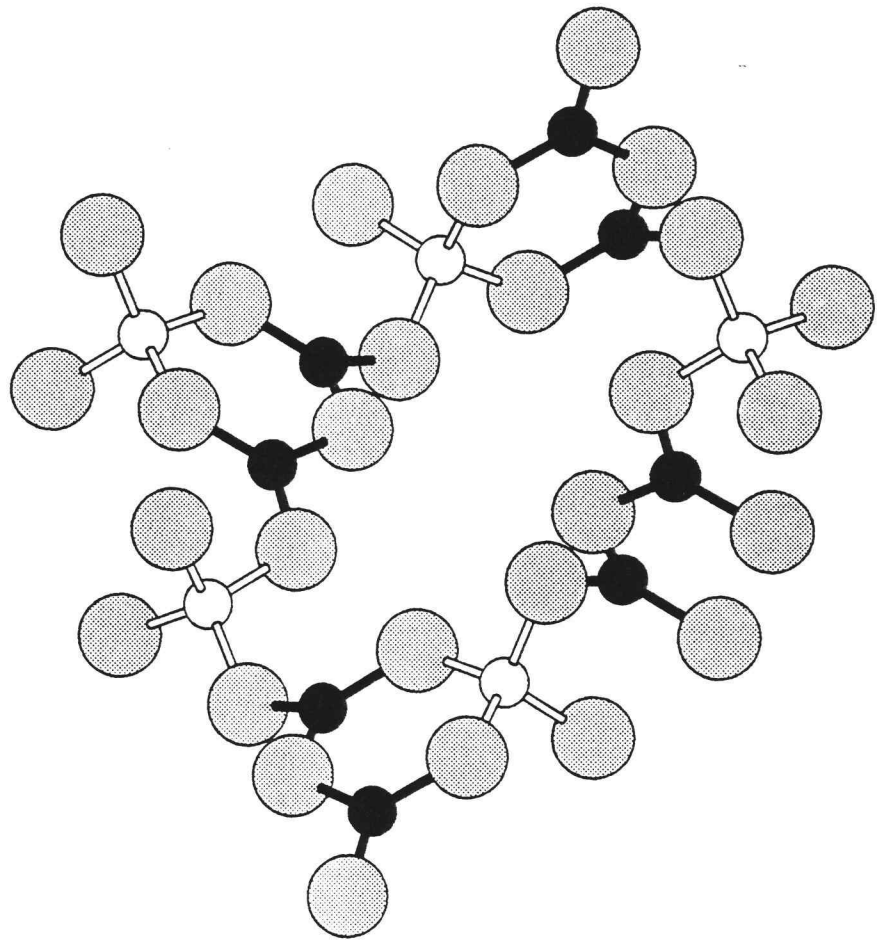

Figure 7.8. The polyborate anion in the nonlinear optical material LiB_3O_5.

oriented. These materials should also be highly birefringent, exhibiting many of the characteristics of the converter BaB_2O_4 [22,26]. The layered nature of a pyroborate structure can be disrupted by the coordination requirements of the associated cations as in the case of LBO or by the changeable nature of the interplanar angle. Where intermediate angles are encountered (~30-60°) in acentric samples, layered-type packings should be unfavored, and lower birefringence should be observed, likely with an intermediate nonlinearity.

Acknowledgments

This work was funded by the US National Science Foundation, Solid-State Chemistry Program. JH was supported under subcontract B07620 administered by Lawrence Livermore National Laboratory. DAK is grateful to the Alfred P. Sloan Foundation for a fellowship, 1989-1991.

References

[1] P.D. Thompson and D.A. Keszler, Solid State Ionics **32/33**, 521 (1989).

[2] H. Bartl and W. Schuckmann, Neues Jahrb. Min. Monatsh. **8**, 253 (1966).

[3] M. Gasperin, Acta Crystallogr. **B 30**, 1181 (1974).

[4] P.A. Baucher, M. Gasperin, and B. Cervelle, Acta Crystallogr.**B 32**, 2211 (1976).

[5] S. Block, G. Burley, A. Perloff, and R.D. Mason, J. Res. Nat. Bur. Stand. **62**, 95 (1959).

[6] S. Berger, Acta Chem. Scand. **4**, 1054 (1950).

[7] Y. Takéuchi, Acta Crystallogr. **5**, 574 (1952).

[8] O.V. Yakubovich, M.A. Simonov, E.L. Belokoneva, Yu.K. Egorov-Tismenko, and N.V. Belov, Dokl. Akad. Nauk SSSR **230**, 837 (1976).

[9] O.V. Yakubovich, N.A. Yamnova, B.M. Shchedrin, M.A. Simonov, and N.V. Belov, Dokl. Akad. Nauk SSSR **228**, 842 (1976).

[10] O.V. Yakubovich, M.A. Simonov, and N.V. Belov, Dokl. Akad. Nauk SSSR **238**, 98 (1978).

[11] H. König, R. Hoppe, and M. Jansen, Z. Anorg. Allg. Chem. **449**, 91 (1979).

[12] K. Machida, G. Adachi, and J. Shiokawa, Acta Crystallogr. **B 35**, 145 (1979).

[13] Yu.N. Il'in, V.V. Kravchenko, and K.I. Petrov, Russ. J. Inorg. Chem. **28**, 909 (1983/84).

[14] U.L. Schäfer, Neues Jahrb. Min. Monatsh. 75 (1980).

[15] P.D. Thompson and D.A. Keszler, Chem. Mater. **1**, 292 (1989).

[16] K. Yvon, W. Jeitschko, and E. Parthe, J. Appl. Cryst. **10**, 73 (1977).

[17] TEXSAN: Single Crystal Structure Analysis Software, Version 5.0, (1989). Molecular Structure Corporation, The Woodlands, TX 77381.

[18] D. Stuart and N. Walker, Acta Crystallogr. **B 39**, 158 (1983).

[19] R.D. Shannon, Acta Crystallogr. **A 32**, 751 (1976).

[20] I.D. Brown in "Structure and Bonding in Crystals," **Vol. II**, ed. M. O'Keeffe and A. Navrotsky, Academic Press: New York, p. 1, (1981).

[21] W.C. Steele and J.C. Decius, J. Chem. Phys. **25**, 1184 (1956).

[22] Chen, B. Wu, A. Jiang, and G. You, Sci. Sin. Ser. **B 28**, 235 (1985).

[23] B.W. Mcclelland, L. Hedberg, K. Hedberg, and K. Hagen, J. Am. Chem. Soc. **105**, 3789 (1983).

[24] C. Chen, Y. Wu, A. Jiang, B. We, G. You, R. Li, and S. Lin, J. Opt. Soc. Am. **B 28**, 235 (1985).

[26] D. Eimerl, L. Davis, S. Velsko, E. K. Graham, and A. Zalkin, J. Appl. Phys. **62**, 1968 (1987).

[27] P.D. Thompson, J. Huang, R.W. Smith, and D.A. Keszler, J. Solid State Chem., in press.

CHAPTER 8

THE PYROBORATE $Sr_2ScLiB_4O_{10}$, A NEW STRUCTURAL TYPE

Paul D. Thompson and Douglas A. Keszler*

Department of Chemistry and
Center for Advanced Materials Research
Oregon State University
Gilbert Hall 153
Corvallis, Oregon 97331-4003

Solid State Ionics **32/33**, 521 (1989)

Abstract

A new pyroborate $Sr_2ScLiB_4O_{10}$ has been synthesized and structurally characterized by single-crystal X-ray diffraction methods. It crystallizes with four formula units in a cell of dimensions a = 12.543(1), b = 5.2201(6), c = 13.625(2) Å, and ß = 116.69(1)°. The structure is a new type having layers of pyroborate groups with the associated cations residing in interlayer interstices. The Sr atoms occupy sites in sevenfold coordination and the Sc atom occupies a distorted octahedron. Five-coordinate Li atoms reside in oblong tunnels extending along the direction [010].

Introduction

Certain features such as weak crystal fields [1], large polarizabilities, high transparencies [2], high optical damage thresholds [3-6], and attractive thermal shock characteristics [2] make solid-state borates of technological interest for a variety of optical applications. These features are manifest in the tunable laser material $Cr^{3+}:ScBO_3$ [7] and the nonlinear optical converter BaB_2O_4 [2]. As part of our general program in the synthesis and characterization of borates and other new materials that may serve as hosts for the laser-active ions Ti^{3+} and Cr^{3+}, we have investigated a number of borate systems containing the ion Sc^{3+}. During attempts to grow crystals of a new, simpler strontium scandium borate from a flux containing $LiBO_2$, we isolated single crystals of the title compound, a new and structurally unique pyroborate. The preparation and crystal structure of this material are described herein.

Experimental

Clear, colorless lathe-shaped crystals were grown from a flux corresponding to the composition 25 mol% SrO, 12.5 mol% Sc_2O_3, 25 mol% Li_2O, and 37.5 mol% B_2O_3. The reagents $Sr(NO_3)_2$ powder, reagent grade, AESAR; $Sc_2(C_2O_4)_3 \cdot 4H_2O$ powder, 99.9%, ALFA; $LiNO_3$ powder, 99.9%, ALFA; and B_2O_3 powder, 99.99%, ALFA were ground under hexane and subsequently heated at 773 K for 8 hours. The mixture was cooled, ground under hexane, pressed into a pellet, and heated to 1273 K at 3 K/min. The sample was soaked for 2 hours at this temperature, then cooled at 6 K/hour to 773 K. The crystals were isolated by dissoulution of the excess $LiBO_2$ in boiling H_2O.

A homogeneous powder of the compound was prepared by pressing a stoichiometric mixture of the aforementioned reagents into a pellet and heating it at 923 K for 30 minutes. The resulting powder was reground, pressed into a pellet, and heated at 1123 K for 8 hours. The powder X-ray diffraction pattern of this sample compares to that calculated from the results of the single-crystal structural determination.

X-ray Structural Work

Details of the data collection, reduction, and refinement are summarized in Table 8.1. The lattice constants were determined by a least-squares analysis of the angle settings of 21 reflections in the range $37° \leq 2\theta(\text{MoK}\alpha) \leq 45°$ that had been automatically centered on a Rigaku AFC6R diffractometer. Intensity data were collected with the ω-2θ scan technique. The intensities of three standard reflections, measured every 199 reflections throughout data collection, exhibited excursions of less than 2.1%.

The structure was solved and refined with the use of computer programs from the TEXRAY crystallographic software package [8]. The positions of the Sr atoms were determined from direct methods. The atoms Sc, B, and O were located from ensuing electron density syntheses. A difference electron density map with these atoms in place afforded several peaks of similar height. Analysis of a drawing of the unit cell with these peaks located afforded the position of the Li atom; the position was verified by successful refinement and the resultant chemically reasonable internuclear separations.

The final cycles of refinement following application of an absorption correction with the program DIFABS [9] were performed on F_o for $F_o^2 \geq 3\sigma(F_o^2)$ and were based on

Table 8.1. Crystal Data and Intensity Collection for $Sr_2ScLiB_4O_{10}$.

Empirical Formula	$Sr_2ScLiB_4O_{10}$
Formula Weight	430.37
a, Å	12.543(1)
b, Å	5.2201(6)
c, Å	13.365(2)
ß, deg.	116.69(1)
V, $Å^3$	798
Z	4
Space Group	$P2_1/n$ (#14)
μ (Mo Kα), cm^{-1}	148.41
Diffractometer	Rigaku AFC6R
Radiation	Mo Kα (λ=0.71069 Å) Graphite-monochromated
Temperature	23°C
λ^{-1} sin θ, limits, $Å^{-1}$	0.049 - 0.859
Data Collected	$-21 \leq h \leq 18$, $0 \leq k \leq 8$, $0 \leq l \leq 22$
Scan speed, deg min^{-1}	32.0 in 2θ
No. unique data with $F_o^2 > 3\sigma(F_o^2)$	2407
R (on F for $F_o^2 > 3\sigma(F_o^2)$	0.041
R_w (on F for $F_o^2 > 3\sigma(F_o^2)$	0.047
Error in observation of unit wt, e^2	0.99

2407 unique observations with 163 variables. The final values of the conventional indices R and R_w on F for these reflections are 0.041 and 0.047, respectively. The final difference electron density map contains no features greater than 0.5% of a Sr atom. Analysis of F_o vs F_c as a function of F_o, $\lambda^{-1}\sin\theta$, and Miller indices reveals no unusual trends.

Final atomic parameters and equivalent isotropic thermal parameters appear in Table 8.2. Atomic displacement coefficients appear in Table 8.3 and structure amplitudes are given in reference [10].

Table 8.2. Positional Parameters and Equivalent Isotropic Thermal Parameters for $Sr_2ScLiB_4O_{10}$

atom	x	y	z	B(eq)[a]
Sr(1)	0.68261(4)	0.3808(1)	0.35128(4)	0.65(1)
Sr(2)	0.65190(4)	0.43554(9)	0.62253(4)	0.56(1)
Sc	0.63442(8)	0.4293(2)	0.88182(7)	0.40(2)
Li	0.1204(9)	0.106(2)	0.6002(8)	1.1(3)
B(1)	0.9147(5)	0.440(1)	0.7721(4)	0.5(1)
B(2)	0.6020(5)	0.859(1)	0.2078(4)	0.7(1)
B(3)	0.5922(5)	-0.108(1)	0.4498(4)	0.6(1)
B(4)	0.9237(5)	0.419(1)	0.5519(4)	0.6(1)
O(1)	0.6440(3)	0.1618(6)	0.7697(3)	0.6(1)
O(2)	0.8850(3)	0.1829(6)	0.5064(3)	0.6(1)
O(3)	0.6815(3)	-0.0004(8)	0.5397(3)	1.1(1)
O(4)	0.5487(3)	0.6264(7)	0.1860(3)	0.6(1)
O(5)	0.5677(3)	0.6410(7)	0.4381(3)	0.7(1)
O(6)	0.8525(3)	0.6285(7)	0.5135(3)	0.7(1)
O(7)	0.5227(3)	0.0741(7)	0.3687(3)	0.8(1)
O(8)	0.5388(3)	0.0727(6)	0.1411(3)	0.7(1)
O(9)	0.8667(3)	0.2120(7)	0.7261(3)	0.7(1)
O(10)	0.7124(3)	-0.0937(7)	0.2870(3)	0.9(1)

[a] $B_{eq} = (8\pi^2/3)\Sigma_i\Sigma_j U_{ij} a^*_i a^*_j \mathbf{a}_i \cdot \mathbf{a}_j$

Table 8.3. Atomic displacement coefficients for $Sr_2ScLiB_4O_{10}$.

ATOM	U11	U22	U33	U12	U13	U23
Sr(1)	0.0080(2)	0.0084(2)	0.0084(2)	0.0009(2)	0.0038(1)	-0.0001(2)
Sr(2)	0.0070(2)	0.0075(2)	0.0065(2)	-0.0001(1)	0.0029(1)	0.0005(1)
Sc(1)	0.0054(3)	0.0040(3)	0.0062(3)	-0.0003(3)	0.0028(3)	0.0002(3)
Li(1)	0.012(4)	0.009(4)	0.017(4)	0.005(3)	0.004(3)	0.006(3)
B(1)	0.008(2)	0.006(2)	0.007(2)	0.004(2)	0.004(2)	0.003(2)
B(2)	0.014(2)	0.007(2)	0.006(2)	0.000(2)	0.007(2)	0.001(2)
B(3)	0.010(2)	0.008(2)	0.006(2)	0.002(2)	0.003(2)	-0.000(2)
B(4)	0.010(2)	0.003(2)	0.011(2)	-0.002(2)	0.006(2)	-0.001(2)
O(1)	0.010(2)	0.007(1)	0.005(1)	0.001(1)	0.004(1)	-0.002(1)
O(2)	0.014(2)	0.004(1)	0.008(1)	-0.002(1)	0.006(1)	-0.001(1)
O(3)	0.007(2)	0.015(2)	0.013(2)	0.003(1)	-0.001(1)	-0.004(1)
O(4)	0.006(1)	0.006(1)	0.009(1)	0.001(1)	0.003(1)	0.002(1)
O(5)	0.013(2)	0.008(1)	0.008(1)	0.000(1)	0.006(1)	-0.000(1)
O(6)	0.010(2)	0.011(2)	0.008(1)	0.002(1)	0.004(1)	-0.001(1)
O(7)	0.011(2)	0.007(1)	0.008(1)	-0.001(1)	0.001(1)	0.005(1)
O(8)	0.008(1)	0.006(1)	0.010(1)	0.001(1)	0.002(1)	0.000(1)
O(9)	0.009(2)	0.006(1)	0.010(2)	-0.002(1)	0.004(1)	-0.003(1)
O(10)	0.007(1)	0.013(2)	0.011(2)	0.000(1)	0.000(1)	-0.001(1)

Results

A drawing of the unit cell with the labeling scheme appears in Figure 8.1. Selected bond distances and bond angles are given in Table 8.4. The structure may be described as a new laminar type with cations residing in sites between layers of pyroborate groups, $B_2O_5^{4-}$, that are approximately coplanar to (101). This description of the structure is best appreciated by inspection of the perspective view of Figure 8.2.

Two crystallographically independent pyroborate groups, Figures 8.3 and 8.4, are present in the structure. Each layer of the structure is formed from one type of pyroborate group; there is no integration of these groups in a given layer (cf. Figures 8.1 and 8.2). The B-O bond lengths 1.342(7) Å - 1.432(7) Å are similar to those observed in other structures where B atoms are triangularly coordinated by O atoms [11]. The B-O distances involving terminal O atoms (mean = 1.353(3) Å) are consistently shorter than those involving the bridging O atoms (mean = 1.42 Å). The bridging B(1)-O(7)-B(3) angle, 133.8(4)°, is slightly greater than the corresponding B(2)-O(8)-B(4) angle, 129.2(4)°; these angles compare to those reported in the compounds $Mg_2B_2O_5$, 131.5° [12-13], $Sr_2B_2O_5$, 139° [14], and $CaMgB_2O_5$, 122 - 127.7° [15].

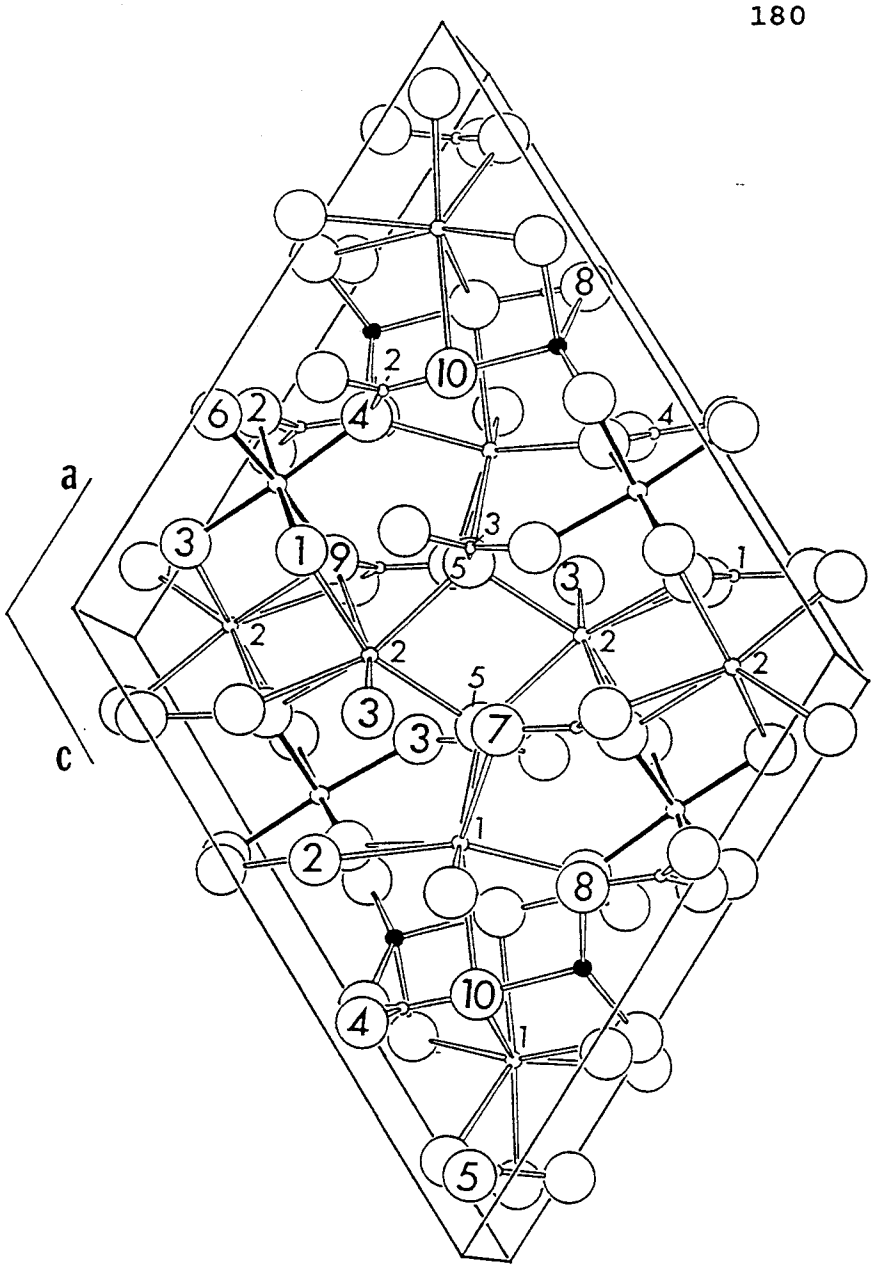

Figure 8.1. Drawing of the unit cell of $Sr_2ScLiB_4O_{10}$ with the atoms labeled. The largest circles represent O atoms, the smallest circles B atoms, the filled circles Li atoms, and the open circles with shaded bonds Sc atoms, here, and in the succeeding figures.

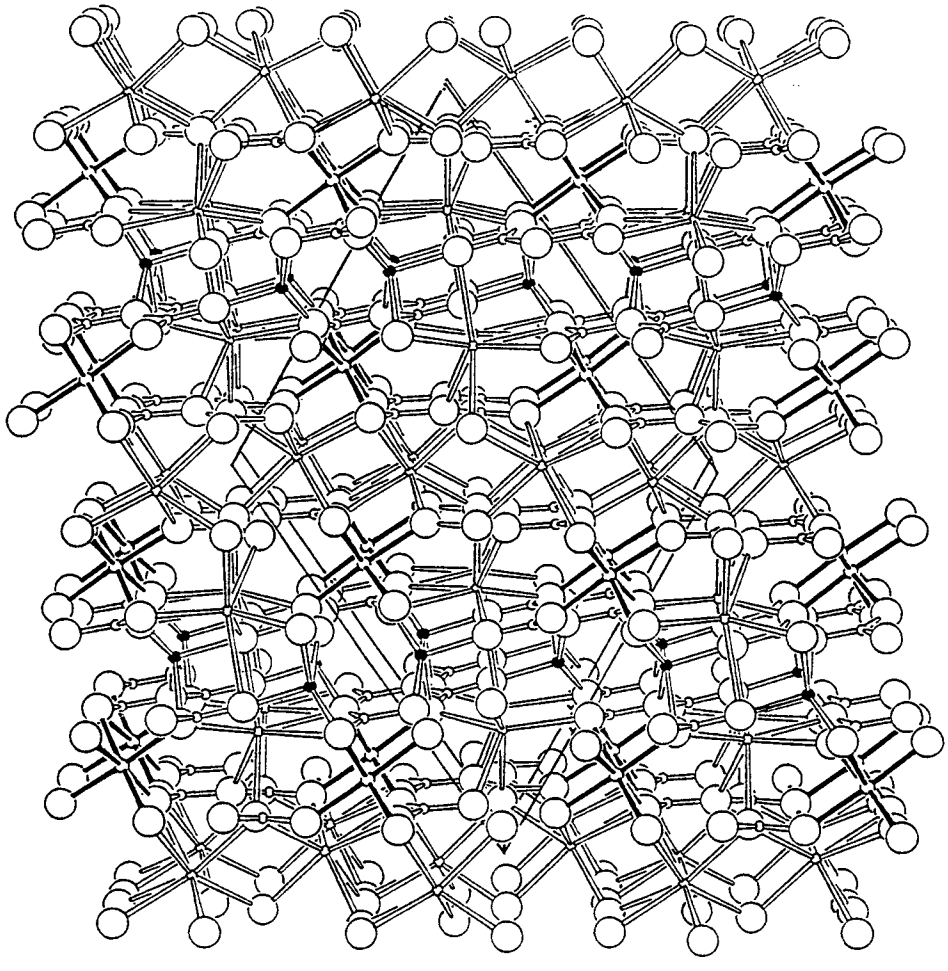

Figure 8.2. Perspective view of the structure of $Sr_2ScLiB_4O_{10}$ along the direction [010].

Table 8.4. Selected Interatomic Distances (Å) and Angles (°) for $Sr_2ScLiB_4O_{10}$.

Sr(1)-O(4)	2.478(3)	Li-O(10)	1.97(1)
Sr(1)-O(5)	2.618(4)	Li-O(2)	2.07(1)
Sr(1)-O(6)	2.621(4)	Li-O(4)	2.14(1)
Sr(1)-O(7)	2.659(4)	Li-O(8)	2.16(1)
Sr(1)-O(2)	2.677(4)	Li-O(6)	2.22(1)
Sr(1)-O(10)	2.709(4)	Li-O(2)	2.67(1)
Sr(1)-O(10)	2.745(4)		
		B(1)-O(9)	1.353(6)
Sr(2)-O(5)	2.491(4)	B(1)-O(1)	1.355(6)
Sr(2)-O(1)	2.501(4)	B(1)-O(7)	1.404(6)
Sr(2)-O(5)	2.527(4)		
Sr(2)-O(1)	2.594(4)		
Sr(2)-O(9)	2.613(4)	B(2)-O(10)	1.342(7)
Sr(2)-O(3)	2.640(4)	B(2)-O(4)	1.354(7)
Sr(2)-O(9)	2.682(4)	B(2)-O(8)	1.432(7)
Sc-O(4)	2.076(4)	B(3)-O(5)	1.340(7)
Sc-O(6)	2.078(4)	B(3)-O(3)	1.356(7)
Sc-O(9)	2.080(4)	B(3)-O(7)	1.420(6)
Sc-O(10)	2.096(4)		
Sc-O(11)	2.114(3)	B(4)-O(6)	1.359(6)
Sc-O(12)	2.114(4)	B(4)-O(2)	1.368(6)
		B(4)-O(8)	1.410(6)
O(4)-Sr(1)-O(5)	81.8(1)	O(5)-Sr(2)-O(5)	80.4(1)
O(4)-Sr(1)-O(6)	118.3(1)	O(5)-Sr(2)-O(9)	114.3(1)
O(4)-Sr(1)-O(7)	99.3(1)	O(5)-Sr(2)-O(3)	90.9(1)
O(4)-Sr(1)-O(2)	158.9(1)	O(5)-Sr(2)-O(9)	126.1(1)
O(4)-Sr(1)-O(10)	71.9(1)	O(1)-Sr(2)-O(5)	75.0(1)
O(5)-Sr(1)-O(6)	76.5(1)	O(1)-Sr(2)-O(3)	85.1(1)
O(5)-Sr(1)-O(7)	71.4(1)	O(1)-Sr(2)-O(9)	73.8(1)
O(5)-Sr(1)-O(10)	143.6(1)	O(5)-Sr(2)-O(9)	82.8(1)
O(5)-Sr(1)-O(10)	144.7(1)	O(1)-Sr(2)-O(9)	73.5(1)
O(6)-Sr(1)-O(2)	53.2(1)	O(1)-Sr(2)-O(3)	110.0(1)
O(4)-Sc-O(6)	86.0(1)	O(4)-Li-O(10)	96.7(4)
O(3)-Sc-O(4)	175.7(2)	O(8)-Li-O(10)	106.6(5)
O(2)-Sc-O(4)	86.9(1)	O(6)-Li-O(10)	97.1(4)
O(6)-Sc-O(9)	174.5(2)	O(4)-Li-O(8)	86.3(4)
O(3)-Sc-O(6)	93.0(1)	O(4)-Li-O(6)	165.8(5)
O(1)-Sc-O(3)	94.4(2)	O(6)-Li-O(8)	86.2(4)
O(1)-Sc-O(2)	176.2(1)		

Table 8.4. cont'd

O(9)-B(1)-O(1)	120.8(4)	O(5)-B(3)-O(3)	124.3(5)
O(9)-B(1)-O(7)	115.5(4)	O(5)-B(3)-O(7)	122.2(4)
O(1)-B(1)-O(7)	123.5(4)	O(3)-B(3)-O(7)	113.4(4)
O(4)-B(2)-O(10)	124.7(5)	O(2)-B(4)-O(6)	120.8(5)
O(8)-B(2)-O(10)	116.5(5)	O(6)-B(4)-O(8)	123.3(4)
O(4)-B(2)-O(8)	118.8(4)	O(2)-B(4)-O(8)	115.8(4)

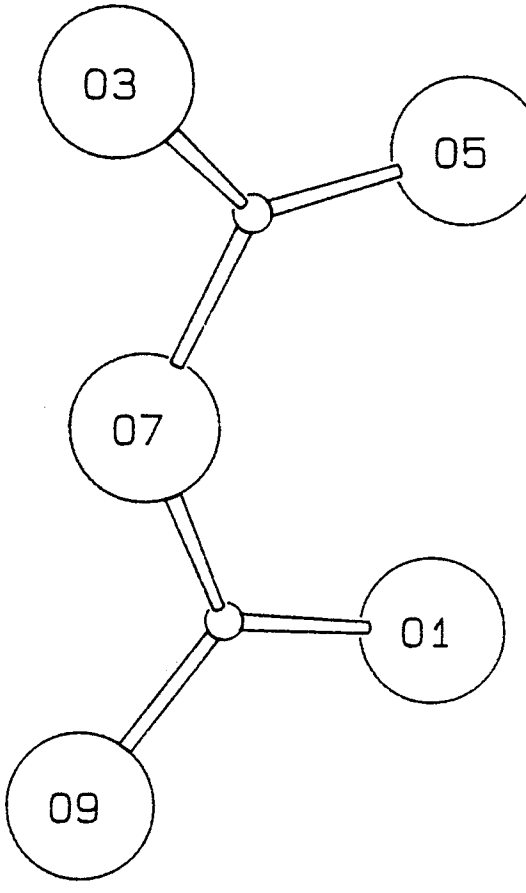

Figure 8.3. Pyroborate group with B(1)-O(7)-B(3) angle = 133.8(4)° and interplanar angle = 8.9(1)°.

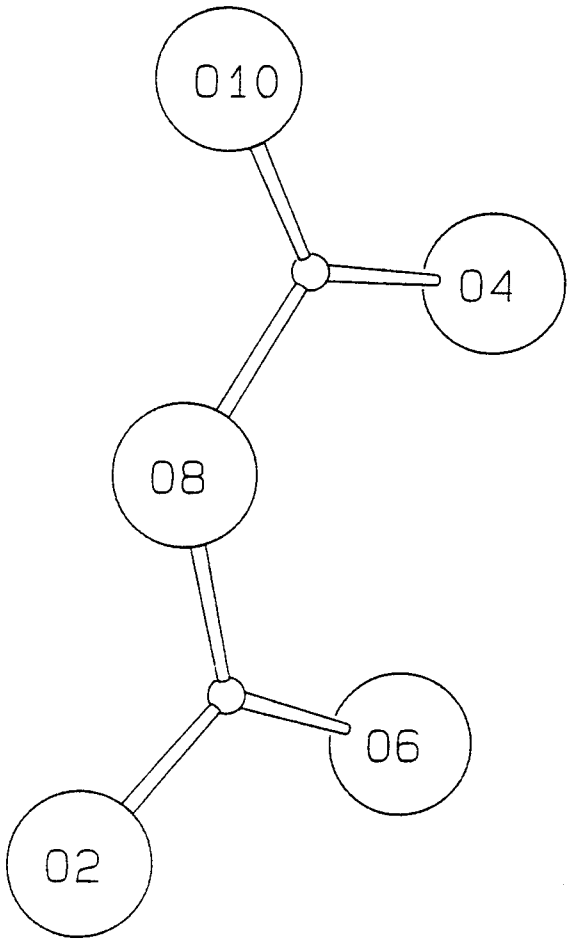

Figure 8.4. Pyroborate group with B(2)-O(8)-B(4) angle = 129.2(4)° and interplanar angle = 1.6(1)°.

Each Sr atom occupies an irregular heptacoordinate site, Figures 8.5 and 8.6. The bond distances and angles do not clearly define the type of coordination polyhedron about the atom Sr(2). Because four of the coordinated O atoms are present in one layer of pyroborate groups and three others in an adjacent layer we prefer the description tetragonal base-trigonal base [16]. The coordination polyhedron of the atom Sr(1) is also not clearly defined by the bond distances and angles although it may be viewed as an irregular capped trigonal prism. It is common for the Sr atom to exhibit large and irregular coordination environments in borates. Its coordination number is nine in the compounds SrB_2O_4 [17] and $SrNaBO_3$ [18], seven in the compound $Sr_2CuB_2O_6$ [19] where the range of Sr-O distances 2.514(4) - 2.676(4) Å is similar to the present compound, and six in the dolomite $SrZrB_2O_6$ [20].

The Li atom coordinates to five O neighbors located at the vertices of a distorted square pyramid, Figure 8.7. Consideration of the long Li-O(2) interaction, 2.67(1) Å, as an additional bonding interaction would complete a distorted octahedral coordination. The polyhedra centered by atom Sr(1) share vertices across the laminar space occupied by the Li atoms (Figure 8.2), resulting in the formation of oblong tunnels that extend along the direction [010]; two Li atoms per unit cell translation

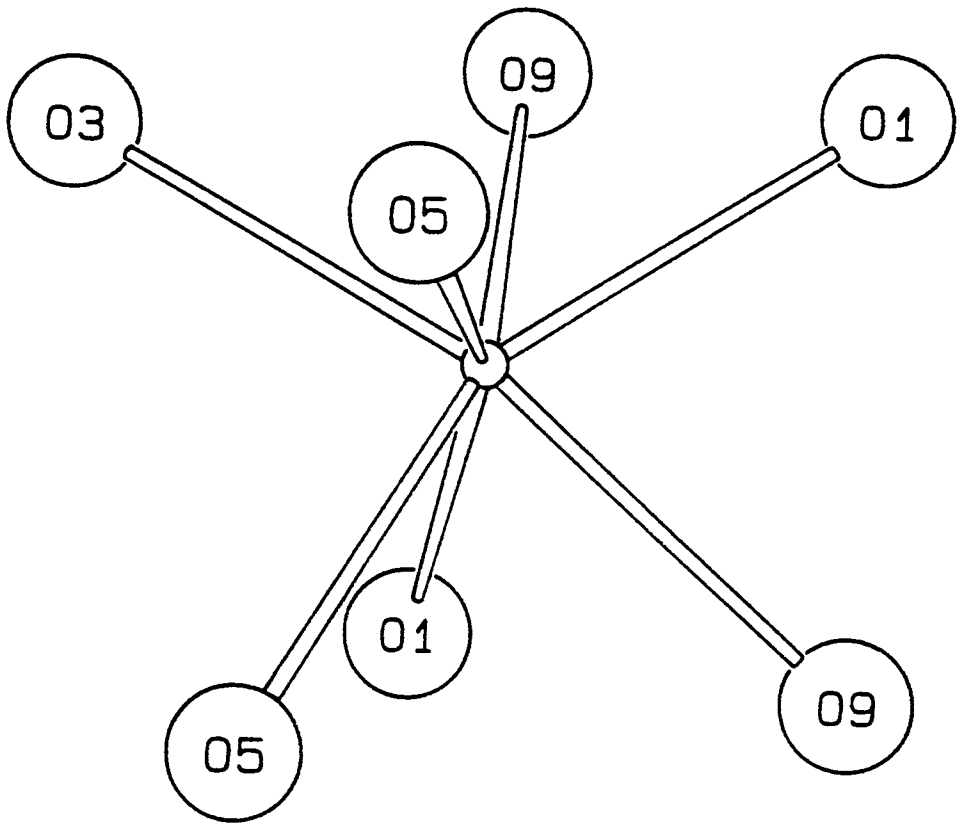

Figure 8.5. Sr(2) polyhedron with tetragonal base-trigonal base coordination.

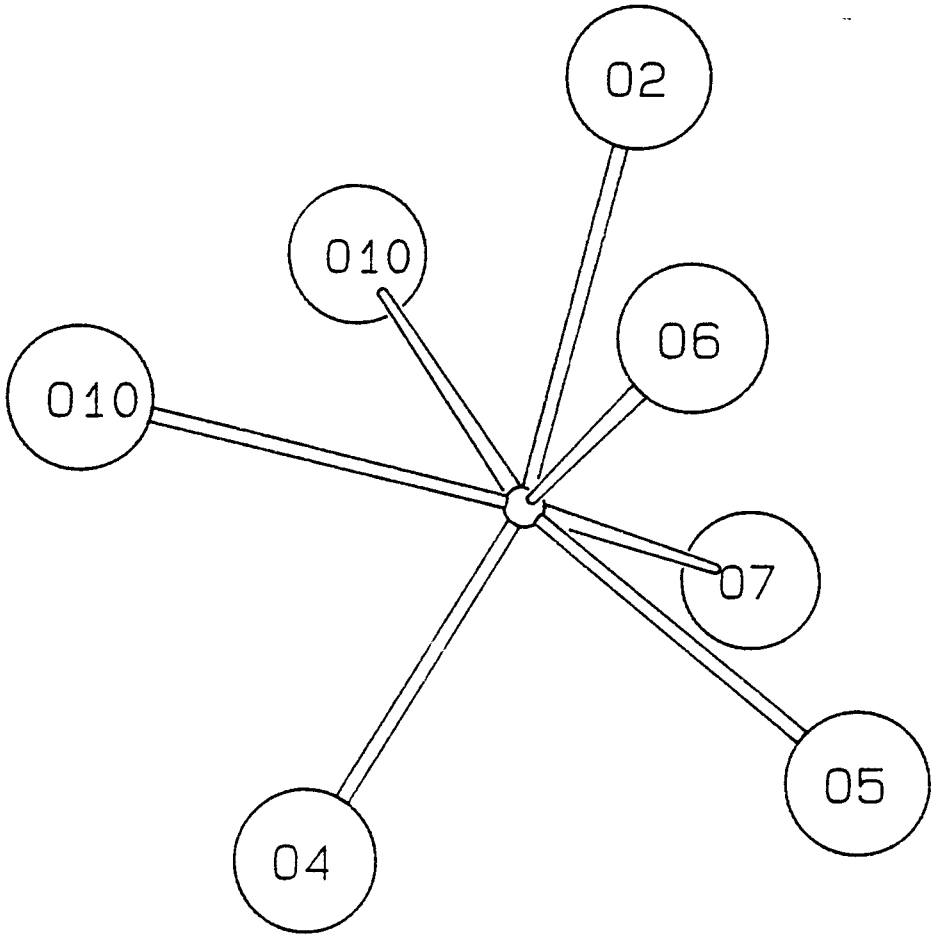

Figure 8.6. Sr(1) polyhedron with irregular capped trigonal prismatic coordination.

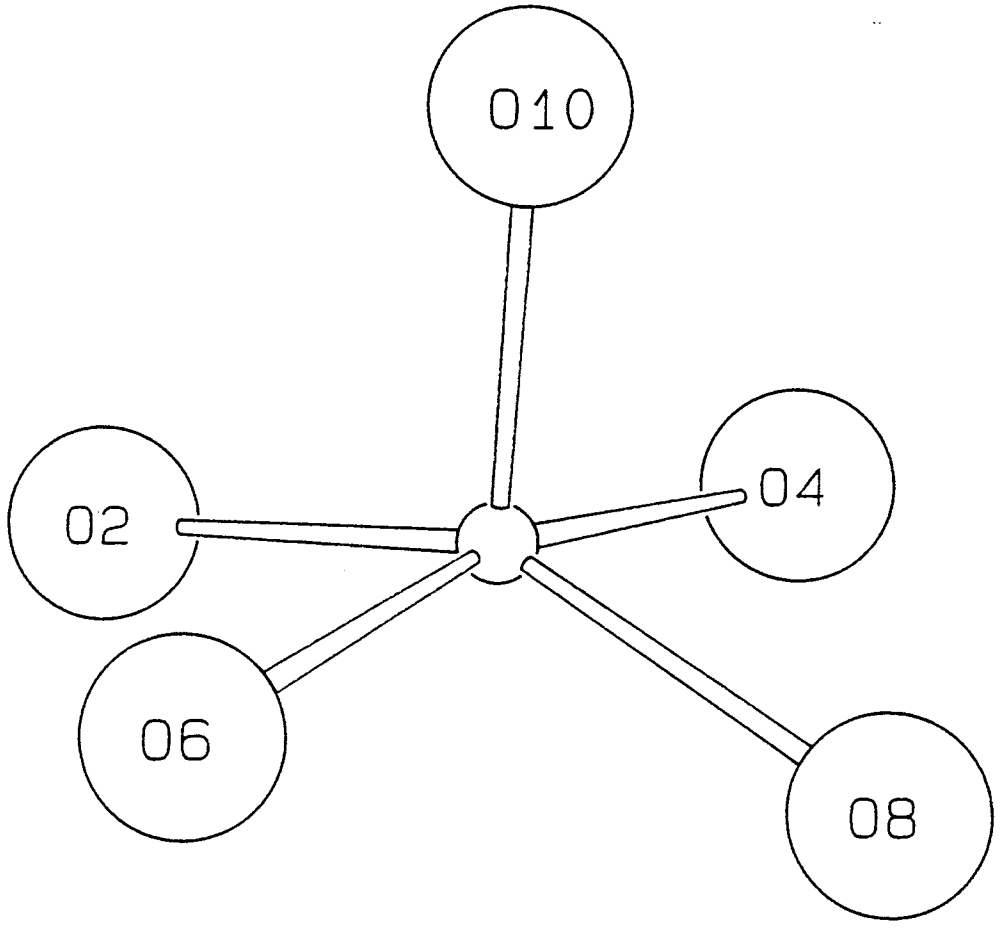

Figure 8.7. Five-coordinate Li in distorted square pyramid.

along the b axis are present in each tunnel.

The Sc atom resides in a distorted octahedral environment, Figure 8.8, with bond distances ranging from 2.076(4)-2.114(4) Å and angular distortions from an orthogonal octahedron that include O(4)-Sc-O(9), 97.5(1)°, O(3)-Sc-O(9), 83.8(1)°, and O(3)-Sc-O(6), 93.0(1)°. These compare to the Sc-O distance, 2.1200(4) Å, observed in the simple borate $ScBO_3$ [21] in which a small trigonal elongation of the octahedron affords the O-Sc-O angle, 92.28(1)°. The Sc atoms are well isolated from one another (number density = 5 X 10^{21} cm^{-3}, cf. $ScBO_3$, number density = 2 X 10^{22} cm^{-3}) with the distance of closest approach at 5.2201(6) Å along the b axis; they do not share any O atoms. Eight of the ten O atoms are coordinated by four cations in approximate tetrahedral coordination. Atom O(3) is bound by atoms B(3), Sc, and Sr(2) in a trigonal manner. Likewise, the bridge atom O(8) in one of the pyroborate groups binds to three atoms B(1), B(2), and Li in a distorted triangular manner. The individual polyhedra condense only by sharing edges and vertices. The polyhedra occupied by the Sr(2) atoms join through edges O(5)···O(5) and O(1)···O(9) to form a one-dimensional string along the direction [101]. The Sr(2)-centered polyhedron also shares edges O(3)···O(9) and O(1)···O(9), and the vertex O(1) with Sc-centered octahedra. The two sevenfold polyhedra of atoms Sr(1) and

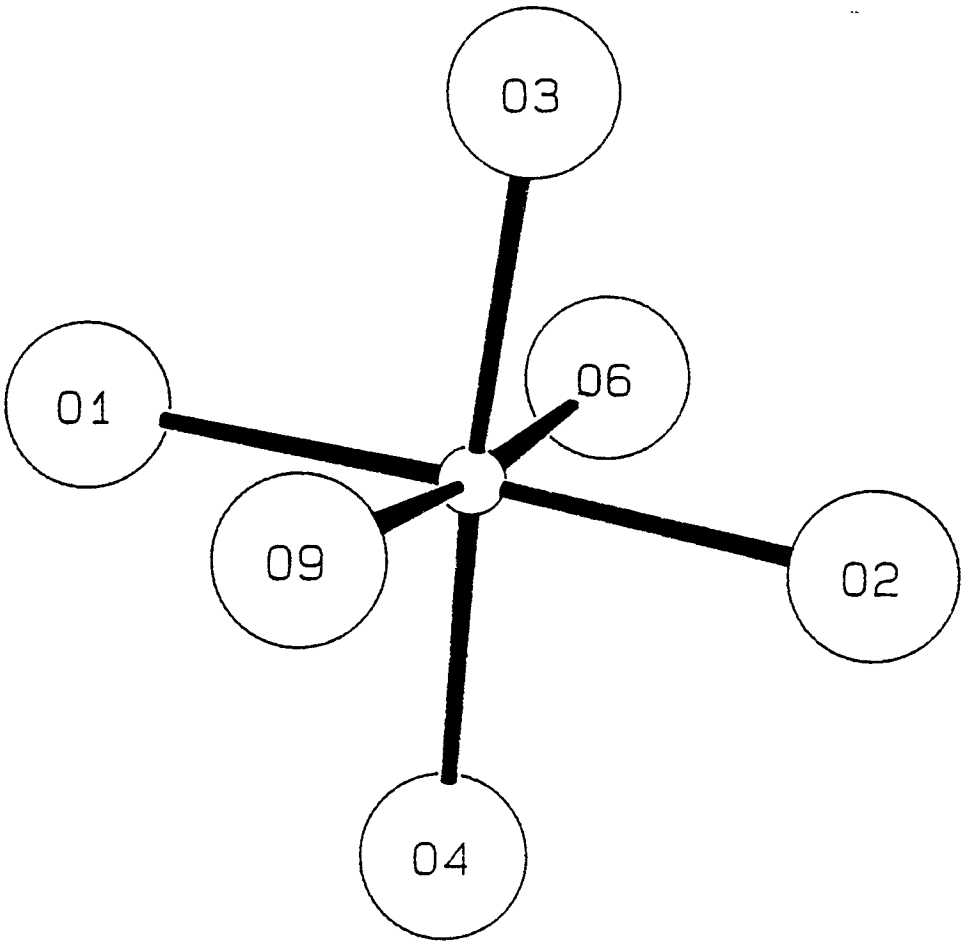

Figure 8.8. Sc in distorted octahedron.

Sr(2) share only one vertex O(5). The Sr(1)-centered polyhedron shares vertices O(2), O(4), and O(6) with Sc atoms. The edges O(4)···O(8) and O(2)···O(10) and the vertex O(6) bridge the Sr(1) and Li atoms. The edge O(2)···O(6) and the vertex O(4) of the Sc octahedron are shared by the neighboring Li atoms.

Attempts to synthesize derivatives with Ga, Cr, or Al atoms substituted for the Sc atoms resulted in the borate SrB_2O_4 as the major product. The ions Ga^{3+} (r = 0.620 Å), Cr^{3+} (r = 0.62 Å), and Al^{3+} (r = 0.530 Å) apparently are not large enough (Sc^{3+}, r = 0.73 Å) to support the octahedral environment in the presence of the Sr^{2+} cation. The ranges of stability for partial substitution of Ca^{2+}, Ba^{2+}, and Al^{3+} ions into this structure as well as the melting characteristics, optical properties of doped samples, and ion exchange reactions involving the replacement of the Li^{+} ion will be discussed in a forthcoming paper.

Acknowledgments

This research was supported by the U.S. Department of Energy and Lawrence Livermore National Laboratory under contract No. 2143103. The X-ray diffractometer was purchased with funds provided by the U.S. National Science Foundation (CHE-8604239) and by the donors of the Foursight! program administered by the OSU Foundation.

References

[1] See for example, T. Harig, B. Struve, and G. Huber, J. Luminescence **24**, 367 (1981).

[2] D. Eimerl, L. Davis, S. Velsko, E.K. Graham, and A. Zalkin, J. Appl. Phys. **62**, 1968 (1987).

[3] C. Chen, B. Wu, G. You, A. Jiang, and Y. Huang, Dig. Tech. Papers, **XIII IQEC**, paper MCC5 (1984).

[4] C. Chen, B. Wu, A. Jiang, and G. You, Sci. Sinica Ser. **B 28**, 235 (1985).

[5] K. Kato, IEEE J. Quant. Electron. **QE-22**, 1013 (1986).

[6] C. Chen, Y.X. Fan, R.C. Eckardt, and R.L. Byer in "SPIE Proceedings, Laser and Nonlinear Optical Materials", ed. L.G. DeShazer, **Vol. 681**, 12 (1986).

[7] S.T. Lai, B.H.T. Chai, M. Long, and R.C. Morris, IEEE J. Quant. Electron. **QE-22**, 1931 (1986).

[8] Molecular Structure Corporation, TEXSAN, Structure Analysis Package. MSC, 3304 Longmire Drive, College Station, TX 77840, USA.

[9] N. Walker and D. Stuart, Acta Cryst. **A 39**, 158 (1983).

[10] Supplementary Material, available from authors.

[11] W.H. Zachariasen, Acta Cryst. **A 24**, 214 (1968).

[12] Y. Takeuchi, Acta Cryst. **5**, 574 (1952).

[13] M.E. Mrose and M. Fleischer, Am. Mineralogist **48**, 915 (1963).

[14] H. Bartl and W. Schuckmann, Neues Jahrb. Mineral. Monatsh. **8**, 253 (1966).

[15] O.V. Yakubovich, N.A. Yamnova, B.M. Shchedrin, M.A. Simonev, and N.V. Belov, Dokl. Akad. Nauk SSSR **228**, 842 (1976).

[16] E.L. Muetterties and C.M. Wright, Quart. Rev. **21**, 1 (1967).

[17] J. Krogh-Moe, Acta Chem. Scand. **18**, 2055 (1964).

[18] H. Sun and D.A. Keszler, results to be submitted.

[19] R.W. Smith and D.A. Keszler, J. Solid State Chem. **81**, 305 (1989).

[20] G. Bayer, Z. Kristallogr. **133**, 85 (1971).

[21] D.A. Keszler and H. Sun, Acta Cryst. **C 44**, 1505 (1987).

BIBLIOGRAPHY

L.J. Andrews and S.M. Hitelman, Ettore Majorana Int. Sci. Ser.: Phys. Sci. **30**, 515 (1987).

H. Bartl and W. Schuckmann, Neues Jahrb. Mineral., **8**, 253 (1966).

P.A. Baucher, M. Gasperin, and B. Cervelle, Acta Crystallogr.**B 32**, 2211 (1976).

G. Bayer, Z. Kristallogr. **133**, 85 (1971).

S. Berger, Acta Chem. Scand., **4**, 1054 (1950).

S. Block, G. Burley, A. Perloff, and R.D. Mason, J. Res. Nat. Bur. Stand. **62**, 95 (1959).

I.D. Brown in "Structure and Bonding in Crystals," **Vol. II**, ed. M. O'Keeffe and A. Navrotsky, Academic Press: New York, p. 1, (1981).

A. Budgor, SPIE **vol 461**, New Lasers for Analytical and Industrial Chemistry, 62 (1984).

J.A. Caird, S.A. Payne, P.R. Staver, A.J. Ramponi, L.L. Chase, and W.F. Krupke, IEEE J. Quantum Electron. **QE-24**, 1077 (1988).

L.L. Chase, and S.A. Payne, IEEE J. Quantum Electron., in press.

C. Chen, Y.X. Fan, R.C. Eckardt, and R.L. Byer in "SPIE Proceedings, Laser and Nonlinear Optical Materials", ed. L.G. DeShazer, **Vol. 681**, 12 (1986).

C. Chen, Y. Wu, A. Jiang, B. We, G. You, R. Li, and S. Lin, J. Opt. Soc. Am. **B 28**, 235 (1985).

C. Chen, B. Wu, A. Jiang, and G. You, Sci. Sinica Ser. **B 28**, 235 (1985).

C. Chen, B. Wu, G. You, A. Jiang, and Y. Huang, Dig. Tech. Papers, **XIII IQEC**, paper MCC5 (1984).

T.M. Dunn and A.H. Francis, Phys. Rev. Lett., **25(11)**, 705 (1970).

D. Eimerl, L. Davis, S. Velsko, E. K. Graham, and A. Zalkin, J. Appl. Phys. **62**, 1968 (1987).

W.H. Fonger and C.W. Struck, Phys. Rev. B **11(9)**, 3251 (1975).

M. Gasperin, Acta Crystallogr. B **30**, 1181 (1974).

D.L. Graf and W.F. Bradley, Acta Cryst. **15**, 238 (1962).

T. Harig, B. Struve, and G. Huber, J. Luminescence **24**, 367 (1981).

H. Y-P. Hong and K. Dwight, Mat. Res. Bull., **9**, 1661 (1974).

J. Huang and D.A. Keszler, to be submitted.

Yu.N. Il'in, V.V. Kravchenko, and K.I. Petrov, Russ. J. Inorg. Chem. **28**, 909 (1983/84).

G.F. Imbusch, W.M. Yen, A.L. Schawlow, D.E. McCumber and M.D. Sturge, Phys. Rev. **133(4A)**, 1029 (1964).

K. Kato, IEEE J. Quant. Electron. **QE-22**, 1013 (1986).

F. Kellendonk, T. van den Belt, and G. Blasse, J. Chem. Phys., **76(3)**, 1194 (1982).

D. A. Keszler and H. Sun, Acta Crystallogr. C **44**, 1505 (1987).

Kirk-Othmer: Encyclopedia of Chemical Technology, John Wiley & Sons, Inc. **14**, 527 (1981).

H. König, R. Hoppe, and M. Jansen, Z. anorg. allg. Chemie, **449**, 91 (1979).

J. Krogh-Moe, Acta Chem. Scand. **18**, 2055 (1964).

W.F. Krupke and L.L. Chase, SPIE Int. Soc. Opt. Eng., **Vol. 1040**, in press.

F. Liebau, Structural Chemistry of Silicates, Springer-Verlag, Berlin, p. 48 (1985).

S.T.Lai, SPIE High Power and Solid State Lasers, **22**, 146 (1986).

S.T. Lai, SPIE **vol 622**, High Power and Solid State Lasers, 146 (1986).

S.T. Lai, B.H.T. Chai, M. Long, and R.C. Morris, IEEE J. Quantum Electron. **QE-22**, 1931 (1986).

S.T. Lai, B.H.T. Chai, M. Long, M.D. Shinn, J.A. Caird, J.E. Marion, and P.R. Staver, In Tunable Solid-State Lasers II; A.B. Budgor, L. Esterowitz, and L.G. DeShazer, eds.; Springer-Verlag, Berlin, p. 145 (1986).

K. Machida, G. Adachi, and J. Shiokawa, Acta Crystallogr. **B 35**, 145 (1979).

T. H. Maiman, Nature **187**, 493 (1960).

G. Mariotto, M. Montagna and F. Rossi, J. de Phys. **46**, C7-343 (1985).

B.W. McClelland, L. Hedberg, K. Hedberg, and K. Hagen, J. Am. Chem. Soc. **105**, 3789 (1983).

D.E. McCumber and M.D. Sturge, J. Appl. Phys. **34(6)**, 1682 (1963).

A. Monteil, C. Garapon and G. Boulon, J. Lumin. **39**, 167 (1987).

G.P. Morgan, T.J. Glynn, G.F. Imbusch and J.P. Remeika, J. Chem. Phys. **69**, 4859 (1978).

M.E. Mrose and M. Fleischer, Am. Mineralogist **48**, 915 (1963).

E.L. Muetterties and C.M. Wright, Quart. Rev. **21**, 109 (1967).

T. Muramoto and T. Hashi, Phys. Lett. **51A(7)**, 423 (1975).

K.P. O'Donnell, A. Marshall, M. Yamaga and B. Henderson, J. Lumin. **42**, 365 (1989).

S. A. Payne, L. L. Chase, L. K. Smith, W. L. Kway, and H. W. Smith, J. Appl. Phys., **66(3)** 1051 (1989).

S.A. Payne, L.L. Chase, and G.D. Wilke, Phys. Rev. B **37**, 998 (1988).

T.A. Reynolds, private communication.

U.L. Schäfer, Neues Jahrb. Min. Monatsh. 75 (1980).

K.I. Schaffers, T. Alekel III, P.D. Thompson, J.R. Cox, and D.A. Keszler, J. Am. Chem. Soc. **112**, 7068 (1990).

K.I. Schaffers, P.D. Thompson, T. Alekel III, J.R. Cox, and D.A. Keszler, to be submitted.

M.L. Shand and S.T. Lai, IEEE J. Quantum Electron. **QE-20**, 105 (1984).

M.L. Shand and J.C. Walling, IEEE J. Quant. Elec. **QE-18**, No. 7, 1152 (1982).

R.D. Shannon, Acta Crystallogr. A **32**, 751 (1976).

R.W. Smith and D.A. Keszler, J. Solid State Chem. **81**, 305 (1989).

W.C. Steele and J.C. Decius, J. Chem. Phys. **25**, 1184 (1956).

B. Struve and G. Huber, Appl. Phys. B, **36**, 195 (1985).

D. Stuart and N. Walker, Acta Crystallogr. **B 39**, 158 (1983).

S. Sugano and Y. Tanabe, J. Phys. Soc. Jpn. **13(8)**, 880 (1958).

Y. Takéuchi, Acta Crystallogr. **5**, 574 (1952).

Y. Tanabe and S. Sugano, J. Phys. Soc. Jpn. **9**, 766 (1954).

TEXSAN: Single Crystal Structure Analysis Software, Version 5.0, (1989). Molecular Structure Corporation, The Woodlands, TX 77381.

P.D. Thompson, J. Huang, R.W. Smith, and D.A. Keszler, J. Solid State Chem., submitted.

P.D. Thompson and D.A. Keszler, Chem. Mater. **1**, 292 (1989).

P.D. Thompson and D.A. Keszler, Solid State Ionics **32/33**, 521 (1989).

P.D. Thompson and D.A. Keszler, to be submitted.

D. Vivien, B. Viana, A. Revcolevschi, J.D. Barrie, B. Dunn, P. Nelson and O.M. Stafsudd, J. Lumin. **39**, 29 (1987).

N. Walker and D. Stuart, Acta Cryst. **A 39**, 158 (1983).

J.C. Walling, In Topics in Laser Physics, Tunable Lasers, Eds.: L.F. Mollenauer and J.C. White, Springer-Verlag, Berlin, **59**, p. 331 (1987).

M.J. Weber, J. Appl. Phys. **44(9)**, 4058 (1973).

R.W.G. Wyckoff, Crystal Structures, 2nd ed., Interscience Publishers, **2**, p. 6 and 13 (1964).

O.V. Yakubovich, M.A. Simonov, E.L. Belokoneva, Yu.K. Egorov-Tismenko, and N.V. Belov, Dokl. Akad. Nauk SSSR **230**, 837 (1976).

O.V. Yakubovich, M.A. Simonov, and N.V. Belov, Dokl. Akad. Nauk SSSR **238**, 98 (1978).

O.V. Yakubovich, N.A. Yamnova, B.M. Shchedrin, M.A. Simonov, and N.V. Belov, Dokl. Akad. Nauk SSSR **228**, 842 (1976).

K. Yvon, W. Jeitschko, and E. Parthe, J. Appl. Cryst. **10**, 73 (1977).

W.H. Zachariasen, Acta Cryst. **A 24**, 214 (1968).

APPENDICES

APPENDIX 1

THE NEW RHOMBOHEDRAL BORATE $Sr_3Sc_2(BO_3)_4$

The title compound exists at the midpoint of the $Sr_3B_2O_6$-$2ScBO_3$ phase line in the triangle shown in Figure 1.7. I present the best experimental powder X-ray pattern obtained to date in Figure A1.1. Initial attempts to solve the crystal structure were performed in a monoclinic subcell (space group $P2_1/c$, V = 1032 $Å^3$). I achieved a minimum residual of 9 % by using atomic positions obtained from a SHELXS direct methods solution. The structure contains three crystallographically distinct Sr atoms. One is eight coordinate and the other two are nine coordinate. The two Sc atoms occupy octahedral sites.

Although the structure solution resulted in reasonable distances and angles for the SrO_8, SrO_9, and ScO_6 polyhedra, reasonable B-O distances and angles could not be obtained. The B-O distances ranged from 1.17 Å to 1.63 Å, and O-B-O angles ranged from 109° to 131°. Neither range is consistent with the metrical results of other borate structures. After it became evident that no amount of moving the B atoms around in the monoclinic subcell would give a reasonable structure solution, I abandoned the proposed model and mounted and examined additional single crystals on the diffractometer.

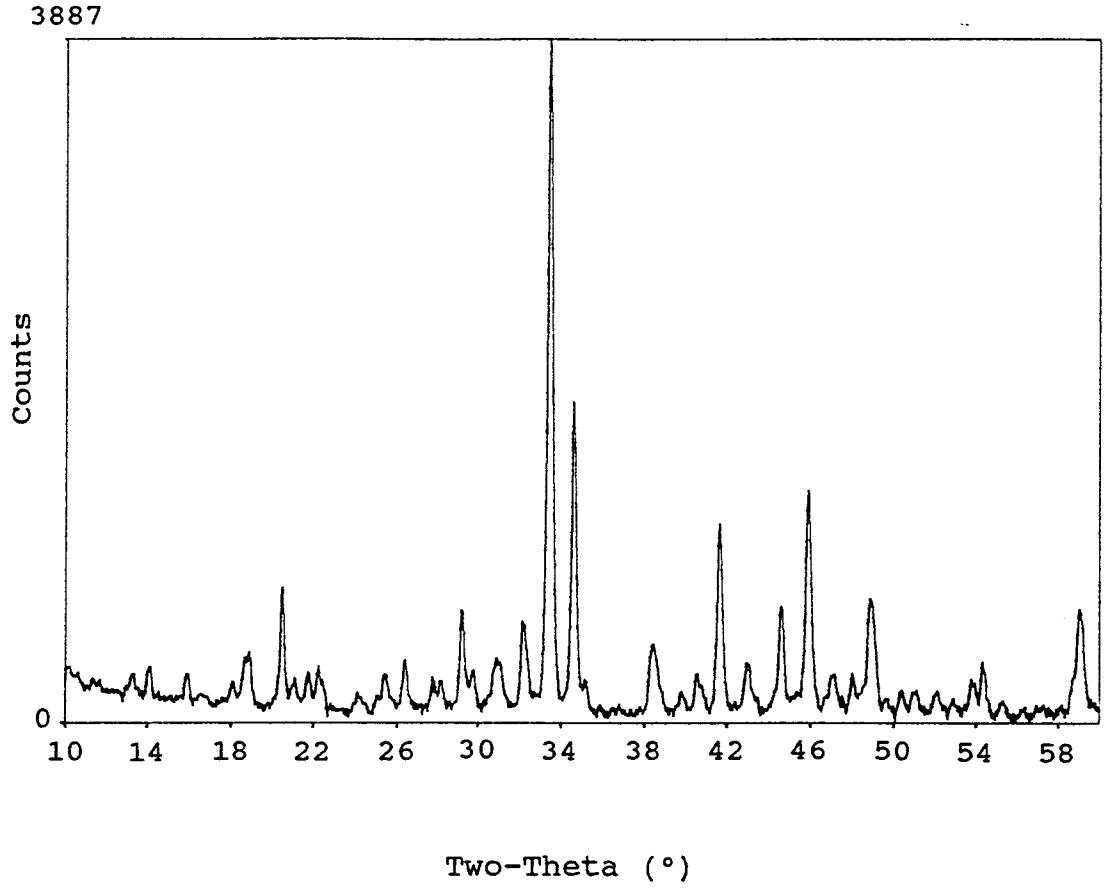

Figure A1.1. Experimental powder diffraction pattern exhibited by the new material $Sr_3Sc_2(BO_3)_4$.

From several different single crystals, I identified a large rhombohedral unit cell with a volume that is 12 times larger than the monoclinic subcell. The rhombohedral cell was verified from analysis of the Laue symmetry. Metrical parameters for this large unit cell that will be used as the basis for a new data collection are listed in Table A1.1. I verified that this large rhombohedral cell is representative of the powder by using a calculated powder pattern to index twenty peaks in the experimental pattern given in Figure A1.1. Least-squares refinement of peak positions obtained from the experimental pattern afforded unit cell parameters in agreement with those obtained from single crystals.

I expect that a final structure solution on the basis of the rhombohedral unit cell will reveal the correct B atomic positions. The smaller monoclinic subcell is repeated 12 times in the larger cell because of symmetry constraints and the ordering of the B atoms. A preliminary drawing of the monoclinic subcell reveals that the BO_3 groups likely adopt a unique planar arrangement in which they "stand up" within a layer and link interleaved Sr- and Sc-centered polyhedra.

Table A1.1. Structural parameters of the new orthoborate $Sr_3Sc_2(BO_3)_4$.

Crystal system	rhombohedral
a = b (Å)	20.713(1)
c (Å)	33.324(1)
V ($Å^3$)	12381.9(6)
z	48 (21.5 $Å^3$/O atom)
Space group	$R\bar{3}c$ or R3c

APPENDIX 2

THE UNIQUE TRIGONAL BORATE $LiSrM_2(BO_3)_3$ (M = Y,Er)

The title compound is a new material that I discovered in an attempt to grow crystals of $Sr_3Y(BO_3)_3$ from an $LiBO_2$ flux. Unit cell parameters for the material containing M = Y are listed in Table A2.1. Structure solution resulted in an unsatisfactorily high residual probably because of disorder between the Sr and Y sites. A calculated powder pattern from this partial solution is given in Figure A2.1.

Another batch of crystals display the powder pattern of the analogue $LiSrEr_2(BO_3)_3$. Because I grew this material in an excess of SrO, B_2O_3, and $LiBO_2$, the experimental pattern presented in Figure A2.2 reveals the presence of minor amounts of $Sr_3B_2O_6$ and SrB_2O_4. The sample includes pink Er-containing crystals and colorless crystals. I expect that this material may display less disorder of Sr^{2+} and M^{3+} than in the M = Y material because the Er^{3+} is slightly smaller than Y^{3+}. Data collection and structure solution from this batch of crystals should lead to a more accurate refinement of the structure.

Table A2.1. Structural parameters of the new material $LiSrY_2(BO_3)_3$.

Crystal system	rhombohedral
a = b (Å)	10.312
c (Å)	6.419
V ($Å^3$)	591.14
z	3 (21.9 $Å^3$/O atom)
Space group	$P\bar{3}m1$ (#164)

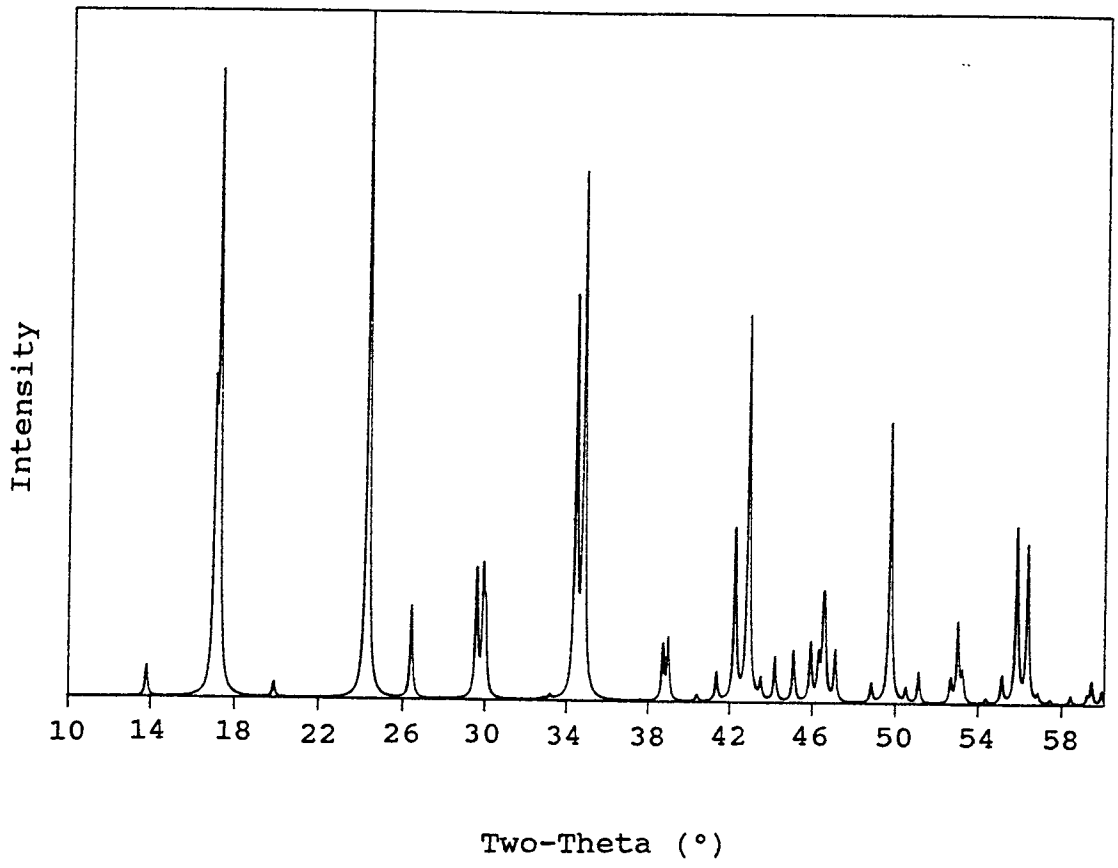

Figure A2.1. Calculated powder diffraction pattern for the new material $LiSrY_2(BO_3)_3$.

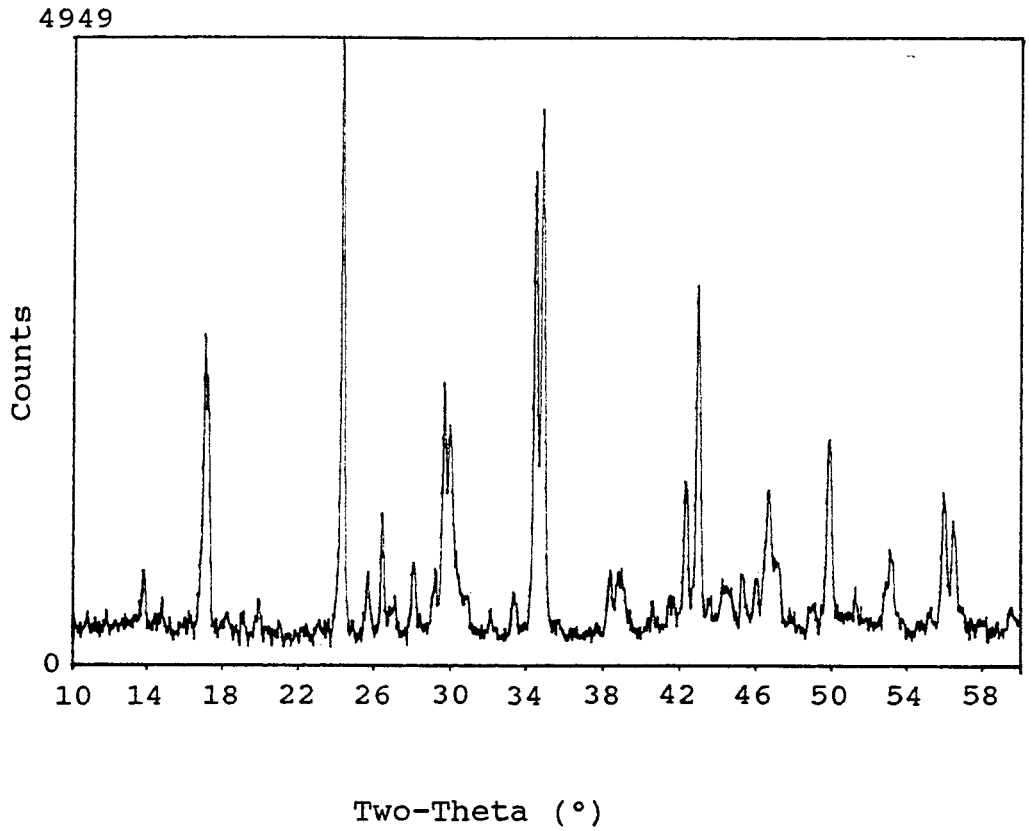

Figure A2.2. Experimental powder diffraction pattern of the new material $LiSrEr_2(BO_3)_3$.